Dissertation

submitted to the

Combined Faculty of Mathematics, Engineering, and Natural Sciences

of Heidelberg University, Germany

for the degree of

Doctor of Natural Sciences

Put forward by

Lillian de Bruin

Born in: New York, United States

Oral Examination: 29.11.2023

Real-time infrared processes in high-temperature QCD plasmas

Referees:	Jan M. Pawlowski Bjoern Malte-Schaefer

Abstract

Quantum Chromodynamics (QCD) is a rich non-Abelian gauge theory that describes the strong nuclear force. Heavy ion collisions create a QCD plasma, in which the weakly coupled high-temperature regime of the theory can be studied. At low momenta in QCD plasmas, several features emerge that affect transport phenomena during the thermalization of the plasma. In this thesis we will investigate two such features and explore their manifestations in heavy ion collisions and their significance.

The first half of this thesis investigates the dissipative effects of sphaleron transitions in the quark-gluon plasma. We modify the anomalous hydrodynamic equations of motion to account for dissipative effects due to QCD sphaleron transitions. By investigating the linearized hydrodynamic equations, we show that sphaleron transitions lead to non-trivial effects on vector and axial charge transport phenomena in the presence of a magnetic field. Due to the dissipative effects of sphaleron transitions, a wavenumber threshold k_{CMW} emerges characterizing the onset of chiral magnetic waves. Sphaleron damping also significantly impacts the time evolution of both axial and vector charge perturbations in a QCD plasma in the presence of a magnetic field. Based this, we also investigate the dependence of the vector charge separation on the sphaleron transition rate, which may have implications for the experimental search for the Chiral Magnetic Effect in Heavy Ion Collisions.

The second half of this thesis explores the formation of a condensate in the moments after a heavy ion collision. We show gauge condensation, which occurs as a consequence of the large density of gluons. To identify this condensation phenomenon, we construct two local gauge-invariant observables that carry the macroscopic zero mode of the gauge condensate. The first order parameter investigated here is the correlator of the spatial Polyakov loop. We also consider, for the first time, the correlator of the gauge invariant scalar field, associated to the exponent of the Polyakov loop. Using real-time lattice simulations of classical-statistical $SU(2)$ gauge theory, we find gauge condensation on a system-size dependent time scale $t_{\mathrm{cond}} \sim L^{1/\zeta}$ with a universal scaling exponent ζ. Furthermore, we suggest an effective theory formulation describing the dynamics using one of the order parameters identified. The formation of a condensate at early times may have intriguing implications for the early stages in heavy ion collisions.

Contents

Abstract

List of Figures

List of Tables

1 Introduction **1**
Outline of this thesis 4

2 Theoretical background **6**
2.1 Quantum chromodynamics 6
2.2 The chiral anomaly and the vacuum of gauge theories 10
2.2.1 The Atiyah-Singer index theorem 11
2.2.2 Vacua in non-Abelian gauge theories 12
2.3 Sphaleron transitions 15
2.3.1 Chiral Phenomena 16
2.3.2 Chirality transfer in non-Abelian gauge theories 17
2.3.3 Experimental search for chiral phenomena 18
2.4 Initial stages far from equilibrium 20
2.4.1 Classical-statistical simulations 20
2.4.2 Hierarchy of scales far from equilibrium 21
2.4.3 Wilson loops 23
Area law behavior out of equilibrium 24
2.4.4 Non-thermal fixed points and universality 25

3 Sphaleron damping and charge transport in QCD plasmas **27**
3.1 Chirality charge dynamics in high-temperature QCD plasmas 29
3.2 Hydrodynamic description of anomalous transport in QCD-like theories . 31
3.3 Hydrodynamic excitations in charge-neutral plasma 36
3.3.1 Single flavor dynamics 37
3.3.2 Multi flavor dynamics 43
3.4 Effects of sphaleron damping on vector and axial charge dynamics 46
3.4.1 Vector charge perturbations 46
3.4.2 Axial charge perturbations 47
3.4.3 Sensitivity of charge separation to the sphaleron rate 48
3.5 Conclusions & Outlook 52

4 Gauge-invariant condensation 54
4.1 Early-time infrared dynamics far from equilibrium 56
4.1.1 The infrared scale far from equilibrium 57
4.1.2 Local order parameters 58
4.2 Gauge-invariant condensation 62
4.2.1 Classical-statistical lattice simulations 62
4.2.2 Evolution of one-point functions 63
4.2.3 Condensate fractions 65
4.3 Conclusion 70

5 Conclusion 71

Acknowledgements 73

A Divergence identities derivation 74
A.1 Divergence of the entropy current 74
A.2 Divergence of vorticity and magnetic field 75

B Linearized hydrodynamic equations 77
B.1 Linearizing energy-momentum transport equations 77
B.2 Linearizing charge transport equations 79

C Multiflavor degenerate perturbation theory calculations 81

D Mean and error estimates for scaling exponents 85

Bibliography 87

List of Figures

1.1 Illustration of the spacetime evolution of a relativistic heavy ion collision. The far-from-equilibrium matter produced in a collision thermalizes after ~ 1 fm/c, resulting in the quark-gluon plasma. The quark-gluon plasma, which is described by viscous hydrodynamics, expands and cools until the system reaches the confining "freeze-out" temperature at which hadrons form. The resulting gas is composed of dilute free-streaming hadrons, which are observed in the various detectors at heavy ion collision experiments. Figure from Ref.[1] 2

2.1 Visualization of the sphaleron transition in the periodic QCD vacuum. Transitions between topologically inequivalent vacua (labeled by N_{CS}) can occur through quantum tunneling, or in a system with high temperatures like a QGP, can be thermally activated by a sphaleron transitions. 15
2.2 Time evolution of the hard scale (λ^2), the electric screening/Debye scale (m_D^2), and the spatial string tension/magnetic scale (σ) far from equilibrium. A dynamical separation of scales is clearly visible. Figure from [2] 22

3.1 Single-flavor dispersion relations (3.38) for charge modes without dissipation from sphaleron transitions. The diffusion constant is fixed, so the behavior of the excitations depends on the wavenumber **k** and the magnetic field strength. 38
3.2 Single-flavor dispersion relations ω_A (3.43) and ω_V (3.44) for different values of Γ_{sph} plotted for $eB/T^2 = 0.05, 0.15, 0.45$ (top to bottom) respectively. Vertical dotted line represents k_{CMW} for each case. 39
3.3 Mixing angle $\cos\Omega^2_{A/V}$ for the single-flavor case plotted for $eB/T^2 = 0.45$, $\Gamma_{\text{sph}}/T^4 = 0.001$. Vertical dotted line represents k_{CMW}. 40
3.4 Phases for the single-flavor case plotted for $eB/T^2 = 0.45$, $\Gamma_{\text{sph}}/T^4 = 0.001$. Vertical dotted line represents k_{CMW}. 40
3.5 Dispersion relations in the multiflavor case for different values of Γ_{sph} plotted for $eB/T^2 = 0.05, 0.15, 0.45$ (top to bottom), respectively. Black solid lines indicate the asymptotic limits of small or large wavenumber k. 42
3.6 Mixing angles for two-flavor system, $eB/T^2 = 0.45$. 43
3.7 Phases for two-flavor system, $eB/T^2 = 0.45$. 44
3.8 Spatial profiles of axial (n_A) and vector (n_V) charge distributions for *initial vector charge perturbation* after an evolution for $t = 10$ fm/c. Different curves in each panel correspond to four different values of the sphaleron transition rate Γ_{sph}. Different columns show the the results for different magnetic field strength $eB/T^2 = 1/16$ in the left column and $eB/T^2 = 1$ in the right column. 47

3.9 Spatial profiles of axial (n_A) and vector (n_V) charge distributions for *initial axial charge perturbation* after an evolution for $t = 10$ fm/c. Different curves in each panel correspond to four different values of the sphaleron transition rate Γ_{sph}. Different columns show the the results for different magnetic field strength $eB/T^2 = 1/16$ in the left column and $eB/T^2 = 1$ in the right column. 48

3.10 Electric charge separation, quantified by the electric dipole moment D for an initial axial charge distribution as a function of Γ_{sph} for single- and two-flavor configurations of various initial charge ratios at $t = 10$ fm/c. . 49

4.1 Visualization of the spatial correlation between the Polyakov loop correlator $\langle PP^\dagger\rangle(t, \Delta x, L)$ in a) and the rectangular spatial Wilson loop $W[t, \Delta x, L]$ in c). The spatial periodicity of the system results in the identification of coordinates $x_2' \equiv x_2 \bmod L$ on the lattice, causing the Wilson loop to exhibit a wrapping effect in the x_2 direction, as depicted in b). The distinguishing feature between the Polyakov loop correlator and the Wilson loop is the presence of connecting Wilson lines (blue) in the latter, which shows the connection between the two quantities. . . . 57

4.2 Comparison of the Wilson loop expectation value $\langle W\rangle$ and the Polyakov loop correlator $\langle PP^\dagger\rangle$ on a lattice with size $N_s = 96$ at time $Qt = 1000$. The Polyakov loop correlator $\langle PP^\dagger\rangle$ exhibits consistent dynamics with the Wilson loop at larger spatial separations, indicating a strong correlation between the two quantities. 58

4.3 Comparison of the expectation value of the Polyakov loop to the Polyakov loop re-expressed in terms of the algebra-valued holonomous eigenvalue field for $N_s = 96$ lattice, $Q_s t = 1000$. This shows the approximate agreement of the one-point functions $\langle P\rangle \equiv \langle\cos(\varphi)\rangle \approx \cos(\langle\varphi\rangle)$. 62

4.4 Expectation values of the spatial Polyakov loop and the scalar algebra field as functions of rescaled time for different volumes. The Polyakov loop is rescaled with $\zeta = 0.24$ and the algebra field is rescaled with $\zeta = 0.25$, both exhibiting scaling behavior in time. We also observe that $\langle\phi\rangle$ starts from $\approx \pi/2$ and decreases with time, which is in line with Figure 4.3. In the context of condensation, the connected correlator becomes increasingly independent of $\langle\phi\rangle$, indicating Bose-Einstein condensation behavior. . . . 64

4.5 Condensate fractions (4.21) of the connected correlators $\langle PP^\dagger\rangle_c$ and $\langle\varphi\varphi^\dagger\rangle_c$ as functions of rescaled time for different lattice volumes. All curves fall on top of each other and therefore show the emergence of a volume-independent condensate fraction. The rescaled quantities have scaling exponents $\zeta = 0.31$ and $\zeta = 0.34$, respectively, using the procedure in Appendix D (cf., Table 4.1). (*Insets:*) Condensate fraction as a function of time, not rescaled, for the respective correlators. 65

4.6 Condensate fraction (Eq. (4.23)) of the full Polyakov loop correlator (left) and the full algebra field correlator (right) as a function of finite-size rescaled time for different volumes. All curves fall on top of each other and therefore show the emergence of a volume-independent condensate fraction. The scaling exponents ζ are identical to those in Figure 4.5. Insets: Condensate fraction as a function of time, not rescaled, for the respective correlators. 65

4.7 Rescaled connected correlators $\langle PP^\dagger\rangle_c$ and $\langle\varphi\varphi^\dagger\rangle_c$ normalized by their values at $\Delta x = 0$ for fixed $Q\Delta x = 5$, with a reduced time extent ($Qt \leq 15000$). The scaling exponents ζ are identical to those in Figure 4.5. . . 66
4.8 Time evolution of the normalized connected Polyakov loop correlator $\langle PP^\dagger\rangle_c(\Delta x)/\langle PP^\dagger\rangle_c(\Delta x{=}0)$ (left) and normalized connected algebra field correlator $\langle\varphi\varphi^\dagger\rangle_c(\Delta x)/\langle\varphi\varphi^\dagger\rangle_c(\Delta x{=}0)$ (right) shown for six times $Qt = 100, 300, 1000, 2000, 4000, 8000$ on a $N_s = 96$ lattice. Clear growth of condensate is demonstrated for both order parameters. 67
4.9 Comparative analysis of the normalized connected Polyakov loop correlator $\langle PP^\dagger\rangle(\Delta x)/\langle PP^\dagger\rangle(\Delta x{=}0)$ and the normalized connected algebra field correlator $\langle\varphi\varphi^\dagger\rangle(\Delta x)/\langle\varphi\varphi^\dagger\rangle(\Delta x{=}0)$ on a lattice with size $N_s = 96$ at time $Qt = 1000$, as in Figure 4.2 and Figure 4.8. 68

List of Tables

4.1 Summary of scaling exponents for different condensate observables. These values and their uncertainties have been estimated using a similar χ^2-procedure as in [3–5], which we outline in Appendix D. The scaling exponent ζ is compared for the two sufficiently local observables studied in this work, the connected Polyakov loop correlator and the algebra field, to the Polyakov loop correlator in (4.23), and to the Wilson loop expectation value studied in [5]. 66

For Phyllis Dircks and Claire de Bruin xx

Chapter 1

Introduction

Quantum Chromodynamics (QCD) is a non-Abelian gauge theory that describes the strong nuclear force, one of the four fundamental forces of the standard model of particle physics. The theory describes interactions between fermionic matter fields called quarks, mediated by the gauge boson known as the gluon.

Studying QCD is not only interesting but also practical. For example, QCD interactions can lead to mass generation [6–8], QCD degrees of freedom are an essential ingredient to understanding early universe cosmology (~ 1 microsecond post-Big Bang) [1, 9] and neutron stars and mergers [10], and matter produced in heavy ion collisions [11].

Ultrarelativistic heavy ion collisions in particular probe QCD in extreme conditions, such as high temperatures, large baryon densities, and strong magnetic fields. Currently, the facilities performing such experiments are the Relativistic Heavy Ion Collider (RHIC) at Brookhaven National Laboratory in the US and the Large Hadron Collider (LHC) at CERN in Europe. Over the last decades, experiments at RHIC and LHC have collided a plethora of nuclei over a wide range of energies to better understand the quark-gluon plasma (QGP), a state of deconfined quarks and gluons that was also present in the early universe in the first microseconds after the Big Bang.

In heavy ion collisions, far-from-equilibrium matter is produced and thermalizes on a time scale ~ 1 fm/c, resulting in the QGP. The quark-gluon plasma expands and cools until the system reaches the confining “freeze-out” temperature at which hadrons form. The QGP, which has been discovered to be a nearly perfect fluid [12, 13] is described by viscous hydrodynamics. During the hadronic freezeout period, a gas composed of dilute free-streaming hadrons is produced. The hadrons are observed in the various detectors at heavy ion collision experiments. This is illustrated in Figure 1.1[1].

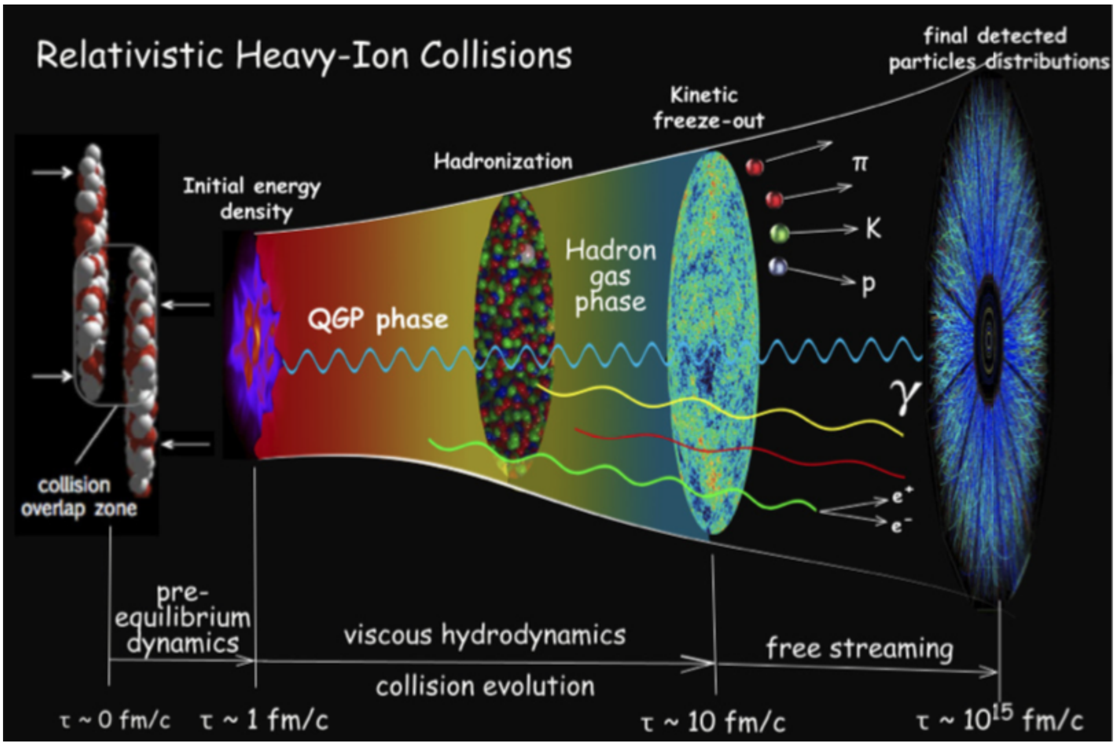

FIGURE 1.1: Illustration of the spacetime evolution of a relativistic heavy ion collision. The far-from-equilibrium matter produced in a collision thermalizes after ~ 1 fm/c, resulting in the quark-gluon plasma. The quark-gluon plasma, which is described by viscous hydrodynamics, expands and cools until the system reaches the confining "freeze-out" temperature at which hadrons form. The resulting gas is composed of dilute free-streaming hadrons, which are observed in the various detectors at heavy ion collision experiments. Figure from Ref.[1]

The heavy ion collision experiments have been wildly successful in characterizing the QGP. Some of the important characteristics discovered include the aforementioned "perfect fluid" behavior, the energy loss of jets in the medium (jet quenching), and the regeneration and suppression of quarkonia [12, 13]. However, despite this success, we still lack a comprehensive knowledge of the emergence of these features. Additionally, significant theoretical progress has been achieved in the past decades regarding features that have emerged and could modify our current understanding of the spacetime evolution of the QGP. In this thesis, we will discuss two such features: sphaleron transitions that persist throughout the thermalization of the QGP and condensation that emerges in the initial stages.

QCD has a non-trivial vacuum structure that includes an infinite number of energy-degenerate but topologically inequivalent vacuum configurations [14, 15]. At finite temperature, transitions between vacua are thermally activated by finite-energy configurations called sphalerons. Sphaleron transitions in the QGP lead to the generation of significant fluctuations of axial charge density [2, 15–17], and hence an imbalance in the number of right- and left-handed chiral quarks. Due to the Adler-Bell-Jackiw ("chiral") anomaly [18, 19] and the Atiyah-Singer index theorem [20], the imbalance of chirality sourced by sphaleron transitions has important physical consequences. Perhaps the best-known physical consequence is the separation of electric charge along an applied external magnetic field in a system with a chirality imbalance–this is the Chiral Magnetic Effect [21]. The CME and other anomalous chiral phenomena [22–26] have been found to emerge naturally within the context of relativistic hydrodynamics and significantly modify the hydrodynamic equations [22, 27]. Such systems are also ubiquitous in nature and manifestations of these phenomena occur across a diverse range of energy scales. In particular, these include of baryo- and magnetogenesis in the early universe [28], the QGP in heavy ion collisions [29], and Dirac and Weyl semimetals in condensed matter systems [30].

Although frequent and sizeable in the QGP, the effects of axial charge-changing processes in describing anomalous transport phenomena in heavy-ion collisions are frequently neglected in phenomenological studies [31] and have only been explored to a limited extent in [32, 33]. Therefore, we seek to clarify the conditions under which anomalous charge transport in high-temperature QCD plasmas such as the QGP can be described macroscopically by anomalous relativistic hydrodynamics. We then seek to explore the extent to which the non-conservation of axial charge due to QCD sphaleron transitions affects transport processes in a QCD plasma.

On the other hand, the matter formed moments after a heavy ion collision is far from equilibrium and is characterized by a large initial density of gluons, which could facilitate the formation of a condensate [34]. The identification of such a condensate requires the construction of a gauge-invariant operator that measures the macroscopic zero mode that signals gauge condensation. These types of operators for nonequilibrium condensation have been studied previously in the context of the Abelian Higgs model and its relation to non-Abelian theories [35–37].

Condensation in non-Abelian gauge theories was recently demonstrated in [5]. It is indicated by the formation of a macroscopic zero-mode expectation value that scales proportionally with $(2\pi)^d\delta^{(d)}(0) \to L^d$ for a $d-$dimensional finite volume with the length scale L [38]. Specifically, the study investigated the expectation value of the spatial Wilson loop, which computes the infrared excitations of non-Abelian gauge theories[2, 39–41]. However, the Wilson loop is a non-local object. Therefore it cannot be used to formulate a low energy effective theory with which we can further elucidate the dynamics of the infrared condensate. Therefore, we must devise a local order parameter that is sensitive to gauge condensation.

It is also interesting to note that the non-equilibrium matter formed in the initial stages also exhibits features that are found in other strongly correlated systems across a variety of energy scales, ranging from inflation in the early universe and ultracold atoms. These systems have universal features, and it is interesting to further investigate the presence of such features in non-Abelian gauge theories.

Outline of this thesis In Chapter 2, we present the theoretical concepts relevant to the work done in this thesis. We first introduce the basic features of QCD and matterless Yang-Mills theories, the latter of which will be utilized in Chapter 4. We then spend time discussing the vacuum of gauge theories, both Abelian and non-Abelian, and its relation to the so-called chiral anomaly. We then define sphaleron transitions and emergent chiral phenomena, including the experimental search in both heavy ion collisions and in condensed matter systems. Following this discussion, we then describe the initial stages of heavy ion collisions and the far-from-equilibrium matter created there. We discuss the heirarchy of scales that emerges and focus on the deep infrared scale and Wilson loops. We conclude the chapter with a discussion on non-thermal fixed points and universal features of the non-equilibrium plasma.

The body of this thesis consists of two main parts.

In the first part, Chapter 3, we discuss sphaleron transitions and the role of topological transitions in the equilibration of a QCD plasma. We begin by first discussing axial charge dynamics in high-temperature QCD plasmas. We establish the conditions under which a macroscopic description of sphaleron transitions is justified and discuss how to incorporate them in an anomalous hydrodynamic framework. Then, by examining the dispersion relations, we demonstrate that sphaleron transitions have a non-trivial effect on both anomalous and ordinary vector charge transport in the presence of an external magnetic field. We also observe that the dissipatice effects sourced by sphaleron transitions induce a nontrivial coupling between different species of chiral fermions. We subsequently investigate the sensitivity of charge transport in the presence of an external magnetic field to the sphaleron transition rate via numerical simulations. Additionally, we devise an analytic expression for vector charge separation in a spacetime homogeneous plasma that depends explicitly on the sphaleron transition rate.

In the second part, Chapter 4, we discuss gauge condensation in highly-occupied QCD plasmas and its role in early time dynamics. First, we discuss early time dynamics in the far-from-equilibrium plasma. We then introduce two local order parameters that are related to the Wilson loop, which are used to identify condensation. We finally employ classical-statistical lattice simulations and demonstrate the build up of a macroscopic zero mode that is consistent with condensation.

Parts of this thesis are available as preprints:

[1] L. de Bruin and S. Schlichting. *Sphaleron damping and effects on vector and axial charge transport in high-temperature QCD plasmas.* arXiv:2309.01726

[2] J. Berges, K. Boguslavski, L. de Bruin, T. Butler, and J. M. Pawlowski. *Order parameters for gauge invariant condensation far from equilibrium.* arXiv:12307.13669

Chapter 2

Theoretical background

In this chapter we present the basic theoretical background for the different parts of this thesis. We first in Section 2.1 describe the basics of QCD and relevant aspects of the theory for our studies in Chapter 3 and Chapter 4. Then, in Section 2.2, we discuss the structure of the QCD vacuum and the manifestation of the chiral anomaly in non-Abelian gauge theories. The physical consequences of the vacuum and the chiral anomaly is discussed in Section 2.3, introducing sphaleron transitions and emergent phenomena. Finally, in Section 2.4 we discuss the far-from-equilibrium initial stages of a heavy ion collision. Here, we explain the relevant scales and infrared phenomena and the utility of classical fields and the Wilson loop. We comment on universality and how similar conditions in relativistic and non-relativistic field theories result in Bose-Einstein condensation.

2.1 Quantum chromodynamics

Quantum Chromodynamics (QCD) is a non-Abelian gauge theory coupled to fermions that describes strong nuclear interactions. The Lagrangian of QCD is

$$\mathcal{L}_{\text{QCD}} = -\frac{1}{4} G^a_{\mu\nu} G^{\mu\nu}_a + \sum_f \bar{\Psi}^f_i (i\gamma^\mu D_{\mu,ij} - m_f \delta_{ij}) \Psi^f_j , \tag{2.1}$$

where we dropped the dependence on spacetime x to simplify the presentation. The non-Abelian gauge fields $\mathcal{A}^a_\mu$ describe gluons and belong to the color group $SU(N_c = 3)$ in the adjoint representation with the coupling constant g. These bosonic fields enter the Lagrangian via the non-Abelian tensor $G^a_{\mu\nu}$:

$$G^a_{\mu\nu} = \partial_\mu A^a_\nu(x) - \partial_\nu A^a_\mu + g f^{abc} A^b_\mu A^c_\nu , \tag{2.2}$$

and transform under a local gauge transformation $\Omega(x)$ in the adjoint representation of $SU(3)$ according to

$$A_\mu(x) \rightarrow \Omega(x) A_\mu \Omega^\dagger(x) - \frac{1}{g}(\partial_\mu \Omega(x))\Omega^\dagger(x). \tag{2.3}$$

The gauge fields lie in the basis of the Lie algebra $su(N_c)$ and therefore can be expressed as

$$A_\mu = A_\mu^a t^a, \tag{2.4}$$

where t^a are the generators in the fundamental representation. The generators obey the Lie bracket and normalization condition,

$$[t^a, t^b] = i f^{abc} t^c, \qquad \mathrm{tr}(t^a t^b) = \frac{1}{2}\delta^{ab}. \tag{2.5}$$

The structure constants f^{abc} are real and totally anti-symmetric color tensors. For $SU(3)$, the generators are usually taken to be $t^a = \lambda^a/2$, where λ^a are the Gell-Mann matrices. For $SU(2)$, which will become relevant in Chapter 4, the generators are usually taken to be $t^a = \sigma^2/2$, where σ^a are the Pauli matrices, and the structure constants are given by the Levi-Civita symbol $f^{abc} = \epsilon^{abc}$.[1]

The fermion sector, in the fundamental representation, describes the quark fields Ψ, labelled by color index $i = 1, 2, 3$ and flavor index f that corresponds to quark flavors with masses m_f. The fermionic quark fields transform under a local gauge transformation $\Omega(x)$ in the fundamental representation of the gauge group according to

$$\Psi(x) \rightarrow \Omega(x)\Psi(x), \qquad \bar{\Psi}(x) \rightarrow \bar{\Psi}\Omega^\dagger(x). \tag{2.6}$$

This notation suppresses the quark spin, which can be given by the right-handed component $\Psi_R = \frac{1}{2}(1+\gamma_5)\Psi$ and the left-handed component $\Psi_L = \frac{1}{2}(1-\gamma_5)\Psi$. In the massless limit, these fermions are *chiral*.

Additionally, the covariant derivative $D_{\mu,ij}$ in Eq. (2.1) is defined as

$$D_{\mu,ij} = \partial_\mu \delta_{ij} + i g t_{ij}^a A_\mu^a, \tag{2.7}$$

where t_{ij}^a are the $SU(N_c)$ generators in the fundamental representation.

An additional term can be added to the action, the so-called θ term,

$$\frac{\theta g^2}{32\pi^2} G(x)_{\mu\nu}^a \tilde{G}_a^{\mu\nu}(x), \tag{2.8}$$

---

[1] The Levi-Civita symbols follow the convention $\epsilon^{123} = 1$.

which is an overall topological term. As such, while it has no effect on the local physics of the field, it does play a role in classifying the global topological class of the field configurations. Relevant for us, it classifies the allowed vacua of the theory, and by extension the towers of excited states above them.

It is worth noting that, unless θ is zero, $\mathcal{P}$ and $\mathcal{CP}$ invariances of QCD are lost. Parity violation in strong interactions has never been observed. Additionally, from experiments on the electric dipole moment of the neutron, strict limits on the $\mathcal{CP}$ violaing phase have been placed. However, this does not discount the importance of the θ term in QCD, as the vacuum can fave fluctuations of topological charge, from which chiral phenomena can emerge. [42]

The Lagrangian (2.1) is symmetric with respect to space parity $\mathcal{P}$ and charge conjugation $\mathcal{C}$ transformations. It is also invariant under local $SU(3)$ color transformations. Furthermore, in the massless fermion limit, the theory also has a global chiral symmetry $SU(3)_L \times SU(3)_R$, global baryon number symmetry $U(1)_V$, global axial charge symmetry $U(1)_A$, and the gluon and quark fields are scale-invariant.

The breaking of these classical symmetries–including in the massless fermion limit–by quantum and vacuum effects gives rise to various (special) phenomena, including confinement, asymptotic freedom, quantum anomalies, and spontaneous chiral symmetry breaking. This is primarily due to the interplay of the quantum axial anomaly and classical topologically non-trivial solutions that characterize the QCD vacuum [14, 21, 43]. In the next section, we further discuss the characteristics of the QCD vacuum and emergent phenomena.

In the latter half of this thesis, we turn our focus to gluon dynamics in the initial stages of heavy ion collisions. The Yang-Mills sector of QCD is matterless and describes only the gluonic gauge fields; therefore Eq. (2.1) reduces to the classical action

$$S_{\mathrm{YM}} = -\frac{1}{4}\int d^4x\ G^a_{\mu\nu}(x) G^{\mu\nu}_a(x). \tag{2.9}$$

We will return to the classical Yang Mills equations in Section 2.4 and Chapter 4.

Although the symmetries and symmetry-breaking features of QCD are well-established, the theory itself and its matterless counterpart are not analytically tractable and we must resort to numerical methods and approximations (e.g. effective field theories) to study their properties. Discretizing the theory on a Euclidean lattice and solving with Monte Carlo methods has been successful in computing properties such as the mass spectrum of hadrons, magnetic moments, and finite-temperature thermodynamic properties [44, 45].

Computing real-time features is significantly more challenging, since these cannot be trivially analytically continued from Minkowski spacetime to Euclidean spacetime. One example of this is the sphaleron transition rate, which we will define and describe in Section 2.3. Classical-statistical lattice simulations can also be performed to study the real-time dynamics of infrared excitations that describe gauge condensations. We employ this method in Chapter 4.

2.2 The chiral anomaly and the vacuum of gauge theories

Before we turn to the vacua of $SU(3)$, we first will discuss the chiral anomaly in the context of an abelian gauge theory. Quantum anomalies express the non-conservation of a quantity on the quantum level that is conserved at the classical level. A famous example of this is the chiral anomaly (Adler-Bell-Jakiw anomaly) which expresses the non-conservation of axial charge [18, 19]. The anomaly is reflected in the three-point function of the theory, and is therefore also referred to as the "triangle anomaly." This can be seen readily in textbook derivations (e.g. [46]): when the gauge theory is placed in an external gauge field, axial charge is not conserved.

The anomaly can clearly be understood when derived from the path integral measure via Fujikawa's method [47]. The method's guiding principle is that, in order to determine the invariance of an action under a symmetry, one must also ensure that the path integral measure is also invariant. For brevity, we will not discuss the full details of this method, but more information can be found in [47, 48].Fujikawa's method clearly exhibits the relationship between the Abelian chiral anomaly and the Atiyah-Singer index theorem[20]. In turn, it exposes the deep topological meaning of the anomaly.

We consider a Dirac operator $\not{D}$ for a spinor in the background of a fixed gauge field A_μ. The operator will have eigenspinors ϕ_n (with corresponding conjugates $\bar{\phi}_n$), and we can expand a general spinor ψ in terms of the product of eigenspinors and corresponding Grassmann-valued numbers. Since eigenspinors with distinct eigenvalues are orthogonals, eigenspinors with the same eigenvalues can be chosen to be orthogonal.

The fermion measure can then be rewritten in terms of these eigenspinors. Under a chiral transformation $\delta\psi = i\epsilon(x)\gamma^5\psi$, the fermion measure picks up a Jacobian factor,

$$J = \exp\left(-i\int d^4x\epsilon(x)\sum_x \bar{\phi}_n(x)\gamma^5\phi_n(x)\right), \tag{2.10}$$

which, when calculated, yields

$$\sum_n \bar{\phi}_n\gamma^5\phi_n = \frac{e^2}{32\pi^2}\epsilon^{\mu\nu\rho\sigma}F_{\mu\nu}F_{\rho\sigma}. \tag{2.11}$$

The transformation $\delta\bar{\psi} = i\epsilon(x)\gamma^5\bar{\psi}$ yields another factor of the Jacobian. The measure then transforms as

$$\int \mathcal{D}\psi\mathcal{D}\bar{\psi} \to \int \mathcal{D}\psi\mathcal{D}\bar{\psi}\exp\left(-\frac{ie^2}{16\pi^2}\int d^4x\epsilon(x)\epsilon^{\mu\nu\rho\sigma}F_{\mu\nu}F_{\rho\sigma}\right). \tag{2.12}$$

When evaluated, the axial current is not conserved and instead obeys the relation,

$$\partial_\mu J_A^\mu = \frac{e^2}{16\pi^2}\epsilon^{\mu\nu\rho\sigma}F_{\mu\nu}F_{\rho\sigma}. \tag{2.13}$$

For N_f massless Dirac fermions, the Abelian anomaly is generalized to

$$\partial_\mu J_A^\mu = \frac{e^2 N_f}{16\pi^2}\epsilon^{\mu\nu\rho\sigma}F_{\mu\nu}F_{\rho\sigma}. \tag{2.14}$$

2.2.1 The Atiyah-Singer index theorem

The seminal results of Atiyah and Singer equated the analytic index of an elliptic complex with the topological index of its corresponding fiber bundle [20, 49]. In this subsection, we will elucidate its importance in physical theories described by Abelian and non-Abelian gauge theories and the topological meaning of the respective anomalies.

Let us consider the Dirac operator in Euclidean space in the background of a general gauge field A_μ. Since the Dirac operator $i\not{D}$ is Hermitian, it has real eigenvalues,

$$i\not{D}\phi_n = \lambda_n\phi_n, \qquad \lambda_n \in \mathbb{R}. \tag{2.15}$$

When the eigenvalues for some eigenfunction ϕ_n are nonzero, then $\gamma^5\phi_n$ is also an eigenfunction, since $\gamma^\mu\gamma^5 = -\gamma^5\gamma^\mu$ (for $\mu = 1, ..., 4$), and

$$i\not{D}(\gamma^5\phi_n) = -i\gamma^5\not{D}\phi_n = -\lambda_n\gamma^5\phi_n. \tag{2.16}$$

It is clear that non-zero eigenvalues come in pairs $\pm\lambda_n$ and that ϕ_n and $\lambda^5\phi_n$ are orthogonal functions.

However, this does not apply to the zero eigenvalues and the zero modes. In general, if ϕ_n and $\gamma^5\phi_n$ have the same zero eigenvalue, then $i\not{D}$ and γ^5 can be simultaneously diagonalized. Since $(\gamma^5)^2 = 1$, its possible eigenvalues are ±1. Let's define n_+ and n_- to be the number of zero modes of $i\not{D}$ with the γ^5 eigenvalues ±1, respectively. By definition, the index of the Dirac operator is

$$\text{Index}(i\not{D}) = n_+ - n_-. \tag{2.17}$$

To connect this to the Abelian chiral anomaly, we recall Eq. (2.11). Compactifying this theory on a four-manifold leads to the discretization of the spectrum. Then we can integrate Eq. (2.11),

$$\int d^4x \sum_n \bar{\phi}_n \gamma^5 \phi_n = \frac{e^2}{32\pi^2} \int d^4x \epsilon^{\mu\nu\rho\sigma} F_{\mu\nu} F_{\rho\sigma}. \tag{2.18}$$

Only the zero modes will contribute to the left-hand side of this equation, since whenever the eigenvalues are nonzero ϕ_n and $\gamma^5\phi_n$ are orthogonal. Therefore, we can say

$$\int d^4x \sum_n \bar{\phi}_n \gamma^5 \phi_n = n_+ - n_-, \tag{2.19}$$

and finally equate

$$\mathrm{Index}(i\not{D}) = \frac{e^2}{32\pi^2} \int d^4x \epsilon^{\mu\nu\rho\sigma} F_{\mu\nu} F_{\rho\sigma}. \tag{2.20}$$

Let us now consider the space $\mathbb{R} \times X$, in which X is a closed spatial 3-manifold. We can also define the axial charge $J_A = \int_X j_A^0$ and parameterize $\mathbb{R}$ by t. In this case, the integrated anomaly equation tells us about the change in the charge,

$$\Delta J_A = J_A\Big|_{t=+\infty} - J_A\Big|_{t=-\infty} = \frac{e^2}{16\pi^2} \int d^4x \epsilon^{\mu\nu\rho\sigma} F_{\mu\nu} F_{\rho\sigma}. \tag{2.21}$$

The l.h.s. must be an integer due to quantum mechanics. On the other hand, the r.h.s. must be an integer due to topology. This example is the essence of the Atiyah-Singer index theorem, where an analytic index is equated to a topological one. The axial anomaly bridges these ideas in this spirit.

This also holds in non-Abelian gauge theories, which we will associate with the collective effects of sphaleron damping.

2.2.2 Vacua in non-Abelian gauge theories

Let us consider Yang-Mills theory in the temporal gauge $A_0 = 0$, and let $\mathcal{G}$ be the set of time-independent gauge transformations $g(\mathbf{r})$. If we consider Euclidean space $\mathbb{R}^3$ and add the point at infinity, the space becomes compactified to a three-sphere, $\mathbb{R}^3 \cup \{\infty\} \simeq S^3$. The compactification amounts to requiring that all fields and gauge transformations have well-defined limits as $|\mathbf{r}| \to \infty$. The residual gauge transformations in $\mathcal{G}$ then define maps from S^3 onto the gauge group,

$$\mathcal{G} = \{g : S^3 \to G\}. \tag{2.22}$$

Now let $\mathcal{G}_0 \subset \mathcal{G}$ be the subgroup of $\mathcal{G}$ that contains all transformations in $\mathcal{G}$ that can be smoothly deformed into the identity. The theory will have topological sectors if [46]

$$\mathcal{G}/\mathcal{G}_0 \neq \mathbf{1}. \tag{2.23}$$

In $3+1$ dimensional gauge theories, one turns to the homotopy group associated with the spatial dimension (3) to determine whether or not these topological sectors appear. For example, for $SU(2)$ in 3+1 dimensions, $\pi_3(S^3) = \mathbb{Z}$. Then, we deduce that these topological sectors appear and are labelled by an integer, which is, in this case, the topological winding number.

The gauge group for QCD is the simply-connected, compact Lie group $SU(3)$, but it is sufficient to consider the mapping of the $SU(2)$ subgroup of $SU(3)$ onto the three-sphere S^3. The integer that indexes the topologically inequivalent vacua in QCD is referred to as the topological charge, or Chern-Simons number N_{CS}.

Because the vacua are topologically inequivalent, transitions between the vacua with different N_{CS} are topologically nontrivial. Transitions between vacua have physical ramifications associated with the generation and erasure of axial charge [17, 50].

We show this by first defining the Chern-Simons number,

$$N_{CS} = \int d^3x \; K^0(t, x), \tag{2.24}$$

where K^0 is the temporal component of the Chern-Simons current,

$$K^\mu = \frac{g^2}{32\pi^2}\epsilon^{\mu\nu\alpha\beta}\left(A^a_\nu G^a_{\alpha\beta} - \frac{g}{3}f_{abc}A^a_\nu A^b_\alpha A^c_\beta\right). \tag{2.25}$$

The spatial integral over the four-divergence of the Chern-Simons current defines a total time derivative. Therefore, K^μ can be expressed as the difference of two boundary terms,

$$\int_{t_1}^{t_2} dt \int d^3x \; \partial_\mu K^\mu = N_{CS}(t_2) - N_{CS}(t_1), \tag{2.26}$$

which is precisely the change in Chern-Simons number. We can also express the divergence of the Chern-Simons current in terms of the topological Chern-Pontryagin charge,

$$\partial_\mu K^\mu = \frac{g^2}{32\pi^2} G^a_{\mu\nu}\tilde{G}^{\mu\nu}_a. \tag{2.27}$$

In $SU(N_c)$ gauge theories with N_f flavors of light quarks, the conservation of axial current associated with each quark species

$$j^\mu_{A,f} = \bar{q}_f \gamma^\mu \gamma_5 q_f \tag{2.28}$$

is violated due to both the chiral anomaly and the symmetry-breaking associated with non-zero quark mass m_f. The quark mass can be neglected in the high temperature phase of a QCD plasma. The non-conservation of axial charge is expressed by the chiral anomaly equation,

$$\partial_\mu j^\mu_{A,f} = -\frac{N_f g^2}{16\pi^2} G^a_{\mu\nu} \tilde{G}^{\mu\nu}_a, \tag{2.29}$$

where

$$G^a_{\mu\nu} = \partial_\mu A^a_\nu - \partial_\nu A^a_\mu + g f^{abc} A_{\mu\ b} A_{\nu\ c} \tag{2.30}$$

is the non-Abelian field strength tensor and $\tilde{G}^{\mu\nu}_a$ is its dual.We can relate the anomaly equation to the four-divergence of the Chern-Simons current via Eq. (2.27),

$$\int d^3x \ j^0_A(t_2) - \int d^3x \ j^0_A(t_1) = -2N_f \int_{t_1}^{t_2} dt \int d^3x \ \partial_\mu K^\mu. \tag{2.31}$$

The left hand side of Eq. (2.31), when non-zero, refers to an axial charge imbalance, or the generation of axial charge. Comparing Eq. (2.26) and Eq. (2.31), it is clear that the generation of axial charge is directly associated with the change in N_{CS}.

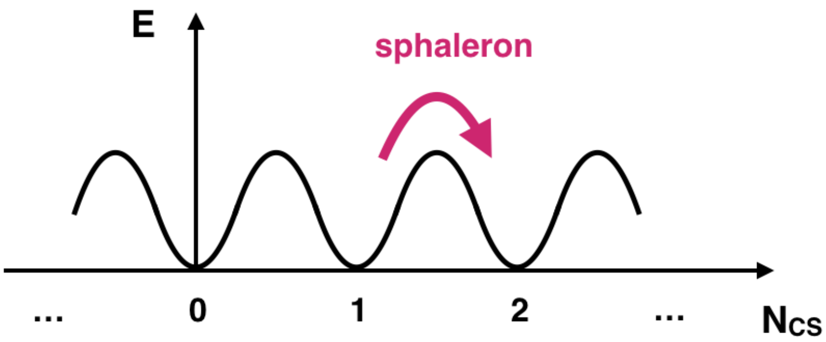

Figure 2.1: Visualization of the sphaleron transition in the periodic QCD vacuum. Transitions between topologically inequivalent vacua (labeled by N_{CS}) can occur through quantum tunneling, or in a system with high temperatures like a QGP, can be thermally activated by a sphaleron transitions.

2.3 Sphaleron transitions

At finite temperature, transitions between vacua with different topological charge are activated thermally by finite-energy sphaleron configurations [15]. In Figure 2.1, we show a visual representation of sphaleron transitions in the periodic QCD vacuum. Sphaleron transitions are abundant in QCD at high temperatures, such as in the QGP. However, determining the rate of sphaleron transitions from first-principles is complicated because sphaleron transitions are real-time processes [16, 51].

Individual sphaleron transitions are not correlated with each other, so we characterize the long-time behavior of N_{CS} by an integer random walk between topological sectors. Therefore, the sphaleron transition rate is the probability of a change in Chern-Simons number per unit spacetime volume and time [16]:

$$\Gamma_{\rm sph} = \lim_{t\to\infty} \frac{\langle \Delta N_{CS}^2 \rangle}{Vt} = \int d^4x \left\langle \frac{g^2}{32\pi^2} G^a_{\mu\nu}\tilde{G}^{\mu\nu}_a(x) \frac{g^2}{32\pi^2} G^a_{\alpha\beta}\tilde{G}^{\alpha\beta}_a(0) \right\rangle. \tag{2.32}$$

The sphaleron transition rate is set by the zero frequency and momentum limit of the $G\tilde{G}$ Wightman function in Minkowski spacetime. Analytically continuing Eq. (2.32) to Euclidean spacetime shows that the calculation of the zero-frequency Euclidean correlation function for the Euclidean topological susceptibility corresponds to the zero-frequency Minkowski retarded function. This is not the quantity that sets the sphaleron rate; that is the zero-frequency and momentum limit of the Wightman function.

In other words, the Euclidean frequency-domain correlation function continues to a Minkowski frequency-domain function with the wrong operator ordering [16]. Although one can relate the Euclidean function to the Wightman function through the Kramers-Kronig relations, eventually this yields an integral relation that would need to be inverted in order to extract the correct quantity on the lattice. Such problems have also plagued the evaluation of other transport coefficients such as electric conductivity and shear viscosity [52].

The accepted estimate for $SU(N_C = 3)$ gauge theory at weak coupling was determined in [16] by exploiting the weak coupling relation between the sphaleron rate and the topological diffusion rate for classical lattice gauge theory,

$$\Gamma_{\text{sph}} = (132 \pm 4) \left(\frac{g^2 T^2}{m_D^2} \right) \left(\ln \frac{m_D}{\gamma} + 3.0410 \right) \alpha_s^5 T^4, \tag{2.33}$$

where $\alpha_S = g^2/4\pi$ and

$$\gamma = \frac{3g^2 T}{4\pi} \left(\ln \frac{m_D}{\gamma} + 3.041 \right), \tag{2.34}$$

$$m_D^2 = \frac{6 + N_f}{6} g^2 T^2. \tag{2.35}$$

The quantity γ is the mean rate of color randomization. It is defined self-referentially and was found self-consistently [16].

More recently, a high-precision lattice calculation of the sphaleron transition rate was performed on large, fine-grained lattices in the quenched approximation at $T = 1.5T_c$ [53]. These calculations determined the sphaleron transition rate to be on the order of $\Gamma_{\text{sph}} = (0.02 - 0.2)T^4$. The large systematic uncertainties come from the analytic continuation of Euclidean functions to Minkowski space, which is usual for these types of calculations. However, the large value determined in this study and the discrepancy with previous calculations highlights the difficulty in computing the sphaleron transition rate, especially in physically relevant regimes for heavy ion collisions.

In the strong-coupling regime, the sphaleron rate can be determined via the Ads/CFT correspondence for a $\mathcal{N} = 4$ Supersymmetric Yang-Mills plasma [54]. The rate was determined to be

$$\Gamma_{\text{sph}} = \frac{(g^2 N)^2}{256\pi^3} T^4, \tag{2.36}$$

which indicates that the occurrence of sphaleron transitions becomes more frequent in the strong coupling limit.

2.3.1 Chiral Phenomena

Inevitably, the non-trivial interplay between external gauge fields and the quantum chiral anomaly has physical consequences. Quantum phenomena non-trivially affect systems possessing chiral fermions, from quark-gluon plasma (QGP) to Dirac semimetals [55].

In the presence of an external Abelian magnetic field, in a system with a chirality imbalance, electric charges separate along the direction of the magnetic field via the chiral anomaly. This is the Chiral Magnetic Effect (CME) [21]. An analogous separation of axial charges along the magnetic field can occur if fluctuations of vector charge occur in this system, called the Chiral Separation Effect (CSE). In fact, fluctuations of axial and vector charge mutually induce each other to form a collective excitation known as the Chiral Magnetic Wave (CMW) [23]. The CMW propagates along the direction of the magnetic field.

These chiral phenomena were shown by Son and Surówka [22] to emerge in the framework of relativistic hydrodynamics when the triangle anomaly was accounted for within the equations of motion. Relativistic hydrodynamics also gives rise to other chiral phenomena, including phenomena related to the global vorticity of a fluid, known as Chiral Vortical Effects (CVEs)[22].

In ultra-relativistic heavy ion collisions, a high-temperature QCD plasma consisting of deconfined quarks and gluons is produced called "quark-gluon plasma" (QGP). These heavy ion collisions also produce very strong magnetic fields in non-central heavy ion collisions. The presence of strong magnetic fields makes QGP a good laboratory for the study of chiral phenomena, as chiral phenomena emerge from the interplay of the global topology with a background Abelian magnetic field.

2.3.2 Chirality transfer in non-Abelian gauge theories

In this chapter, we established that in gauge theories with chiral fermions, the axial charge density is manifestly not conserved. Based on this discussion, it is important to comment on the transfer of net chirality in a system from the fermionic to gauge degrees of freedom.

Mechanisms of chirality transfer in Abelian gauge theories like QED are well established [56–59]. Fluctuations of electric and magnetic fields deplete the net axial charge density of a system such as an electromagnetic plasma. In order for chiral transport phenomena to persist in such a system, an external electromagnetic field must be applied. On the other hand, when there is no external field applied, the chirality is transferred from the fermion sector to the gauge sector. This process proceeds via the exponential growth and decay of helical gauge fields due to chiral plasma instabilities. When the growth of an instability saturates, a self-similar turbulent cascade results in the generation of large scale helical gauge fields [56, 59–61]. This has been studied in various ways, from weak coupling techniques [57, 58, 62, 63] to effective macroscopic descriptions [56, 64, 65] to non-perturbative real-time lattice simulations [59, 66, 67].

The story is naturally more complicated in non-Abelian gauge theories, such as in QCD or the electroweak sector of the standard model. Topological transitions like sphaleron transitions tend to erase net axial charge present in the fermion sector[15, 68]. It follows that sphaleron transitions play an important role in our understanding of the real-time dynamics of chiral transport phenomena, which play a role in theories of Baryo- and Leptogenesis in the early universe [69–71]. A recent paper [50] reported on the first microscopic study of chirality transfer in non-Abelian plasmas. This study established that the primary driver of chirality transfer in non-Abelian plasmas is these topological transitions.

2.3.3 Experimental search for chiral phenomena

Experimental observation and study of chiral phenomena is a direct probe of gauge field topology. Such phenomena are ubiquitous in nature and there are two current avenues being explored: in heavy ion collisions and in Dirac and Weyl semimetals [30]. There is also closely related phenomena expected to occur in the Early Universe, expected to lead to the generation of primordial magnetic fields [28].

The experimental searches for chiral phenomena at the Relativistic Heavy Ion Collider (RHIC) at Brookhaven National Laboratory and at the Large Hadron Collider (LHC) at CERN are ongoing [72]. In heavy ion collisions, the CME, for example, manifests as a separation of positively and negatively charged hadrons along the direction of the magnetic field induced by the collision. The search is plagued by many sources of uncertainty, both on the experimental and theoretical side. A major source of uncertainty with experimental efforts stems from the measurements of charge separation. Background effects, for example, are induced by elliptic flow coupled to two-particle correlations.

Part of the 2018 isobar run at the RHIC was dedicated to the search for the CME. Using RuRu and ZrZr isobar collisions was suggested to allow for an independent manipulation of the magnetic field to significantly reduce background interference with a statistically-significant CME signal. The similar size and shape of the nuclei were thought to produce a similar background, but the difference in electric charge of Ru and Zr would result in a different induced magnetic field and therefore a different observed CME signal.[72, 73]The first blind analysis results from the STAR experiment were released in [74]. The STAR Collaboration performed a blind analysis of a data sample of several billion isobar collisions of $RuRu$ and $ZrZr$ at $\sqrt{s_{NN}} = 200$ GeV, based on the methodology presented in [75]. While the results presented are inconsistent with the presence of the CME, the conclusions of the STAR team should also be approached with care due to several factors, primarily with hadron multiplicity and collective flow taken into account [76].

With the discovery of three-dimensional Dirac semimetals Cd_3As_2 and Na_3Bi [30], the experimental frontier for the discovery of chiral transport phenomena widened to include condensed matter experiments. In Dirac systems in parallel electric and magnetic fields, the CME emerges via a positive contribution to the conductivity with a quadratic dependence on the magnetic field. The CME is proportional to the product of the chirality imbalance and the magnetic field, the former of which is generated dynamically through the anomaly with a rate proportional to the product of electric and magnetic field. This leads to a negative longitudinal magnetoresistance [30].

One of the first experiments measured magneto transport in zirconium pentatelluride $ZrTe_5$. They observed a large negative magnetoresistence when the magnetic field is parallel to the current. Additionally, the magnetoconductance has a quadratic field dependence, which is a clear indication of the chiral magnetic effect [21, 77]. Since then, various experiments have been performed regarding magnetotransport in Dirac semimetals and have reported strong evidence for the CME [30, 77].

2.4 Initial stages far from equilibrium

In the initial stages of a heavy ion collision, in the transverse plane, the initial production of quarks and gluons is described by the color glass condensate (CGC) effective field theory [78, 79]. In this phase the gluons can saturate and generate a large scale saturation scale, $Q \gg \Lambda_{\mathrm{QCD}}$.

In the CGC theory, the incoming nuclei are highly length-contracted by an ultrarelativistic factor $\gamma \gg 1$. The incoming nuclei are described as sheets of colored glass because these sheets are composed of colored gluons and the classical gluon field is created by fast-moving sources, akin to how glasses are in general described as systems that evolve slowly compared to natural time scales. The gluon distribution has a maximal phase space density for momentum modes that are softer than the saturation momentum, as strong gluon fields are self-generated by the nuclei [80]. The density of gluons per transverse area and rapidity in the wave functions of the nuclei increases with collision energy. Let dN/dy be the number of gluons per rapidity y. Then the density of gluons per transverse area and rapidity in the wave functions of the nuclei is $(dN/dy)/\pi R_A^2$, where R_A is the nuclear radius. The transverse density of gluons determines the saturation momentum scale Q, which becomes very large at high energies compared to Λ_{QCD},

$$Q^2 \sim \frac{\alpha_s}{\pi R_A^2} \frac{dN}{dy} \gg \Lambda_{\mathrm{QCD}}. \tag{2.37}$$

The saturation momentum sets the momentum scale for the transverse momentum distribution of partons in the nuclei wave functions. When $Q \gg \Lambda_{\mathrm{QCD}}$, the coupling constant is small, such that $\alpha_s(Q) \ll 1$. One can then treat the evolution of the system with weak coupling methods. On the other hand, the number of gluons per phase space cell in the incoming wave functions, given by

$$\frac{1}{\pi Q^2 R_A^2} \frac{dN}{dy} \sim \frac{1}{\alpha_s} \gg 1, \tag{2.38}$$

is large and can be treated as classical in this regime of the evolution. The production and initial evolution of gluons are determined by solving the classical Yang-Mills equations.

2.4.1 Classical-statistical simulations

In practice, we can map this non-perturbative problem to a classical-statistical problem [81–84]. Classical-statistical problems can be solved using real-time lattice simulations. In such simulations, the system is initialized with quantum initial conditions and the dynamics are then approximated with a classical evolution.

The classical equations of motion are derived from the principle of stationary action,

$$\frac{\delta S[A]}{\delta A^a_\mu} = 0, \tag{2.39}$$

in which $S = \int d^4x\mathcal{L}$. From this equation and the Yang-Mills Lagrangian (2.9), the classical Yang-Mills equations are

$$[D_\mu, F^{\mu\nu}] = 0. \tag{2.40}$$

One can fix the residual gauge freedom by taking the temporal gauge, $A_0 = 0$. On the discretized lattice, temporal gauge links go to unity, so it is a convenient choice when evaluated on the lattice. In the continuum, the equations of motion are

$$\partial_t A_i = E_i, \tag{2.41}$$

$$\partial_t E_i = -D_j F_{ji}, \tag{2.42}$$

where E_i are the algebra-valued, conjugate momenta that are identified in Yang-Mills theory as chromoelectric fields. In order to simulate this on the lattice, the non-Abelian Gauss law constraint must be obeyed,

$$D_i E^i = 0. \tag{2.43}$$

The discretized versions of the equations of motion are derived from the classical Yang-Mills Hamiltonian derived by Kogut and Susskind [85] or the Wilson-Gauge action [39, 86].[2]

We utilize classical-statistical simulations in Chapter 4 and describe details of our set up in Section 4.1.

2.4.2 Hierarchy of scales far from equilibrium

In thermal equilibrium at high temperature T, the weakly-coupled QCD plasma exhibits a hierarchy of scales: hard momenta $\sim T$ that dominate the energy density of the system, a soft electric screening (Debye) scale $\sim gT$, and an ultrasoft magnetic screening scale $\sim g^2T$, where $g^2 = 4\pi\alpha_s \ll 1$.

---

[2] The simulations utilized in Chapter 4 use the Kogut-Susskind method.

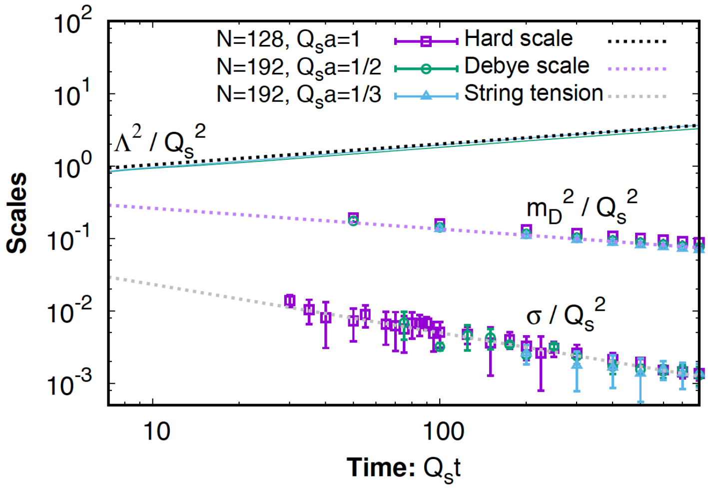

FIGURE 2.2: Time evolution of the hard scale (λ^2), the electric screening/Debye scale (m_D^2), and the spatial string tension/magnetic scale (σ) far from equilibrium. A dynamical separation of scales is clearly visible. Figure from [2]

Far from equilibrium, such a separation of scales also exists in the vicinity of the non-thermal attractor, the self-similar scaling regime of highly occupied plasmas that is insensitive to the initial conditions and the exact value of the coupling [3, 41, 86–92].

The hard scale, which dominates the system's energy density, scales as $\Lambda(t) \sim t^{1/7}$, the soft electric screening (Debye) mass follows $m_D(t) \sim t^{-1/7}$, and the ultrasoft magnetic screening scale evolves as $\sqrt{\sigma}(t) \sim t^{-\zeta/2}$, which is associated with the string tension σ and with the sphaleron transition rate [2, 3, 41, 87, 91, 93]. These characteristic momentum scales are initially of the same order Q_s, but the self-similar evolution leads to a dynamical separation of scales over time, such that $\sqrt{\sigma}(t) \ll m_D(t) \ll \Lambda(t)$, as shown in Figure 2.2. Interestingly, the ultrasoft scale approaches zero faster than the Debye screening scale.

The ultrasoft magnetic scale sets the time scale for the build up of a gauge condensate, which will be discussed in Chapter 4. Below the threshold set by the magnetic scale, at ultrasoft momenta, occupation numbers are expected to be $f \sim 1/\alpha_s$. Therefore, the dynamics is non-perturbative.

In the equilibrium plasma, the spatial Wilson loop provides the scale that determines the magnetic screening. Therefore, it can be used to study the non-equilibrium temporal evolution, from which the scaling exponent that controls the screening can be extracted. It follows that the corresponding dynamical string tension of the classical theory can be derived from this as well. In general, the Wilson loop is an extended object that is used to probe non-perturbative, infrared behavior of non-Abelian gauge theories. The spatial Wilson loop has been shown to characterize a universal state of QCD matter far from equilibrium [41]. In the following subsection, we will describe the basic properties of the Wilson loop.

2.4.3 Wilson loops

The fundamental properties of Wilson loops are best described in the geometric language of fiber bundles. The gauge theory is itself a fiber bundle, and a gauge field A_μ is a connection, which can be written in terms of its color indices as $(A_\mu)_i^j = A_\mu^a (T^a)_i^j$.

To better understand the Wilson loop, let us first consider a test particle that carries some internal degree of freedom such as electric charge, denoted by a complex vector q of fixed length, such that for q_i, $q^\dagger q$ is constant, and $i = 1, ..., \text{dim}R$. The charge sits in a representation R of the Lie group G. In QCD, the charged test particle is a quark with chromoelectric charge q_i. As the particle moves around the manifold, the connection tells the charge vector how to rotate, or how the vector parallel transports. If the test particle is transported around a closed loop $\mathcal{C}$, it obtains a phase given by $\exp\{i \oint_{\mathcal{C}} A\}$.

Precisely, in a non-Abelian gauge theory, for some particle moving with a worldline $x^\mu(\tau)$, the rotation of the vector q is governed by the parallel transport equation,

$$i \frac{dq}{d\tau} = \frac{dx^\mu}{d\tau} A_\mu(x) q, \tag{2.44}$$

where we consider A_μ to be Hermitian such that the length $q^\dagger q$ is constant. Now suppose that the particle is moving along curve $\mathcal{C}$ from time $\tau = \tau_i$ to $\tau = \tau_f$. The rotation of the vector and therefore the parallel transport depends on the starting and ending points, and the path between them. We relate $q(\tau_f)$ to $q(\tau_i)$ via

$$q(\tau_f) = U[x_i, x_f; \mathcal{C}] q(\tau_i), \tag{2.45}$$

where U is a *Wilson line*, defined as the path-ordered exponential,

$$\begin{aligned} U[x_i, x_f; \mathcal{C}] &= \mathcal{P} \exp\left(i \int_{\tau_i}^{\tau_f} d\tau \frac{dx^\mu}{d\tau} A_\mu(x(\tau)) \right), \\ &= \mathcal{P} \exp\left(i \int_{x_i}^{x^f} A \right), \end{aligned} \tag{2.46}$$

where $\mathcal{P}$ denotes path-ordering. The Wilson line, under a gauge transformation $\Omega(x)$, transforms as

$$U[x_i, x_f; \mathcal{C}] \to \Omega(x_i) U[x_i, x_f; \mathcal{C}] \Omega^\dagger(x_f). \tag{2.47}$$

If the test particle is moving on a closed loop, the Wilson line is referred to as a Wilson *loop*, and it quantifies how the charge vector q differs from its starting value. In other words, the Wilson loop is a holonomy. It is usually written as

$$W[\mathcal{C}] = \mathrm{tr}\mathcal{P}\exp\left(i\oint A\right). \tag{2.48}$$

Like the Wilson line, it depends on the representation of the gauge field and its value along the (closed) path.

Returning to QCD, the Wilson loop can be viewed as an operator that transports a chromoelectrically-charged particle around a closed loop in spacetime. The particle is charged in the fundamental representation of the non-Abelian $SU(N_c)$ group such that the color-averaged transport around the closed loop is the path-ordered exponential,

$$W = \frac{1}{N_c}\mathrm{tr}\mathcal{P}\exp\left(ig\oint_{\mathcal{C}} dx^\mu A_\mu(x)\right), \tag{2.49}$$

where the gauge coupling is given by g and the indices μ run from 0 to 4. In thermal equilibrium, the theory is time translation invariant. Then the closed curve $\mathcal{C}$ includes the temporal direction, which is analytically-continued to imaginary values. The expectation value is a constant in time.

Area law behavior out of equilibrium The behavior of the spatial Wilson loop for large areas reflects the infrared properties of the strongly-correlated system.

In equilibrium at zero temperature, the expectation value of the Wilson loop in Yang-Mills theory decreases exponentially with the area A as

$$-\log\langle W\rangle_{\mathrm{eq.}} = \sigma_{\mathrm{eq.}}A, \tag{2.50}$$

where A is sufficiently large and $\sigma_{\mathrm{eq.}}$ is the equilibrium string tension that describes the rise of the static quark-anti-quark potential for large spatial separation. At zero temperature, spatial Wilson loops and their spatio-temporal counterparts show the same area law behavior. However, unlike their spatio-temporal counterparts, the spatial Wilson loops exhibit this behavior in the de-confined high temperature phase, in the vicinity of the self-similar regime far from equilibrium. Here, this area law behavior reflects non-perturbative gauge field configurations.

In Ref [41], a universal scaling exponent ζ is determined from the logarithm of the Wilson loop expectation value as a function of the area rescaled with time, $\log\langle W\rangle \sim At^{-\zeta}$. This is the scaling exponent for the ultrasoft magnetic scale, $\sqrt{\sigma(t)}$, which is the dynamical spatial string tension. This was determined by classical-statistical lattice simulations.

The simulations further determine that both $SU(2)$ and $SU(3)$ gauge theories show nearly identical infrared scaling exponents when properly normalized by their respective Casimir color factors.

2.4.4 Non-thermal fixed points and universality

Generally, in systems with a characteristic over-occupation of ultrasoft modes such as the non-equilibrium plasma formed in heavy ion collisions, the system can approach a transient solution independent of its initial conditions known as a non-thermal fixed point (NTFP) before it thermalizes. NTFPs represent non-equilibrium attractor solutions reached on a time scale that is much shorter than the thermalization time. Near the NTFP, the distribution function or correlator that describes these ultrasoft modes undergoes a self-similar evolution. During the self-similar evolution, the dynamics is controlled by a scaling function and corresponding scaling exponents.

When the scaling properties of different systems with different underlying microscopic theories coincide, they can be loosely grouped into universality classes. Some examples of similar over-occupied systems in extreme conditions include relativistic scalar systems that are used to model inflation and non-relativistic scalar systems that model the dynamics of ultracold quantum gases. These systems also approach NTFPs as they thermalize and exhibit nearly identical scaling properties and self-similar evolution.

Cosmological inflation models describe the early stage of the universe after the Big Bang. Some scenarios are modelled by scalar field theories featuring classical inflaton fields that decay due to instabilities from parametric resonances or tachyonic or spinoidal dynamics [94–96]. These instabilities can induce overoccupied excitations with transient dynamics, with a corresponding distribution that exhibit a self-similar evolution. In fact, the model exhibits different scaling regions that involve a dual cascade [94, 97, 98]. There is a direct energy cascade, in which energy is transferred to higher momenta, which drives the thermalization process. On the other hand, there is a particle cascade, in which particles evolve to lower momenta and occupy the zero mode, inducing a far from equilibrium Bose-Einstein condensate [5, 38].

These over-occupied conditions can also be prepared in table-top experiments featuring ultracold atomic gases [99]. In an optical trap, the dynamics of an interacting, non-relativistic Bose gas with density n and scattering length a can be probed. One can classify an over-occupied regime via some *diluteness parameter* and *coherence length*. The diluteness parameter $\zeta = \sqrt{na^3}$ indicates a regime in which the system exhibits this high-occupancy, according to the condition $\zeta \ll 1$. The coherence length is the inverse of the characteristic momentum scale $Q = \sqrt{16\pi an}$. In this system, Q is similar to the saturation momentum scale Q in heavy ion collisions, and the diluteness provides a dimensionless coupling parameter. The Bose cas is considered over-occupied when the occupancies $\sim 1/\zeta$ and when modes have momenta on the order of Q [99].

Additionally, universal caling has been experimentally discovered in other cold-atom systems [100–102]. In Refs. [100, 101], the non-equilibrium dynamics for magnetic hyperfine excitations of a spin-one Bose gas is tested in an elongated trap. A sudden change in the applied magnetic field is induced as a non-equilibrium instability and then the transverse spin is measured for three different initial conditions. Regardless of the initial conditions, a self-similar scaling regime emerges that is characterized by universal scaling exponents.

One of the outstanding questions is the extent to which these systems can be compared and how exactly we classify universality. A first step to this direct comparison can be taken when we can identify an order parameter in gauge theories that can be linked to the behavior of relativistic and nonrelativistic scalar fields. We investigate this further in Chapter 4.

Chapter 3

Sphaleron damping and charge transport in QCD plasmas

Chiral transport phenomena have recently attracted a significant amount of attention in experimental and theoretical studies, as they may have a significant impact on the collective dynamics of systems possessing (approximately) chiral fermions. Since such systems are ubiquitous in nature, possible manifestations of these phenomena occur across a diverse range of energy scales, with examples including the dynamics of baryo- and magnetogenesis in the early universe [28], the QGP in heavy ion collisions [29], and Dirac and Weyl semimetals in condensed matter systems [30].

Ordinary transport phenomena describe the macroscopic dynamics of conserved energy-momentum and (vector) charges on large time and distance scales. Novel chiral transport phenomena, on the other hand, are linked to the dynamics of axial charges, which generically are not conserved due to quantum anomalies [18, 19]. Despite their expected importance in high temperature QCD plasmas, the effects of axial charge-changing processes in describing anomalous transport phenomena in heavy-ion collisions are frequently neglected in phenomenological studies [31] and have only been explored to a limited extent in the studies of [32, 33]. The primary objective of this study is to clarify the conditions under which anomalous charge transport in high-temperature QCD plasmas can be described macroscopically by anomalous relativistic hydrodynamics, and to explore the extent to which the non-conservation of axial charge due to QCD sphaleron transitions affects transport processes in a QCD plasma.

This chapter is based on Ref. [17] and is organized as follows. We begin with a general discussion of axial charge dynamics in high-temperature QCD plasmas in Section 3.1. Then, we establish the conditions under which a macroscopic description can be justified and subsequently in Section 3.2 demonstrate how to include axial charge changing processes due to sphaleron transitions in the anomalous hydrodynamic description of high-temperature QCD plasmas. Based on this framework, we demonstrate in Section 3.3 that sphaleron transitions have a non-trivial effect on the coupled hydrodynamic behavior of axial and vector charges in the presence of a magnetic field. Strikingly, we observe that the inclusion of the sphaleron damping term leads to the emergence of a wavenumber threshold that characterizes the hydrodynamic behavior of coupled charge modes and indicates the formation of Chiral Magnetic Waves (CMWs). Due to the particular form of the chiral anomaly, the dissipative effects due to sphaleron transitions also induce a non-trivial coupling between different species of chiral fermions, which we discuss using the example of the u, d light flavor sector of QCD. Subsequently, in Section 3.4, we investigate the sensitivity of axial and vector charge transport in the presence of a magnetic field to the sphaleron transition rate. We provide illustrative examples of vector and axial charge separation by numerically solving the linearized hydrodynamic equations, as well as an analytic expression for the vector charge separation in a space-time homogeneous plasma that elucidates its dependence on the sphaleron rate. We finally conclude in Section 3.5 with a summary of our findings and comments on the implications for the experimental search for chiral transport phenomena in heavy-ion collisions.

3.1 Chirality charge dynamics in high-temperature QCD plasmas

Specifically, for an $SU(N_c) \times U(1)$ gauge theory coupled to N_f flavors of massless Dirac fermions, which describes a high temperature QCD plasma in the presence of electromagnetic fields, the non-conservation of the axial current $j^{\mu}_{A,f}(x) = \bar{\psi}_f(x)\gamma^5\gamma^{\mu}\psi_f(x)$ of each fermion flavor takes the form of a local balance equation

$$\partial_{\mu} j^{\mu}_{A,f}(x) = -\frac{(eq_f)^2 N_c}{8\pi^2} F_{\mu\nu}(x)\tilde{F}^{\mu\nu}(x) - \frac{g^2}{16\pi^2} G^a_{\mu\nu}(x)\tilde{G}^{\mu\nu}_a(x), \tag{3.1}$$

where e, g are the $U(1)$ and $SU(N_c)$ gauge couplings, $F_{\mu\nu}$ and $G^a_{\mu\nu}$ denote the corresponding Abelian and non-Abelian field strength tensors, $\tilde{F}^{\mu\nu} = \frac{1}{2}\epsilon^{\mu\nu\alpha\beta}F_{\alpha\beta}$ and $\tilde{G}^{\mu\nu}_a = \frac{1}{2}\epsilon^{\mu\nu\alpha\beta}G^a_{\alpha\beta}$, are their duals and q_f is the electric charge of each fermion flavor. By recognizing the terms on the r.h.s. of Eq. (3.1) as the covariant divergence of the respective Chern-Simons currents, $\partial_{\mu}Q^{\mu}(x) = \frac{e^2}{16\pi^2}F_{\mu\nu}(x)\tilde{F}^{\mu\nu}(x)$, $\partial_{\mu}K^{\mu}(x) = \frac{g^2}{32\pi^2}G^a_{\mu\nu}(x)\tilde{G}^{\mu\nu}_a(x)$ the axial anomaly relation in Eq. (3.1) expresses the local conservation of the overall chirality of fermions $j^0_{A,f}$ and gauge fields $2q_f^2 N_c Q^0, 2K^0$ for each massless flavor. Since anomalous transport phenomena such as the chiral magnetic effect (CME) [21] only occur when a net chirality imbalance is present in the fermion sector ($j^0_{A,f} \neq 0$), it is thus important to understand how a chiral charge imbalance is transferred and re-distributed between fermions and gauge fields on the macroscopic time scales of interest.

Due to their expected importance, different mechanism of chirality transfer have been explored in the context of condensed matter physics [103], nuclear physics [50], and cosmology [67]. Straightforwardly, in QED plasmas or QED-like materials, a chiral charge imbalance in the fermion sector can be created via the application of (aligned) external electric and magnetic fields [30], while spacetime-dependent fluctuations of (chromo-)electromagnetic fields [2, 67] can generate local fluctuations of the chiral charge imbalance of fermions in QED and QCD plasmas. Conversely, a chirality imbalance in the fermion sector can generate chiral plasma instabilities in both QED and QCD plasmas [56, 61], which induce a transfer of chirality from fermions to gauge fields. However, on sufficiently large time and distance scales, the transfer of chirality in non-Abelian gauge theories, such as QCD, is believed to be dominated by so-called sphaleron transitions between different topological sectors of the $SU(N_c)$ gauge fields [2, 15, 16, 50].

By virtue of the non-trivial topology of the $SU(N_c)$ gauge field configurations in the physical real space $\mathbb{R}^3 \cup \{\infty\}$, non-Abelian gauge theories such as QCD feature an infinite number of topologically inequivalent but otherwise degenerate field configurations labelled by an integer Chern-Simons number $N_{CS} = \int d^3\mathbf{x}\ K^0(\mathbf{x})$. In high-temperature QCD plasmas, transitions between different topological sectors are thermally activated by finite-energy configurations called sphalerons. Sphaleron transitions between different topological sectors result in a change in N_{CS} by plus/minus unity, which according to Eq. (3.1) results in a change of the net-axial charge of fermions $J^0_{A,f} = \int d^3\mathbf{x}\, J^0_A(\mathbf{x})$ by plus/minus two units for each flavor. While in charge-neutral plasmas the dynamics of sphaleron transitions thus induces time dependent fluctuations of the chiral charge imbalance $J^A_0 = \sum_f j^0_{A,f}$ of fermions, sphaleron transitions in a chirally imbalanced plasma ($J^0_A \neq 0$) exhibit a bias towards erasing any pre-existing charge imbalance J^A_0 [15, 50], such that on asymptotically large time scales any chiral charge imbalance of fermions will disappear. Since a non-vanishing chiral charge imbalance is however required to realize chiral transport phenomena such as the chiral magnetic effect, one concludes that anomalous transport phenomena in high-temperature QCD plasmas are in a sense intrinsically non-equilibrium phenomena, which can only occur on transient time scales before the chiral charge imbalance is eventually erased.

The typical time scale for which a chiral charge imbalance can persist in a high-temperature QCD plasma therefore crucially depends on the rate of sphaleron transitions. Despite the fact that sphaleron transitions are known to occur in high-temperature QCD plasmas, it is notoriously challenging to compute the sphaleron rate from first principles [16, 51]. The sphaleron transition rate is defined as the thermal expectation value of the zero frequency, zero momentum limit of the Wightman correlation function of $G_{\partial_\mu K^\mu \partial_\mu K^\mu}(\omega, \mathbf{k})$ as

$$\Gamma_{\text{sph}} = \int d^4X \left\langle \frac{g^2}{32\pi^2} G^a_{\mu\nu}\tilde{G}^{\mu\nu}_a(X) \frac{g^2}{32\pi^2} G^a_{\alpha\beta}\tilde{G}^{\alpha\beta}_a(0) \right\rangle \tag{3.2}$$

and describes the occurrence of a Chern-Simons number-changing process per unit volume per unit time [16]. Evaluated at weak coupling for $SU(N_c)$ gauge theories, the sphaleron transition rate is parametrically given by $\Gamma_{\text{sph}} \propto \alpha_S^5 T^4$, where $\alpha_S = g^2/4\pi$ [16], while at strong coupling, the rate of sphaleron transitions is computed via the AdS/CFT correspondence for an $\mathcal{N} = 4$ Supersymmetric Yang-Mills plasma is given by $N \to \infty$: $\Gamma_{\text{sph}} = (g^2N)^2T^4/256\pi^3$[54]. Very recently, (quenched) lattice QCD calculations [53] have determined the sphaleron transition rates at temperatures $T = 1.5T_c$ to be on the order of $\Gamma_{\text{sph}} = (0.02 - 0.2)T^4$, with large systematic uncertainties stemming from the analytic continuation of Euclidean correlation functions to Minkowski space. Even though the estimated rates from lattice QCD are actually sizeable, we will demonstrate shortly that a more careful assessment of their magnitude suggests that an effective macroscopic description of axial charge transport in high-energy heavy-ion collisions may still be warranted.

3.2 Hydrodynamic description of anomalous transport in QCD-like theories

Although chiral transport phenomena in high-temperature QCD plasmas are in principle intrinsically non-equilibrium phenomena, their possible macroscopic manifestations also emerge naturally within the framework of anomalous hydrodynamics [22]. Indeed, if the process of axial charge equilibration is slow compared to the typical kinetic equilibration of the QCD plasma, the axial currents $j^{\mu}_{A,f}$ represent additional slow variables whose dynamics can be described macroscopically by introducing additional axial chemical potentials μ^{f}_{A} associated with the residual deviations of the axial charge $j^{0}_{A,f}$ from the genuine equilibrium state.

However, a meaningful hydrodynamic description based on an expansion around transient equilibrium states with non-vanishing axial chemical potentials ($\mu^{f}_{A} \neq 0$) can only be achieved if the equilibration of axial charge is slow compared to the equilibration of the system. This is the case for weakly-coupled $SU(N_c)$ plasmas, where the timescale of axial charge relaxation due to sphaleron transitions $\tau_{\text{sph}} \approx \frac{\chi_A T}{\Gamma_{\text{sph}}} \sim \alpha_S^{-5} T^3$ [16] is much larger than the timescale associated with the kinetic equilibration of the plasma, $\tau_{\text{kin}} \approx \frac{4\pi\eta/s}{T} \sim \alpha_S^{-2} T^{-1}$ [104]. When considering the QGP created in heavy ion collisions at RHIC and LHC energies, where temperatures typically range up to $\sim 4T_c$, one finds that with the estimate of $\Gamma_{\text{sph}} \approx 0.1T^4$ from [53] $\tau_{\text{sph}} \sim 10T^{-1}$ can be larger, but not significantly larger than $\tau_{\text{kin}} \approx 2T^{-1}$fm/c for favorable values of the transport coefficient $\eta/s = 0.16$ [105].

Now that we have established the anticipated range of applicability of an effective macroscopic description, we proceed to develop the hydrodynamic description of anomalous charge transport following previous works [22, 106]. We consider a viscous relativistic fluid in $3+1$ spacetime dimensions, governed by the Minkowski metric $g^{\mu\nu} = (-1, \mathbf{1})$, with conserved $U(1)$ vector currents[1] $j^{\mu}_{V,f} = \langle \bar{\Psi}_f \gamma^{\mu} \Psi_f \rangle$ and $U(1)$ axial currents $j^{\mu}_{A,f} = \langle \bar{\Psi}_f \gamma^{\mu} \gamma_5 \Psi_f \rangle$ that are not conserved due to the axial anomaly for N_f flavors of massless Dirac fermions. In the presence of a slowly-varying, non-dynamical background electromagnetic field, the conservation laws take the form

$$\partial_{\mu} T^{\mu\nu} = \sum_f e q_f F^{\nu\lambda} j^{V}_{\lambda,f}, \tag{3.3}$$

$$\partial_{\mu} j^{\mu}_{V,f} = 0, \tag{3.4}$$

$$\partial_{\mu} j^{\mu}_{A,f} = (e q_f)^2 C E^{\mu} B_{\mu} - \frac{g^2}{16\pi^2} G^{a}_{\mu\nu} \tilde{G}^{\mu\nu}_{a}, \tag{3.5}$$

---

[1] Note that the vector current is defined such that the electric current is $j^{\mu}_{\text{el,f}} = e q_f j^{\mu}_{V,f}$.

where the right hand side of Eq. (3.3) reflects work done on the system by the external electromagnetic field. Conversely, the right hand side of Eq. (3.5) reflects the non-conservation of axial charge, where effects due to the Abelian chiral anomaly are described explicitly by the term $(eq_f)^2CE^\mu B_\mu$ with the anomaly coefficient $C = N_c/2\pi^2$. Non-Abelian contributions to the axial anomaly are described by the last term in Eq. (3.5), which – in accordance with the discussion in Section 3.1 and Chapter 3 – tend to erase any pre-existing axial charge imbalance. By following the arguments of Shaposnikov, McLerran, and Mottola [15], the expectation value of $\left\langle \frac{g^2}{16\pi^2} G^a_{\mu\nu}\tilde{G}^{\mu\nu}_a \right\rangle$ can be expressed in terms of the sphaleron transition rate Γ_{sph} as

$$\left\langle \frac{g^2}{16\pi^2} G^a_{\mu\nu}\tilde{G}^{\mu\nu}_a \right\rangle = 4\Gamma_{\text{sph}} \sum_f \frac{\mu_{f,A}}{T} \,, \tag{3.6}$$

which in the presence of finite axial chemical potentials $\sum_f \mu_{f,A}$ is manifestly non-zero. We note that even though individual sphaleron transitions represent singular local events, which result in an integer change of the net axial charge, the macroscopic description in Eq. (3.5) is valid over large time and distance scales, where on average multiple sphaleron transitions provide a dissipative effect on the axial charge evolution of the fluid.

The electromagnetic fields are defined in Lorentz covariant form,

$$E^\mu = F^{\mu\nu}u_\nu, \qquad B^\mu = \frac{1}{2}\epsilon^{\mu\nu\alpha\beta}u_\nu F_{\alpha\beta}, \tag{3.7}$$

such that $u_\mu B^\mu = u_\mu E^\mu = 0$. Here, u^μ denotes the rest-frame velocity field, which, following Landau and Lifshitz, is defined as the timelike eigenvector of the energy momentum tensor: $-u_\mu T^{\mu\nu} = \epsilon u^\nu$ such that $u^2 = -1$. Besides u^μ, we use local temperature T and chemical potentials μ_{V_f/A_f} for each fermion flavor as thermodynamic variables. We also define the vorticity,

$$\omega^\mu = \frac{1}{2}\epsilon^{\mu\nu\alpha\beta}u_\nu \partial_\alpha u_\beta, \tag{3.8}$$

which must be included in the hydrodynamic description of anomalous relativistic fluids [22].

Next, to obtain the complete set of hydrodynamic equations of the system, we supplement Eqs. (3.3)-(3.5) with the constitutive relations for the vector/axial currents $j^\mu_{V/A,f}$ and the energy momentum tensor $T^{\mu\nu}$, which, in the most general form in the Landau frame, are written as

$$T^{\mu\nu} = (\epsilon + P)u^\mu u^\nu + P g^{\mu\nu} + \tau^{\mu\nu}, \tag{3.9}$$

$$j^\mu_{V,f} = n_{V,f} u^\mu + \nu^\mu_{V,f}, \tag{3.10}$$

$$j^\mu_{A,f} = n_{A,f} u^\mu + \nu^\mu_{A,f}, \tag{3.11}$$

where $\epsilon = \epsilon(T, \mu_{V,f}, \mu_{A,f})$ denotes the energy density and $P = P(T, \mu_{V,f}, \mu_{A,f})$ is the thermodynamic pressure. By definition, $\tau^{\mu\nu}$ satisfies the relation $u_\mu \tau^{\mu\nu} = 0$, and the dissipative currents $\nu^\mu_{V/A,f}$ are defined such that $u_\mu \nu^\mu_{V/A,f} = 0$ and $n_{V/A,f} = u_\mu j^\mu_{V/A,f}$ is the vector/axial charge density in the local rest frame of the fluid. We also note that, following the common practice in the field of heavy-ion physics, we take all of the above quantities to correspond to their expectation values, and we will not consider thermodynamic fluctuations in this study.

In this study, we restrict ourselves to studying the dissipative corrections $\tau^{\mu\nu}$ and $\nu^\mu_{V/A}$ up to first order in gradients of the hydrodynamic variables and external fields. The correction to Eq. (3.9) is then given by

$$\tau^{\mu\nu} = -\eta \sigma^{\mu\nu} - \zeta \Delta^{\mu\nu} \partial \cdot u, \tag{3.12}$$

which corresponds to ordinary first-order viscous corrections to energy-momentum transport, where η and ζ are the shear and bulk viscosity,

$$\sigma^{\mu\nu} \equiv \Delta^{\mu\alpha}\Delta^{\nu\beta} \left(\partial_\alpha u_\beta + \partial_\beta u_\alpha - \frac{2}{3} g_{\alpha\beta} \partial \cdot u \right) \tag{3.13}$$

is the transverse traceless symmetric shear-stress tensor, and $\Delta^{\mu\nu} = g^{\mu\nu} + u^\mu u^\nu$ denotes the spatial projector orthogonal to the direction of fluid flow. Similarly, the first order viscous corrections to Eqs. (3.10) and (3.11) take the following general form

$$\begin{aligned} \nu^\mu_{V,f} = &- \sigma^{ff'}_{VV} \left(T \Delta^{\mu\nu} \partial_\nu \frac{\mu_{V,f'}}{T} - e q_{f'} E^\mu \right) \\ &- \sigma^{ff'}_{VA} T \Delta^{\mu\nu} \partial_\nu \frac{\mu_{A,f'}}{T} + e q_f \sigma^f_{VB} B^\mu + \xi_{V,f} \omega^\mu, \end{aligned} \tag{3.14}$$

$$\begin{aligned} \nu^\mu_{A,f} = &- \sigma^{ff'}_{AV} \left(T \Delta^{\mu\nu} \partial_\nu \frac{\mu_{V,f'}}{T} - e q_{f'} E^\mu \right) \\ &- \sigma^{ff'}_{AA} T \Delta^{\mu\nu} \partial_\nu \frac{\mu_{A,f'}}{T} + e q_f \sigma^f_{AB} B^\mu + \xi_{A,f} \omega^\mu, \end{aligned} \tag{3.15}$$

and, if not stated otherwise, we will consider the various conductivity tensors to be diagonal in flavor space $\sigma^{ff'} = \sigma \delta^{ff'}$, to comply with the $SU(N_f) \times SU(N_f)$ flavor symmetry of a charge-neutral plasma in the chirally symmetric phase. We note that the various coefficients in Eqs. (3.14) and (3.15) have straightforward physical interpretations, where σ_{VV} and σ_{AA} are the vector and axial conductivities, while the "off-diagonal" transport coefficients σ_{VA} and σ_{AV} describe the coupled transport of axial and vector charges associated with the chiral electric separation effect [107], with $\sigma_{VA} = \sigma_{AV}$ due to the Onsager relations [108]. The other coefficients are related to anomalous chiral transport phenomena associated with the magnetic field and vorticity: σ_{BV} is the conductivity due to the chiral magnetic effect [21], σ_{BA} is the conductivity due to the chiral separation effect [24, 25], ξ_V is the coupling of the chiral vortical effect, and ξ_A is the spin-vorticity coupling[22].

Evidently, the transport coefficients in Eqs. (3.12)-(3.15) are constrained by the second law of thermodynamics, which requires local entropy production to be non-negative. Based on this requirement, it follows directly that the ordinary transport coefficients satisfy the relations $\eta \geq 0$ and $\zeta \geq 0$ for the shear and bulk viscosities in Eq. (3.12), as well as $\Gamma_{\rm sph} \geq 0$, $\sigma_{VV} \geq 0$ and $\sigma_{AA} \geq 0$, while $\sigma_{AV}\sigma_{VA} \leq \sigma_{AA}\sigma_{VV}$, for the sphaleron rate and the various conductivities in Eqs. (3.14) and (3.15). Strikingly, as pointed out in a seminal paper by Son and Surowka [22] and follow-up works [106], the various anomalous chiral transport coefficients in Eqs. (3.12)-(3.15) are constrained to an even greater extent by the same condition. To show this, we quantify entropy production via the entropy current,

$$S^\mu = su^\mu + D_B B^\mu + D_\omega \omega^\mu - \frac{\mu_{V,f}}{T}\nu^\mu_{V,f} - \frac{\mu_{A,f}}{T}\nu^\mu_{A,f}, \tag{3.16}$$

where s is defined by the thermodynamic relation $Ts = (\epsilon + P) - \mu_{V,f} n_{V,f} - \mu_{A,f} n_{A,f}$ and $D_{B,\omega}$ are general functions of temperature T and chemical potentials $\mu_{V/A,f}$. By exploiting the hydrodynamic equations and thermodynamic relations, we can then express the divergence of S^μ as (see Appendix A for details)

$$\begin{aligned}\partial_\mu S^\mu =& -\frac{1}{T}\partial_\mu u_\nu \tau^{\mu\nu} - \nu^\mu_{V,f}\left(\partial_\mu \frac{\mu_{V,f}}{T} - \frac{eq_f}{T}E_\mu\right) - \nu^\mu_{A,f}\partial_\mu \frac{\mu_{A,f}}{T} + 4\Gamma_{\rm sph}\left(\sum_f \frac{\mu_{A,f}}{T}\right)^2 \\ &- \left(\sum_f \frac{\mu_{A,f}}{T}(eq_f)^2\right) C E^\mu B_\mu + \partial_\mu \left(D_B B^\mu + D_\omega \omega^\mu\right),\end{aligned} \tag{3.17}$$

and require positive entropy production with the condition

$$\partial_\mu S^\mu \geq 0. \tag{3.18}$$

Dissipative effects due to shear (η) and bulk (ζ) viscous corrections, vector and axial charge diffusion ($\sigma_{V/AV/A}$), as well as sphaleron damping ($\Gamma_{\rm sph}$) contribute positively to entropy production. Deferring the details of the calculation to Appendix A (see also [22]), one finds that a thermodynamically consistent description of the anomalous transport phenomena associated with the coefficients $\sigma_{VB}, \sigma_{BA}, \xi_A, \xi_V$, requires these phenomena to be non-disspiative in the sense that their contribution to $\partial_\mu S^\mu$ vanishes identically. Based on this requirement, following the calculations in [22, 106], one obtains the following constraints on the anomalous transport coefficients in the single-flavor case:

$$\sigma_{VB} = C\left(\mu_A - \frac{n_V\mu_A\mu_V}{\epsilon+P}\right), \tag{3.19}$$

$$\sigma_{AB} = C\left(\mu_V - \frac{n_A\mu_A\mu_V}{\epsilon+P}\right) + (eq_f)^{-1}\frac{\partial}{\partial\overline{\mu}_A}g(\overline{\mu}_A), \tag{3.20}$$

$$\begin{aligned}\xi_A = C\left(\mu_V^2 - \frac{n_A\mu_A\mu_V^2}{\epsilon+P}\right) + (eq_f)^{-1}\frac{\mu_V}{T}\frac{\partial}{\partial\overline{\mu}_A}g(\overline{\mu}_A)\\ + \frac{\partial}{\partial\overline{\mu}_A}G(\overline{\mu}_A),\end{aligned} \tag{3.21}$$

$$\xi_V = 2C\left(\mu_V\mu_A - \frac{n_V\mu_A\mu_V^2}{\epsilon+P}\right) + (eq_f)^{-1}g(\overline{\mu}_A), \tag{3.22}$$

where $\overline{\mu}_A \equiv \mu_A/T$ and g and G are hitherto arbitrary functions of $\overline{\mu}_A$. These coefficients agree with the single flavor calculations by [22, 106] and with the conductivities calculated microscopically in the original works of [21–25, 106]. While the positivity of entropy production alone does not lead to such stringent constraints in the multiflavor case (see Appendix A), we will assume that individual quark flavors behave independently with respect to the chiral anomaly and entropy production and employ the same transport coefficients for the multiflavor case for respective quark flavors.

Next, we take these coefficients and insert them into the first order corrections to the constitutive relations in Eqs. (3.14) and (3.15). We can then take the constitutive relations with the conservation equations to obtain the closed set of hydrodynamic equations that govern the vector and axial charge dynamics in a high-temperature QCD plasma.

3.3 Hydrodynamic excitations in charge-neutral plasma

Now that we have established the effective macroscopic description of vector and axial charge transport in the presence of QCD sphaleron transitions, we will study the behavior of hydrodynamic excitations on a static equilibrium background, characterized by a fluid velocity field $u^\mu = (1, \mathbf{0})$, temperature T, and vanishing vector/axial charge chemical potentials $\mu_{V_f} = \mu_{A_f} = 0$, which is typical in high energy heavy ion collisions. In order to analyze the hydrodynamic equations, we first perform a spatial Fourier transform of the equations of motion, according to

$$u^i(t, \mathbf{x}) = \int \frac{d^3k}{(2\pi)^3} e^{i\mathbf{k}\cdot\mathbf{x}} u^i_{\mathbf{k}}(t, \mathbf{k}), \tag{3.23}$$

and similarly for the other fields, then subsequently linearize the equations of motion around the static equilibrium background. In the presence of an external magnetic field $\mathbf{B}$, the velocity field can be decomposed as

$$u^i = u_{\mathbf{k}} \frac{\mathbf{k}^i}{|\mathbf{k}|} + u_{\mathbf{B}} \frac{\mathbf{B}^i}{|\mathbf{B}|} + u_{\mathbf{k}\times\mathbf{B}} \frac{\mathbf{k}\times\mathbf{B}}{|\mathbf{k}\times\mathbf{B}|}, \tag{3.24}$$

such that the longitudinal and transverse components of the fluid velocity fields are given by

$$u_L = \frac{\mathbf{k}^i}{|\mathbf{k}|} u^i = u_{\mathbf{k}} + u_{\mathbf{B}} \cos(\theta_{\mathbf{kB}}), \tag{3.25}$$

$$u^i_\perp = u_{\mathbf{B}} \left(\frac{\mathbf{B}^i}{|\mathbf{B}|} - \cos(\theta_{\mathbf{kB}}) \frac{\mathbf{k}^i}{|\mathbf{k}|} \right) + u_{\mathbf{k}\times\mathbf{B}} \frac{(\mathbf{k}\times\mathbf{B})^i}{|\mathbf{k}\times\mathbf{B}|}, \tag{3.26}$$

and the transverse component can be further decomposed into two components:

$$u_{\perp\mathbf{B}} = u_{\mathbf{B}} \left(\frac{\mathbf{B}^i}{|\mathbf{B}|} - \cos(\theta_{\mathbf{kB}}) \frac{\mathbf{k}^i}{|\mathbf{k}|} \right), \tag{3.27}$$

$$u_{\perp\perp} = u_{\mathbf{k}\times\mathbf{B}} \frac{(\mathbf{k}\times\mathbf{B})^i}{|\mathbf{k}\times\mathbf{B}|}. \tag{3.28}$$

We choose the hydrodynamic variables to be fluctuations in energy density $\delta\epsilon = \delta T^{00}$, momentum density $\pi^i = \delta u^i(\epsilon + P) = \delta T^{0i}$, and charge densities $\delta n_{V,f} = \delta j^0_{V,f}$ and $\delta n_{A,f} = \delta j^0_{A,f}$, as these quantities can be defined microscopically in the underlying theory of QCD. By using thermodynamic relations, it is straightforward to express intensive variables from T, u^μ, and $\mu_{V/A}$ in terms of extensive ones; in particular we can express changes in charge density in terms of changes in chemical potential according to

$$\delta n_{i,f} = \chi^{ff'}_{ij} \delta\mu_{j,f'} \,, \qquad \chi^{ff'}_{ij} = \left(\frac{\partial^2 P}{\partial\mu_{i,f} \partial\mu_{j,f'}} \right)_T, \tag{3.29}$$

while changes of the pressure are determined by the equation of state as $\delta P = c_S^2 \delta\epsilon$. Since we are considering a charge-neutral background, all transport coefficients are evaluated at $\mu_{V,f} = \mu_{A,f} = 0$. We also assume $SU(N_f) \times SU(N_f)$ flavor symmetry, such that $\chi_{ij}^{ff'} = \chi_i \delta_{ij} \delta^{ff'}$. We note that in this situation, the "off-diagonal" transport coefficients, $\sigma_{VA} = \sigma_{AV}$ in Eqs. (3.14) and (3.15) also vanish, since the leading-order contributions are $\propto \mu_{A,f}\mu_{V,f}$ [107], i.e. of second order in the chemical potentials.

By imposing these conditions, we obtain the complete system of linearized hydrodynamic equations:

$$\partial_t \delta\epsilon + i|\mathbf{k}|\pi_L = 0, \tag{3.30}$$

$$\partial_t \pi_L + i|\mathbf{k}|c_s^2 \delta\epsilon + \frac{4}{3}\gamma_\eta \mathbf{k}^2 \pi_L = 0, \tag{3.31}$$

$$\partial_t \pi_{\perp B} + \gamma_\eta \mathbf{k}^2 \pi_{\perp B} = 0, \tag{3.32}$$

$$\partial_t \pi_{\perp\perp} + \gamma_\eta \mathbf{k}^2 \pi_{\perp\perp} - \sum_f ieq_f |\mathbf{k} \times \mathbf{B}| \left(D_V^f \delta n_{V,f} \right) = 0, \tag{3.33}$$

$$\partial_t \delta n_{V,f} + D_V \mathbf{k}^2 \delta n_{V,f} + ieq_f C \frac{\mathbf{k}\cdot\mathbf{B}}{\chi_A} \delta n_{A,f} = 0, \tag{3.34}$$

$$\partial_t \delta n_{A,f} + D_A \mathbf{k}^2 \delta n_{A,f} + ieq_f C \frac{\mathbf{k}\cdot\mathbf{B}}{\chi_V} \delta n_{V,f} = -\gamma_{\text{sph}} \sum_f \delta n_{A,f}, \tag{3.35}$$

where $\gamma_\eta = \eta/(\epsilon + P)$ is the shear diffusion coefficient, $D_i = \sigma_{ii}/\chi_i$ are the vector/axial charge diffusion coefficients and the coefficient $\gamma_{\text{sph}} = 4\Gamma_{\text{sph}}/(\chi_A T)$ describes dissipative effects due to sphaleron transitions. Since the right-hand side of Eq. (3.35) contains a sum over all flavors, this contribution leads to an explicit coupling of different flavor components, which tends to erase the net axial charge in the system.

We first observe that Eqs. (3.30) and (3.31) are coupled and describe sound waves, whereas Eq. (3.32) describes a purely diffusive shear mode. Eq. (3.33) is also a diffusive shear mode, coupled to Eqs. (3.34) and (3.35), which describe vector and axial charge density modes. We restrict our analysis to the coupled charge density equations, leaving out Eq. (3.33) as the vector charge density fluctuations feed into the shear mode but the shear mode does not feed back into the charge density equations at linear order.

3.3.1 Single flavor dynamics

Before we address the more complex situation of multiple flavors, we will analyze the effect of sphaleron transitions on the coupled vector and axial charge dynamics of a single fermion flavor ($N_f = 1$) with charge q_f in the presence of a magnetic field.

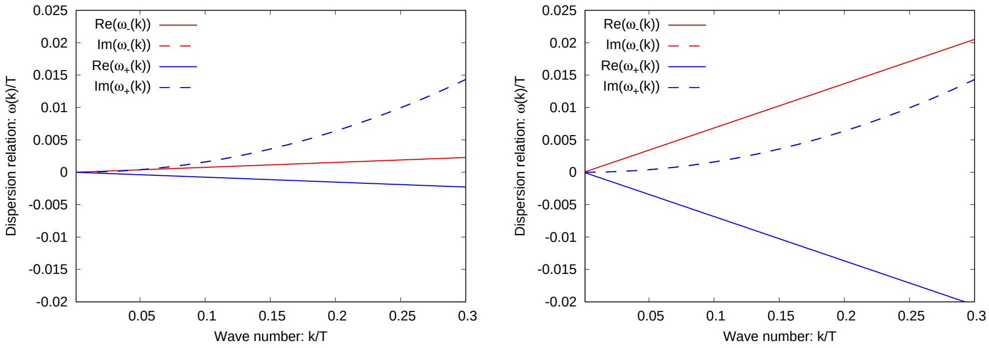

FIGURE 3.1: Single-flavor dispersion relations (3.38) for charge modes without dissipation from sphaleron transitions. The diffusion constant is fixed, so the behavior of the excitations depends on the wavenumber **k** and the magnetic field strength.

We rewrite Eqs. (3.34) and (3.35) in matrix form, using

$$M_{ab}^{N_f=1} = \begin{pmatrix} D\mathbf{k}^2 & ieq_f C\chi_A^{-1}\mathbf{k}\cdot\mathbf{B} \\ ieq_f C\chi_V^{-1}\mathbf{k}\cdot\mathbf{B} & D\mathbf{k}^2+\gamma_{\text{sph}} \end{pmatrix} \tag{3.36}$$

such that the fields $\phi_a = (\delta n_V, \delta n_A)$ satisfy the equation

$$\partial_t\phi_a + M_{ab}\phi_b = 0\ . \tag{3.37}$$

By following standard procedure, the dispersion relations of the linearized hydrodynamic equations are then found by determining minus i times the complex eigenvalues associated with the matrix $M_{ab}^{N_f=1}$ in Eq. (3.36).

Before studying the collective modes that emerge when explicitly accounting for the dissipative contribution of sphaleron transitions, we first address the dynamics of vector and axial charges in the absence of sphaleron transitions by setting $\gamma_{\text{sph}} = 0$ in Eq. (3.36). The resulting dispersion relations of the charge modes take the form

$$\omega_{\mp} = -iD\mathbf{k}^2 \mp \frac{(eq_f)C}{\sqrt{\chi_A\chi_V}}|\mathbf{k}\cdot\mathbf{B}|, \tag{3.38}$$

which are the known dispersion relations associated with the CMW up to $\mathcal{O}(\mathbf{k}^2)$ [23]. We observe that the dispersion relations have two distinct, competing parts, namely a diffusive imaginary part and a propagating real part, as illustrated in Figure 3.1. Since the diffusion constant D is fixed, the mechanism dominating the behavior of the excitations depends primarily on the magnitude and orientation of the wavevector **k** of the perturbation and on the strength of the magnetic field. In the presence of a weak magnetic field, the dynamics of charge modes will be governed by diffusion. As the

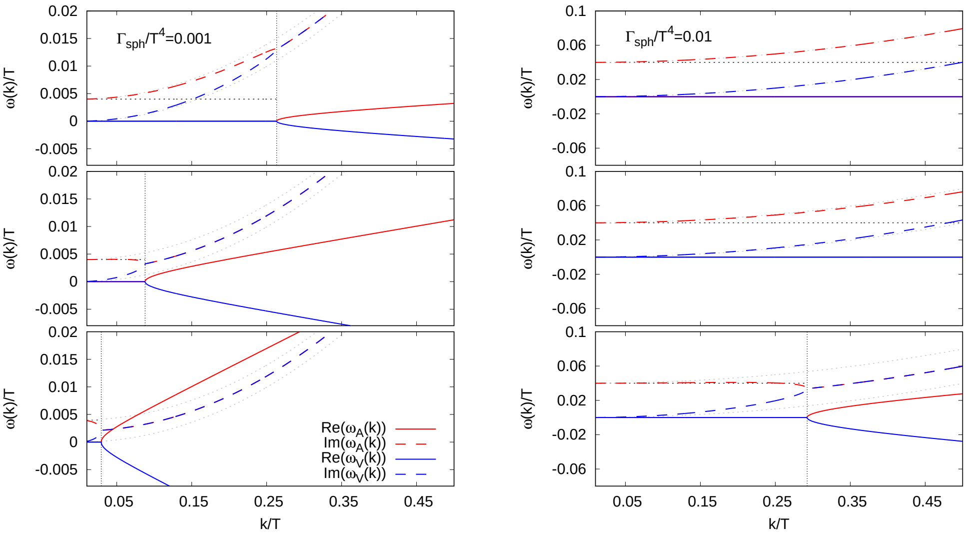

FIGURE 3.2: Single-flavor dispersion relations ω_A (3.43) and ω_V (3.44) for different values of Γ_{sph} plotted for $eB/T^2 = 0.05, 0.15, 0.45$ (top to bottom) respectively. Vertical dotted line represents k_{CMW} for each case.

magnetic field increases in strength, the low **k** modes oriented along the magnetic field will propagate with decreasing influence from diffusion.

We can further characterize the modes by discussing the associated eigenvectors,

$$\mathbf{v}_{\mp} = \begin{pmatrix} \cos\Omega_{\mp} \\ e^{i\phi_{\mp}} \sin\Omega_{\mp} \end{pmatrix}, \tag{3.39}$$

in which the subscripted sign corresponds to the sign of the real part of the dispersion relations. The mixing angles $\Omega_{\mp}$ are

$$\tan\Omega_{\mp} = \sqrt{\frac{\chi_V}{\chi_A}}, \tag{3.40}$$

and the phases $\phi_{\mp}$ are

$$e^{i\phi_-} = -1, \qquad e^{i\phi_+} = 1, \tag{3.41}$$

such that for equal vector/axial charge susceptibilities $\chi_V \approx \chi_A$, vector and axial evolution is maximally mixed.

When sphaleron transitions occur ($\gamma_{\mathrm{sph}} \neq 0$), the dispersion relations can no longer be simply divided into a diffusive and a propagating part. Instead, the inclusion of sphaleron

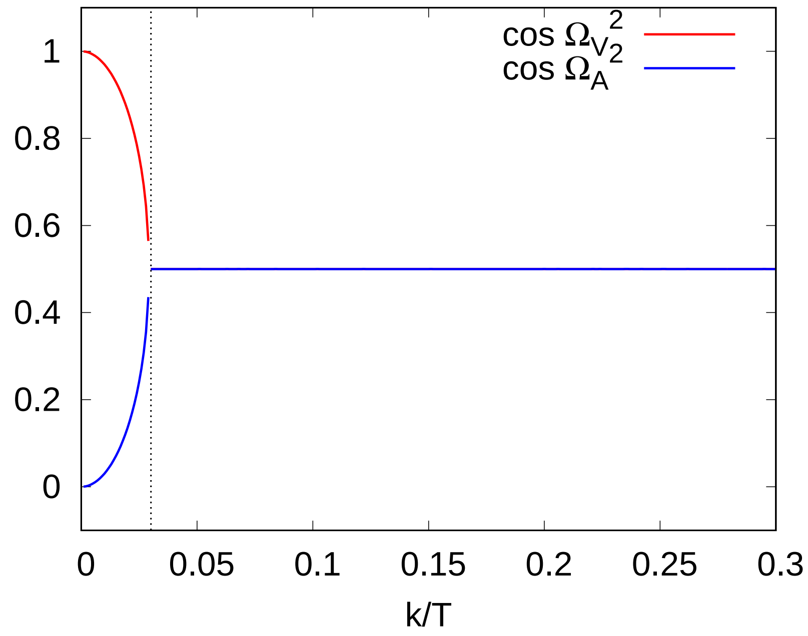

FIGURE 3.3: Mixing angle $\cos\Omega^2_{A/V}$ for the single-flavor case plotted for $eB/T^2 = 0.45$, $\Gamma_{\rm sph}/T^4 = 0.001$. Vertical dotted line represents $k_{\rm CMW}$.

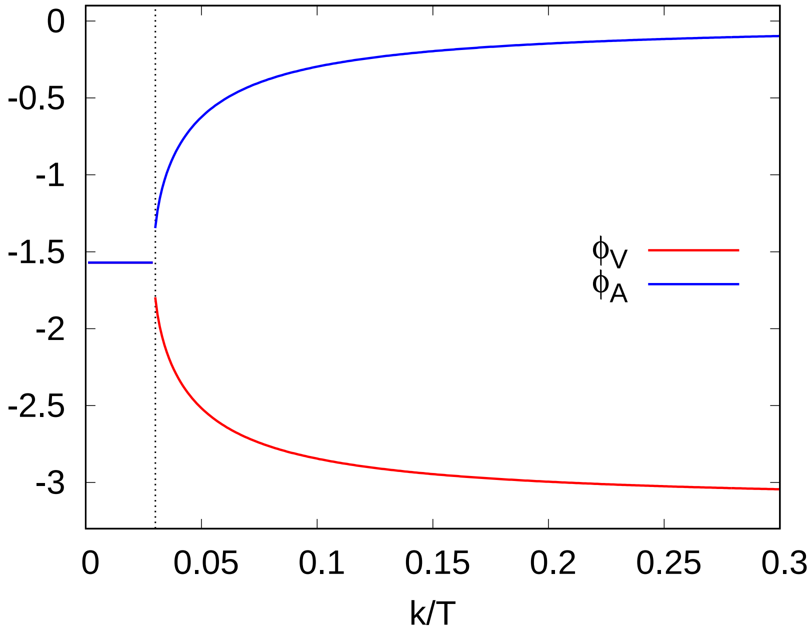

FIGURE 3.4: Phases for the single-flavor case plotted for $eB/T^2 = 0.45$, $\Gamma_{\rm sph}/T^4 = 0.001$. Vertical dotted line represents $k_{\rm CMW}$.

transitions associated with the term $\gamma_{\rm sph}$ leads to the emergence of a wavenumber threshold,

$$k_{\rm CMW} = \sqrt{\frac{\chi_V}{\chi_A}\frac{2\Gamma_{\rm sph}}{e|q_f|C|\mathbf{B}|}}, \tag{3.42}$$

which provides the minimum wavenumber above which a propagating chiral magnetic wave (CMW) can form for a given magnetic field strength. Hence it is convenient to express the dispersion relations in terms of the characteristic scale $k_{\rm CMW}$ as

$$\omega_A = -\frac{i}{2}\left(\gamma_{\rm sph} + 2D\mathbf{k}^2\right) - \frac{\gamma_{\rm sph}}{2}\sqrt{\left(\frac{k}{k_{\rm CMW}}\right)^2 - 1}, \tag{3.43}$$

$$\omega_V = -\frac{i}{2}\left(\gamma_{\rm sph} + 2D\mathbf{k}^2\right) + \frac{\gamma_{\rm sph}}{2}\sqrt{\left(\frac{k}{k_{\rm CMW}}\right)^2 - 1}, \tag{3.44}$$

where ω_A is the dispersion relation of the mode dominated by axial charge diffusion and ω_V is the dispersion relation of the mode dominated by vector charge diffusion.

We plot the dispersion relations in Figure 3.2 for three different values of the magnetic field strength $eB/T^2 = 0.05, 0.15, 0.45$ and further illustrate the behavior for two different values of the sphaleron transition rate, namely $\Gamma_{\rm sph}/T^4 = 0.001$, corresponding to perturbative estimates [16], and $\Gamma_{\rm sph}/T^4 = 0.01$, which is on the order of recent (quneched) lattice QCD results [53]. For illustrative purposes, we consider $N_c = 3$ with the charge susceptibilities of the free theory, given by

$$\chi_{A/V}(T, \mu_{A/V} = 0) = N_c\frac{T^2}{3} = T^2, \tag{3.45}$$

in a charge-neutral plasma.

Each plot shows two distinct regimes separated by their respective value of $k_{\rm CMW}$. Below $k_{\rm CMW}$, CMWs cannot form and modes are purely dissipative as the dynamics is dominated by damping due to sphaleron transitions. On the other hand, above $k_{\rm CMW}$, the dynamics of the modes depends on the magnetic field strength. As eB/T^2 decreases, the wavenumber threshold for the formation of a CMW increases and dissipative effects increasingly dominate the propagation due to charge mixing in the presence of the magnetic field. At high $k_{\rm CMW}$, modes will form a CMW but is strongly damped due to the combined effects of sphaleron damping and charge diffusion. Only at sufficiently high eB/T^2 can the CMW overcome the effects of sphaleron damping and propagate without significant dissipation, as seen in the lower left panel of Figure 3.2 for a small sphaleron transiton rate and large magnetic field strength. In the case of a large sphaleron rate, shown in the right panel of Figure 3.2 dissipative effects dominate for all magnetic field strength considered. Even for the larger magnetic field strength shown in the bottom

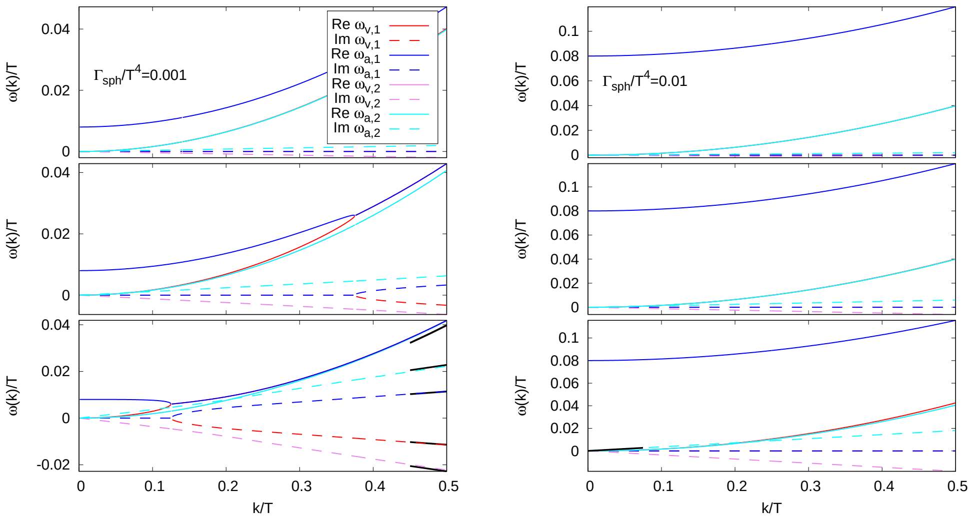

FIGURE 3.5: Dispersion relations in the multiflavor case for different values of $\Gamma_{\rm sph}$ plotted for $eB/T^2 = 0.05, 0.15, 0.45$ (top to bottom), respectively. Black solid lines indicate the asymptotic limits of small or large wavenumber k.

right panel, the dominant effect of the vector/axial charge mixing is not the formation of a propagating CMW but rather the additional dissipative effects due to sphaleron transitions.

We then investigate the extent of charge mixing by analyzing the corresponding eigenvectors,

$$\mathbf{v}_i = \begin{pmatrix} \cos\Omega_i \\ \\ e^{i\phi_i}\sin\Omega_i \end{pmatrix}. \tag{3.46}$$

for $i = A, V$. The mixing angles $\Omega_{A/V}$, shown in Figure 3.3, characterize the mixing of vector and axial charged for the two modes. While at $k = 0$ vector and axial charge dynamics is decoupled, a significant charge mixing already builds up in the dissipative regime $k < k_{\rm CMW}$ regime, before for $k > k_{\rm CMW}$, the mixing angle is identical for both modes, and the evolution of vector and axial charges is maximally mixed.

The phases $\phi_{A/V}$ are shown in Figure 3.4. In the regime where $k < k_{\rm CMW}$, the phases are the same, $\phi_{V/A} = -\pi/2$. However, for $k > k_{\rm CMW}$, as k increases, the phases diverge towards a phase difference $\Delta\phi = \pi$. That is, ϕ_A approaches 0, whereas ϕ_V approaches $-\pi$.

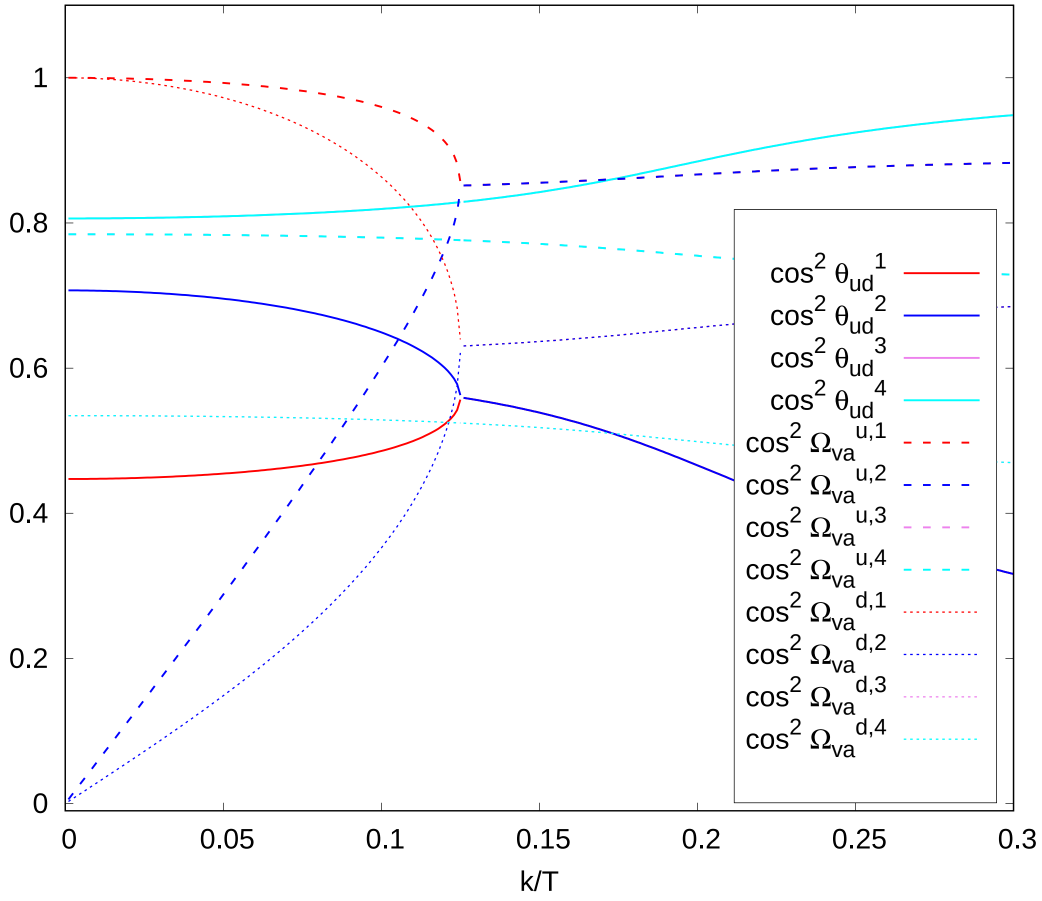

FIGURE 3.6: Mixing angles for two-flavor system, $eB/T^2 = 0.45$.

3.3.2 Multi flavor dynamics

We now move on and consider a two fermion-flavor system with up and down quarks. In this case, the evolution matrix for vector and axial charge dynamics of up and down quarks is given by

$$M_{ab}^{N_f=2} = \begin{pmatrix} M_{ab}^{N_f=1}\big|_{q_f=q_u} & \begin{matrix} 0 & 0 \\ 0 & \gamma_{\rm sph} \end{matrix} \\ \begin{matrix} 0 & 0 \\ 0 & \gamma_{\rm sph} \end{matrix} & M_{ab}^{N_f=1}\big|_{q_f=q_d} \end{pmatrix}, \tag{3.47}$$

where $M_{ab}^{N_f=1}$ denotes the single-flavor matrix given in (3.36), evaluated for the electric charge of the up quark and down quark, respectively. The dynamics is then governed by Eq. (3.37) for $\phi_a = \{\delta n_{V,u}, \delta n_{A,u}, \delta n_{V,d}, \delta n_{A,d}\}$, the vector and axial charge densities for up and down quarks. We emphasize that the dissipative term due to sphaleron

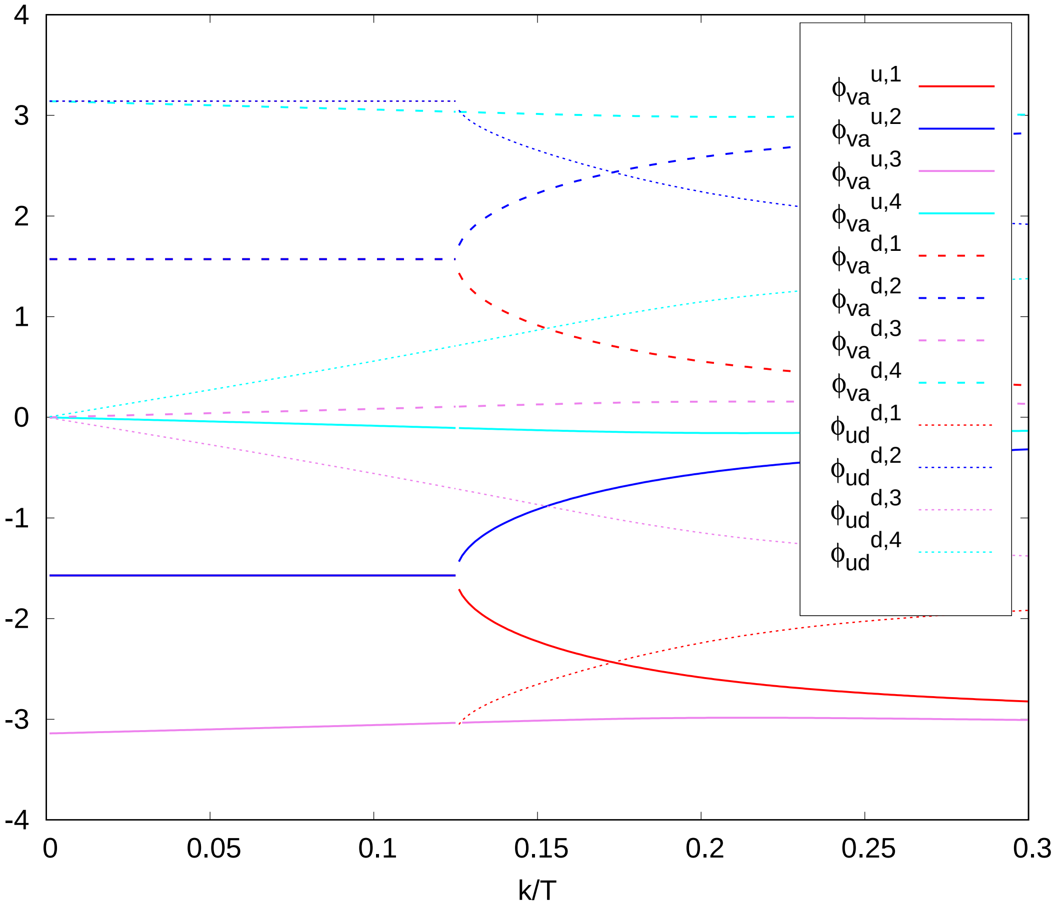

FIGURE 3.7: Phases for two-flavor system, $eB/T^2 = 0.45$.

transitions couples the dynamics of the up and down quarks, as can already be seen in Eq. (3.35), where the right hand side is proportional to the net axial charge imbalance of all flavors.

The dispersion relations in the two flavor case are shown in Figure 3.5 for both a low and higher sphaleron rate, for three different values of the magnetic field. As in the single-flavor case, we can express the eigenvectors in terms of mixing angles and phases. We parameterize the four eigenvectors via

$$\mathbf{v}_i = \begin{pmatrix} \cos\theta_{ud}\cos\Omega^u_{VA} \\ e^{i\varphi^u_{VA}}\cos\theta_{ud}\sin\Omega^u_{VA} \\ e^{i\varphi_{ud}}\sin\theta_{ud}\cos\Omega^d_{VA} \\ e^{i\varphi_{ud}}e^{i\varphi^d_{VA}}\sin\theta_{ud}\sin\Omega^d_{VA} \end{pmatrix}, \quad i = \{1,2,3,4\}\,. \tag{3.48}$$

Based on this parameterization, we find the mixing angles shown in Figure 3.6 and the phases shown in Figure 3.7, where the mixing angle $\cos\theta_{ud}$ describes mixing between up and down flavors, while $\cos\Omega^{u,d}_{VA}$ describe axial and vector charge mixing. Since the general structure in Figure 3.5, Figure 3.6, and Figure 3.7 is rather complicated, we discuss the analytic forms of the vector/axial charge modes and dispersion relations in the two-flavor system in the limiting cases of small and large wavenumber.

In the large wavenumber limit, the sphaleron rate becomes increasingly less important, such that the asymptotic case is described when we take $\gamma_{\text{sph}} \to 0$ in $M_{ab}^{N_f=2}$. In this case, there is no mixing between up and down flavors, such that the corresponding eigenvalues take the form

$$\omega_{d\mp} = -iD\mathbf{k}^2 \mp \frac{e|q_d|C}{\sqrt{\chi_A\chi_V}}|\mathbf{k}\cdot\mathbf{B}|, \tag{3.49}$$

$$\omega_{u\mp} = -iD\mathbf{k}^2 \mp \frac{e|q_u|C}{\sqrt{\chi_A\chi_V}}|\mathbf{k}\cdot\mathbf{B}|, \tag{3.50}$$

which is identical to Eq. (3.38) and describes the independent dynamics of up and down quarks. Conversely, in the small wavenumber limit ($k \to 0$) sphaleron damping plays a prominent role. In this limit, the leading eigenvalues are

$$\omega_1 = -2i\gamma_{\text{sph}}, \quad \omega_2 = \omega_3 = \omega_4 = 0\ , \tag{3.51}$$

where the first mode corresponds to the relaxation of the net axial charge density $(\delta n^u_A + \delta n^d_A)$ due to sphaleron transitions, while the axial charge difference between up and down quarks $(\delta n^u_A - \delta n^d_A)$ is conserved, as well as the corresponding vector quantities, $(\delta n^u_V + \delta n^d_V)$ and $(\delta n^u_V - \delta n^d_V)$. One can further disentangle the three degenerate eigenvalues by applying degenerate perturbation theory to next-to-leading order. By assuming $\chi_a = \chi_V = \chi$ for simplicty, and leaving details of the calculation for Appendix C, the eigenvalues to first order in perturbation theory are given by

$$\omega_2 = 0, \quad \omega_{3,4} = \mp\frac{eC}{\chi\sqrt{2}}\sqrt{(q_d^2 + q_u^2)}|\mathbf{k}\cdot\mathbf{B}|. \tag{3.52}$$

indicating the emergence of constant mode and conjugate pair of propagating chiral magnetic waves, which is indicated by a black line in the bottom right panel of Figure 3.6.

Generally beyond these two simple limits, the coupled dynamics is rather complicated, as can be inferred from the rather complex structures seen in Figure 3.5, Figure 3.6, and Figure 3.7. Clearly, the reason for this is that, in the multi-flavor case, even in the the small k limit, all of the modes are associated with linear combinations of u and d vector and axial charges, as can be deduced the analytic expressions for the eigenvectors in Appendix C as well as from the mixing angles and phases in Figure 3.6 and Figure 3.7.

3.4 Effects of sphaleron damping on vector and axial charge dynamics

Next, in order to assess the impact of sphaleron transitions on normal and anomalous transport phenomena in a QCD plasma, we investigate the response of the system to an initial charge inhomogeneity by solving the linearized hydrodynamic equations (3.37) numerically. We orient the magnetic field along the y-direction and study perturbations in the $x - y$ plane to loosely mimic the evolution in the transverse plane in an off-central heavy-ion collision.[2] We set the scale by setting temperature $T = 4T_C$, where $T_C = 155$ MeV is the QCD cross-over temperature and study the evolution over a time scale $t = 10$ fm/c. We limit ourselves to the single-flavor scenario ($N_f = 1$) and consider two magnetic field strength regimes: $eB/T^2 = 1/16$ and $eB/T^2 = 1$. The first of these regimes, where $eB/T^2 = 1/16$, was chosen to correspond to m_π^2, an optimistic estimate for the magnetic field strength achieved in a heavy ion collision [109]. The second, $eB/T^2 = 1$, was chosen arbitrarily such that it was much stronger than m_π^2. We consider four different values of the sphaleron rate Γ_{sph} for each magnetic field strength eB/T^2, and monitor the evolution of the vector/axial charge distributions along the magnetic field direction, i.e. $n_{V/A}(y,t) = \int_{x,z} n_{V/A}(x,y,z,t)$, to probe how sphaleron transitions affect vector and axial charge transport.

3.4.1 Vector charge perturbations

We first consider an initial vector charge perturbation, given by a Gaussian distribution of width $\sigma = 0.4R_p$, $R_p = 1$ fm, such that the width is on the order of the size of a nucleon – the characteristic length scale of variations in the transverse plane of a heavy-ion collision. By studying the vector and axial charge profiles after $t = 10$ fm/c of evolution as depicted in Figure 3.8, we observe that vector charge diffuses while axial charge separates along the direction of the magnetic field. At $eB/T^2 = 1/16$, the vector charge diffuses with no discernible difference with respect to the value of the sphaleron transition rate. However, when the magnetic field strength is increased to $eB/T^2 = 1$, the charge either purely diffuses or forms a highly diffusive wave. This behavior depends on the sphaleron transition rate. In fact, there is a clear transition in behavior between the charge distribution for $\Gamma_{\text{sph}}/T^4 = 10^{-3}$ and $\Gamma_{\text{sph}}/T^4 = 10^{-2}$; as the sphaleron rate increases, the behavior of the vector charge changes from diffusive propagation to purely diffusive. On the other hand, axial charge separates in the same manner for both magnetic field strengths, though the magnitude of charge separation is greater

---

[2] When solving Eq. (3.37) numerically, in practice we discretize the evolution on a two-dimensional spatial lattice (256^2). The lattice is scaled such that the length of the sides were 10 fm with spacing $a_S = 10/256$ fm.

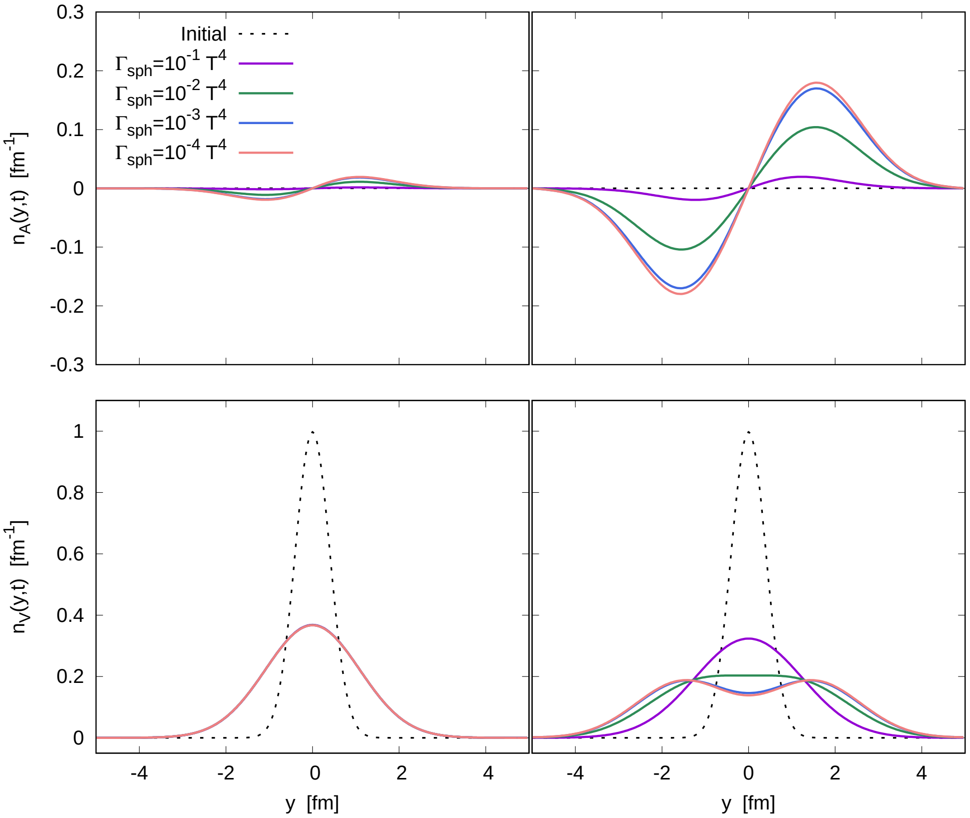

FIGURE 3.8: Spatial profiles of axial (n_A) and vector (n_V) charge distributions for *initial vector charge perturbation* after an evolution for $t = 10$ fm/c. Different curves in each panel correspond to four different values of the sphaleron transition rate Γ_{sph}. Different columns show the the results for different magnetic field strength $eB/T^2 = 1/16$ in the left column and $eB/T^2 = 1$ in the right column.

for a strong magnetic field. One sees immediately from Figure 3.8 that the magnitude and distance of charge separation depend on the value of the sphaleron transition rate. Hence, as the rate of sphaleron transitions increases, the magnitude and distance of separation decreases.

3.4.2 Axial charge perturbations

Next we consider an initial perturbation of the axial charge density, which can be seen as a simple toy model for dynamics of the Chiral Magnetic Effect (CME) in heavy ion collisions [21]. We employ the same parameters as for the initial vector charge perturbation, and present our results for the vector and axial charge profiles in Figure 3.9. As can be expected, the response to an initial axial charge perturbation is significantly more sensitive to the sphaleron rate. Specifically, for $eB/T^2 = 1/16$ shown in the left column, the axial charge profile diffuses and decays and the decay rate depends on the sphaleron rate. For $eB/T^2 = 1$, the modes for each of the four sphaleron rates form a

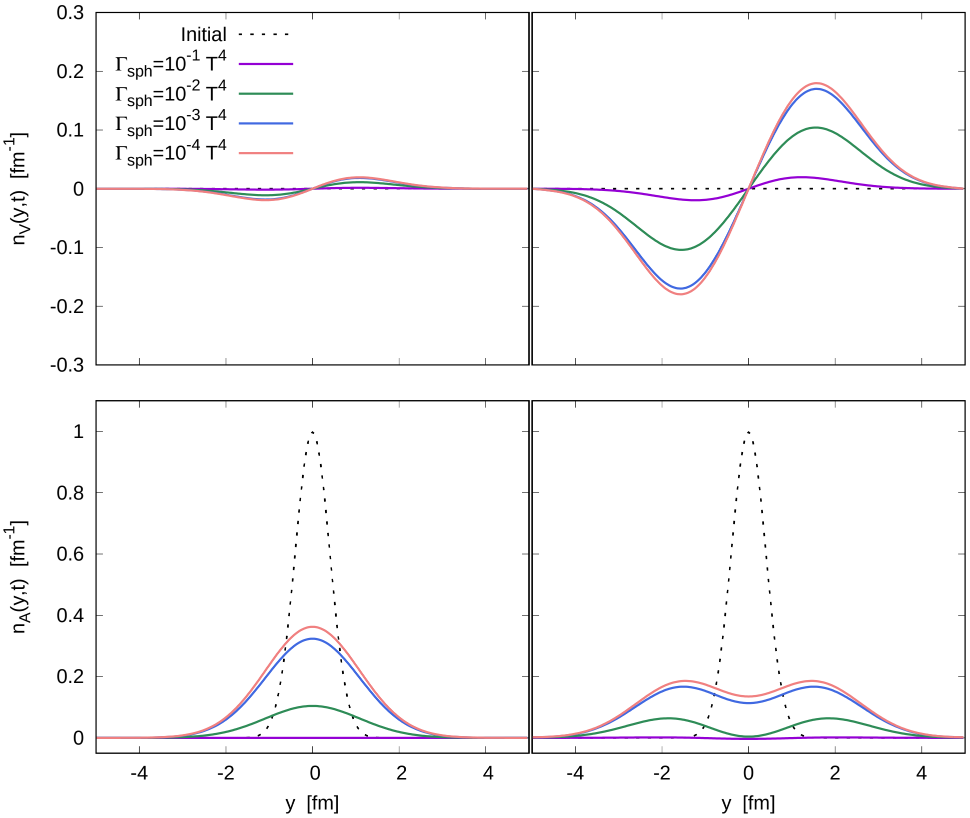

FIGURE 3.9: Spatial profiles of axial (n_A) and vector (n_V) charge distributions for *initial axial charge perturbation* after an evolution for $t = 10$ fm/c. Different curves in each panel correspond to four different values of the sphaleron transition rate Γ_{sph}. Different columns show the the results for different magnetic field strength $eB/T^2 = 1/16$ in the left column and $eB/T^2 = 1$ in the right column.

decaying and highly diffusive wave. With regards to vector charge for the initial axial distribution, one clearly observes a separation of vector charges along the direction of the magnetic field, albeit the amount of charge separation strongly depends on the sphaleron rate and the magnetic field strength.

We also find that for the weaker field case, $eB/T^2 = 1/16$ where the magnetic field strength is relevant for heavy ion collisions, the axial charge charge only diffuses and there is no clear sign of propagating waves. Even though a small amount of vector charge separation is still generated also in this case, it is clear that dissipative effects dominate in this case, and clearly need to be taken into account in a realistic description of the dynamics of the CME and the CMW in heavy-ion collisions.

3.4.3 Sensitivity of charge separation to the sphaleron rate

As discussed in Chapter 2, the vector charge separation along the direction of the magnetic field has been suggested as an experimental signature of the CME in heavy-ion

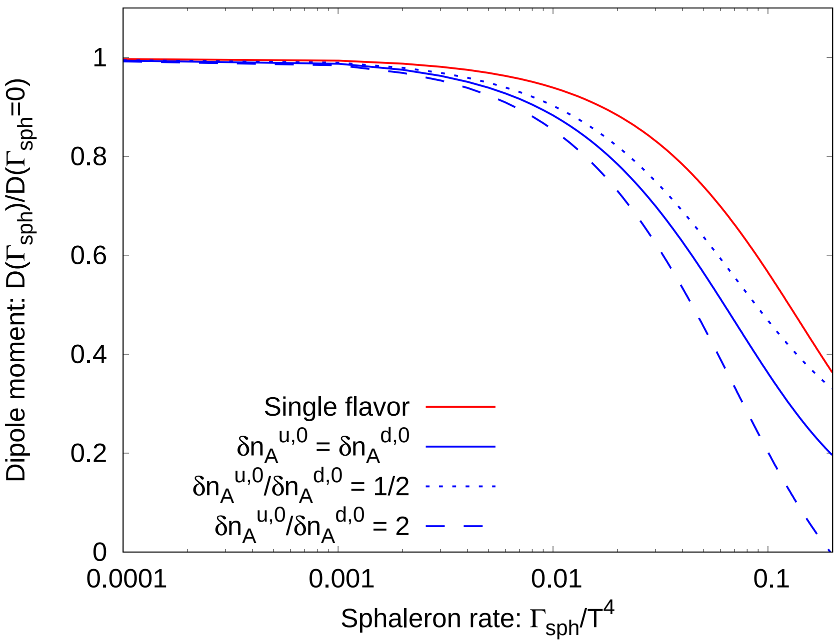

FIGURE 3.10: Electric charge separation, quantified by the electric dipole moment D for an initial axial charge distribution as a function of Γ_{sph} for single- and two-flavor configurations of various initial charge ratios at $t = 10$ fm/c.

collisions [72]. Since this charge separation is sensitive to the sphaleron transition rate, we will further quantify this dependence by using the dipole moment. Specifically, we consider vector charge separation as the result of an initial axial charge perturbation, and determine the electric dipole moment

$$D(\mathbf{B}, t) = \int d^3x \, \frac{\mathbf{x} \cdot \mathbf{B}}{|\mathbf{B}|} \sum_f e q_f n_{V,f}(t, \mathbf{x}), \tag{3.53}$$

which quantifies the amount of electric charge separation along the direction of the magnetic field.

We first derive an expression for the dipole moment for the case of a single quark flavor ($N_f = 1$), rewriting Eq. (3.53) as

$$\begin{aligned} D(\mathbf{B}, t) = \int d^3x \, \frac{\mathbf{x} \cdot \mathbf{B}}{|\mathbf{B}|} \int \frac{d^3k}{(2\pi)^3} e^{i\mathbf{k}\cdot\mathbf{x}} \begin{pmatrix} 1 \\ 0 \end{pmatrix}^t \\ \times \exp\left\{M_{ab}(\mathbf{k})(t - t_0)\right\} \begin{pmatrix} \tilde{n}_V(t_0, \mathbf{k}) \\ \tilde{n}_A(t_0, \mathbf{k}) \end{pmatrix}, \end{aligned} \tag{3.54}$$

where we have used the notation $\tilde{n}_{V/A}(\mathbf{k})$ to differentiate between the charge distributions in coordinate space and their Fourier-transformed counterparts. Recall, matrix M_{ab} is defined by Eq. (3.36). Then, switching the order of integration,

$$D(\mathbf{B},t) = \int \frac{d^3k}{(2\pi)^3} \int d^3x \frac{\left(-i\partial^j_{\mathbf{k}} e^{i\mathbf{k}\cdot\mathbf{x}}\right) B_j}{|\mathbf{B}|} \begin{pmatrix} 1 \\ 0 \end{pmatrix}^t \times \exp\left\{M_{ab}(\mathbf{k})(t-t_0)\right\} \begin{pmatrix} \tilde{n}_V(t_0,\mathbf{k}) \\ \tilde{n}_A(t_0,\mathbf{k}) \end{pmatrix}, \tag{3.55}$$

which becomes

$$\begin{aligned} D(\mathbf{B},t) &= \left(\int \frac{d^3k}{(2\pi)^3} \int d^3x e^{i\mathbf{k}\cdot\mathbf{x}}\right) \frac{i\partial^j_{\mathbf{k}} B_j}{|\mathbf{B}|} \begin{pmatrix} 1 \\ 0 \end{pmatrix}^t \\ &\quad \times \exp\left\{M_{ab}(\mathbf{k})(t-t_0)\right\} \begin{pmatrix} \tilde{n}_V(t_0,\mathbf{k}) \\ \tilde{n}_A(t_0,\mathbf{k}) \end{pmatrix} \\ &= \frac{i\partial^j_{\mathbf{k}} B_j}{|\mathbf{B}|} \begin{pmatrix} 1 \\ 0 \end{pmatrix}^t \exp\left\{M_{ab}(\mathbf{k})(t-t_0)\right\} \\ &\quad \times \begin{pmatrix} \tilde{n}_V(t_0,\mathbf{k}) \\ \tilde{n}_A(t_0,\mathbf{k}) \end{pmatrix} \Bigg|_{k=0}. \end{aligned} \tag{3.56}$$

Evaluating Eq. (3.56) for an initial axial charge perturbation and one quark flavor ($N_f = 1$), we find the dipole moment

$$D(\mathbf{B},t) = -\frac{eq_f|\mathbf{B}|CT}{4\Gamma_{\mathrm{sph}}} \left(1 - e^{-4\Gamma_{\mathrm{sph}}t/(\chi_A T)}\right) \delta\tilde{n}^0_A, \tag{3.57}$$

where we use $\delta\tilde{n}^0_A = \delta\tilde{n}_A(t=0,\mathbf{k}=0)$ to denote the initial net axial charge imbalance.

Similarly, in the case of two quark flavors ($N_f = 2$), we find

$$\begin{aligned} D(\mathbf{B},t) = &- \frac{e|\mathbf{B}|C(q_u^2+q_d^2)T}{16\Gamma_{\mathrm{sph}}} \left(1 - e^{-\frac{8\Gamma_{\mathrm{sph}}t}{\chi_A T}}\right)(\delta\tilde{n}^{u,0}_A + \delta\tilde{n}^{d,0}_A) \\ &- \frac{e|\mathbf{B}|C(q_u^2-q_d^2)T}{2\Gamma_{\mathrm{sph}}} \left(\frac{\Gamma_{\mathrm{sph}}t}{\chi_A T} e^{-\frac{8\Gamma_{\mathrm{sph}}t}{\chi_A T}}\right)(\delta\tilde{n}^{u,0}_A - \delta\tilde{n}^{d,0}_A), \end{aligned} \tag{3.58}$$

where as before $\delta\tilde{n}_A^{u/d,0} = \delta\tilde{n}_A^{u/d}(t=0,\mathbf{k}=0)$ denote the initial axial charge imbalance of u and d flavors, such that the terms in the second line describe the response to a net axial charge imbalance of both flavors, whereas the terms in the third line describe the response to an axial charge difference between u and d flavors. However, most importantly, from Eqs. (3.57) and (3.58), we immediately see the relationship between the sphaleron transition rate $\Gamma_{\rm sph}$ and separation of charge, as quantified by the dipole moment $D(\mathbf{B},t)$.

We illustrate the relations for both the single-flavor and two-flavor case in Figure 3.10, where we present the dependence of the dipole moment $D(\mathbf{B},t)$ on the sphaleron transition rate $\Gamma_{\rm sph}$. By normalizing the dipole moment to its value for $\Gamma_{\rm sph} = 0$, the quantity $D(\Gamma_{\rm sph})/D(\Gamma_{\rm sph}=0)$ becomes independent of the magnetic field strength (c.f. Eqns. (3.57,3.58)) and can be viewed an overall suppression factor of the charge separation signal due to sphaleron transitions. When the sphaleron transition rate is large, all terms proportional to $e^{-\#\Gamma_{\rm sph}t/\chi_a T}$ in Eqns. (3.57,3.58) can be dropped and the charge separation is proportional to $1/\Gamma_{\rm sph}$. By inspecting the results in Figure 3.10 one finds that after an evolution for 10fm/c, the suppression for sphaleron rates $\Gamma_{\rm sph}/T^4 \lesssim 0.01$ is still rather modest. However, for values on the order of the (quenched) lattice QCD estimates [53] $\Gamma_{\rm sph}/T^4 \gtrsim 0.02$ there is in a significant suppression of the signal, as well as a strong sensitivity of the result to the actual value of the sphaleron transition rate. While such a suppression may make it harder to detect possible signatures of the CME and CMW in heavy-ion collisions, the strong sensitivity to the sphaleron rate also suggests a possible experimental avenue for constraining the sphaleron rate using charge separation measurements associated with chiral phenomena such as the CME and the CMW.

3.5 Conclusions & Outlook

Based on a general discussion of the criteria for the validity of a macroscopic description of the axial charge dynamics in high-temperature QCD plasmas, we modified the anomalous hydrodynamic equations of motion to explicitly include dissipative effects sourced by sphaleron transitions. Within this framework, dissipation due to sphaleron transitions is incorporated as a damping term proportional to the sphaleron transition rate, which depletes the net axial charge imbalance of all fermion flavors and contributes positively to entropy production in the system. Notably, in the case of multiple fermion flavors, the dissipative contribution from sphaleron damping also coupled the dynamics of different flavors, as the dissipative term is proportional to the sum of the axial charge density of all flavors.

By linearizing the hydrodynamic equations around a space-time independent background, we investigated the coupled dynamics of vector and axial charge perturbations in a charge neutral background and contrasted our results including sphaleron damping to the traditional behavior of a Chiral Magnetic Wave. When sphaleron damping is taken into consideration, a characteristic wavenumber scale k_{CMW} emerges. Below k_{CMW}, charge modes experience decaying diffusive behavior as the dynamics is dominated by sphaleron transitions. Conversely, above k_{CMW}, the modes behave like an ordinary CMW, albeit the latter is typically strongly damped. The threshold $k_{\text{CMW}} \sim \Gamma_{\text{sph}}/eB$ depends on the sphaleron transition rate and magnetic field strength and we expect that for typical values achieved in heavy-ion collisions at RHIC and LHC energies dissipative effects dominate and the decaying diffusive behavior is realized.

By studying the time evolution of linearized vector/axial charge perturbations, we visualized the impact of the sphaleron transition rate on vector and axial charge transport in a QCD plasma in the presence of a magnetic field. Strikingly, for sufficiently strong magnetic fields, the sphaleron transition rate also has an impact on vector charge transport, i.e. the vector charge response to a vector charge perturbation, which may be interesting from the point of view of extracting the QCD sphaleron rate on the lattice. Secondly, in the presence of an axial charge imbalance, we observe the expected separation of vector charges along the direction of the magnetic field. Even though the amount of charge separation strongly depends on the sphaleron rate and magnetic field strength, the general phenomenon of charge separation persists. We further quantified the amount of charge separation in terms of the electric dipole moment, and determined its dependence on the sphaleron rate. We find that for realistic values of the sphaleron transition rate, the charge separation can easily be suppressed by a factor of two compared to the situation where dissipative effects due to sphaleron transitions are not taken into account.

Since the charge separation is highly sensitive to the sphaleron transition rate, it is conceivable that experimental measurements of charge separation can be used to constrain the QCD sphaleron rate. Such constraints would not only be useful to confront current state-of-the-art calculations, but would provide a unique measurements that can elucidate topological properties of QCD. Our results thus motivate the development of a more comprehensive treatment of axial charge dynamics, where it would also be important to extend the present framework to include fluctuations of axial charge sourced by sphaleron transitions.

Chapter 4

Gauge-invariant condensation

The matter formed moments after a heavy ion collision is far from equilibrium and is characterized by a large initial density of gluons, which could facilitate the formation of a condensate [34]. However, several complications arise when putting together a description of such a condensate. Classical-statistical and kinetic theory simulations have shown that the plasma evolution does not support the formation of a Bose condensate of gluon fields [87, 88, 90, 110]. QCD is also a non-Abelian gauge theory; direct identification of condensation requires the construction of a *local* gauge-invariant operator that measures the macroscopic zero mode that signals gauge condensation. Previous examples of gauge-invariant operators for nonequilibrium condensation have been studied in the context of the Abelian Higgs model and its relation to non-Abelian theories [35–37].

It has been demonstrated in [5] that the initial overoccupation of gluons does in fact lead to the formation of a gauge-invariant condensate. Condensation is indicated by the formation of a macroscopic zero-mode expectation value that scales proportionally with $(2\pi)^d\delta^{(d)}(0) \to L^d$ for a $d-$dimensional finite volume with the length scale L [38]. Specifically, the study investigated the expectation value of the spatial Wilson loop, which computes the infrared excitations of non-Abelian gauge theories as previously explained in Chapter 2 [2, 39–41]. A volume-independent condensate fraction was established for increasing $L \to \infty$. It was further demonstrated that condensate formation is a far-from-equilibrium phenomenon, since the zero mode fraction does not grow in time or scale with volume in classical thermal equilibrium. However, the Wilson loop is a non-local object. Therefore it cannot be used to formulate a low energy effective theory with which we can further unravel the dynamics of the infrared condensate.

In this chapter, we introduce two local order parameters that are related to the spatial Wilson loop: the first one is the two-point connected correlation function of the traced spatial Polyakov loop. The second one is based on an algebra-valued scalar field that is the holonomous eigenvalue of the Polyakov loop. These fields are gauge invariant and live in a $2+1$ dimensional space-time. We will demonstrate that they are sufficiently local objects and their correlators capture the same condensation phenomena as the spatial Wilson loop.

By utilizing classical-statistical lattice simulations, we investigate the dynamics of a weakly-coupled Yang-Mills plasma with a large gluon density. The simulated system approaches a self-similar regime with universal scaling properties, which has been studied in detail [3, 41, 90] and shows similarities to scalar systems [111, 112].

We extract the condensation observable in the vicinity of this self-similar state and analyze its evolution over time. Through this investigation, we aim to shed light on the nature of gauge condensates, the implications of their presence with respect to hydrodynamics and transport phenomena, and their potential role in the formulation of a low-energy effective field theory for QCD. By studying local correlation functions of an algebra-valued scalar field, we can compare our results with far-from-equilibrium Bose condensation for a scalar order parameter field [4, 38, 113–116].

This chapter is based on Ref. [117] and is organized as follows. In Section 4.1 we first discuss the early-time infrared dynamics in the far-from-equilibrium QGP and then introduce the local order parameters used to identify condensation. Then, in Section 4.2 we discuss the employed classical-statistical lattice simulations and present results that demonstrate condensate formation. We finally conclude in Section 4.3.

4.1 Early-time infrared dynamics far from equilibrium

In Ref. [5] it has been shown that the early time evolution of QCD exhibits a condensate. The respective signatures have been obtained from the scaling dynamics of sufficiently large spatial Wilson loops. While this analysis demonstrates the presence of gauge condensates, their nature and dynamics remain to be elucidated.

The presence of a condensate is consequential for the formulation of non-Abelian gauge theories. In particular, it is important to consider when describing the early-time dynamics of QGP in terms of an effective kinetic theory. In this section, we discuss a corresponding reparameterization of the Yang-Mills action,

$$\begin{aligned} S_{\mathrm{YM}}[A] &= -\frac{1}{2}\int_x \mathrm{tr}\, F_{\mu\nu}F^{\mu\nu}\,, \\ F_{\mu\nu} &= \partial_\mu A_\nu - \partial_\nu A_\mu - \mathrm{i}g[A_\mu, A_\nu]\,, \end{aligned} \tag{4.1}$$

with the trace in the fundamental representation. We can formulate the theory in a finite, manifestly infrared setup with periodic boundary conditions on a torus T^3,

$$\int_x = \int \mathrm{d}t \int_{T^3} \mathrm{d}^3x, \qquad T^3 = \mathbb{R}^3 \bmod L\,. \tag{4.2}$$

This configuration reflects the situation in a heavy ion collision with a rapidly expanding but finite plasma. It also allows for a gauge invariant regularization and control of infrared divergences. Finally, we employ simulations to compute the far-from-equilibrium dynamics of gauge theories that are formulated on a finite spatial lattice with periodic boundary conditions.

Due to the presence of gauge condensation, it is advantageous to rewrite the Yang-Mills action (4.1) partially in terms of gauge invariant degrees of freedom that may directly carry the condensation phenomenon. The expectation value of spatial rectangular Wilson loops,

$$W[t, \Delta x, L] = \frac{1}{N_c}\,\mathrm{Tr}\,\mathcal{P}e^{-i\,g\int_{\mathcal{C}} A_i(t,\boldsymbol{x})\,dx_i}\,, \tag{4.3}$$

serves as a gauge-invariant order parameter for gauge condensation [5], where $\mathcal{P}$ denotes path ordering and $\mathcal{C}$ is the closed rectangular path. In (4.3), the Wilson loop stretches over the whole x_2-direction of length L and has an extent $\Delta x = x_1 - x_1'$ in x_1 direction, as depicted in the left panel of Figure 4.1. Therefore, it is a non-local observable instead of a correlation function of local dynamical degrees of freedom. In Section 4.1.2 we will construct local observables in the x_1 direction that are derived from the Polyakov loop, whose correlator is depicted in the right panel of Figure 4.1.

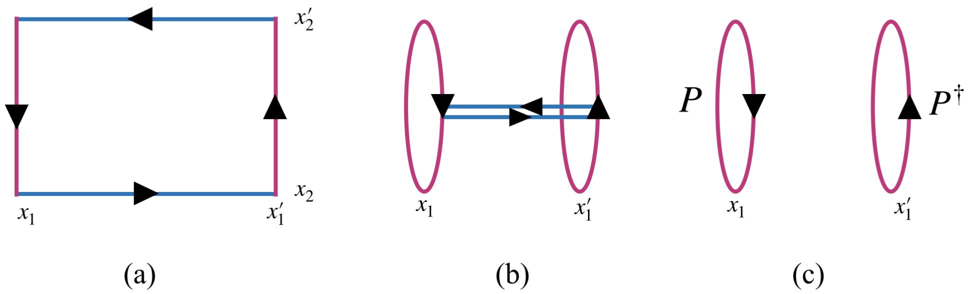

FIGURE 4.1: Visualization of the spatial correlation between the Polyakov loop correlator $\langle PP^\dagger\rangle(t, \Delta x, L)$ in a) and the rectangular spatial Wilson loop $W[t, \Delta x, L]$ in c). The spatial periodicity of the system results in the identification of coordinates $x_2' \equiv x_2$ mod L on the lattice, causing the Wilson loop to exhibit a wrapping effect in the x_2 direction, as depicted in b). The distinguishing feature between the Polyakov loop correlator and the Wilson loop is the presence of connecting Wilson lines (blue) in the latter, which shows the connection between the two quantities.

4.1.1 The infrared scale far from equilibrium

As established in Chapter 2, far from equilibrium in a highly-occupied QCD plasma, there exists a separation of scales. The relevant scale for this chapter is the ultrasoft magnetic scale. The ultrasoft scale approaches zero faster than the Debye screening scale in time, and its scaling exponent sets the time scale for the build-up of a coherent macroscopic state–our condensate.

Below the magnetic scale, at ultrasoft momenta where the occupation numbers are expected to be $f \sim 1/\alpha_s$, the dynamics is non-perturbative. In this regime, the notion of gauge-fixed particle numbers based on a distribution f of gauge modes is ill-defined. Therefore, we cannot approach condensation by counting occupancies of quasi-particle states. Furthermore, far from equilibrium, a condensate can emerge without having a well-defined chemical potential entering its distribution [4, 38], in contrast to condensation in thermal equilibrium.

We employ a more general approach to condensation, as this phenomenon can be identified from properties of correlation functions in strongly correlated systems both in and out of equilibrium. The previous study [5] investigated the dynamics at long distances using gauge-invariant but non-local spatial Wilson loops. The extension of this study, in order to eventually formulate a kinetic theory describing this phenomenon, necessitates the investigation of more local order parameters.

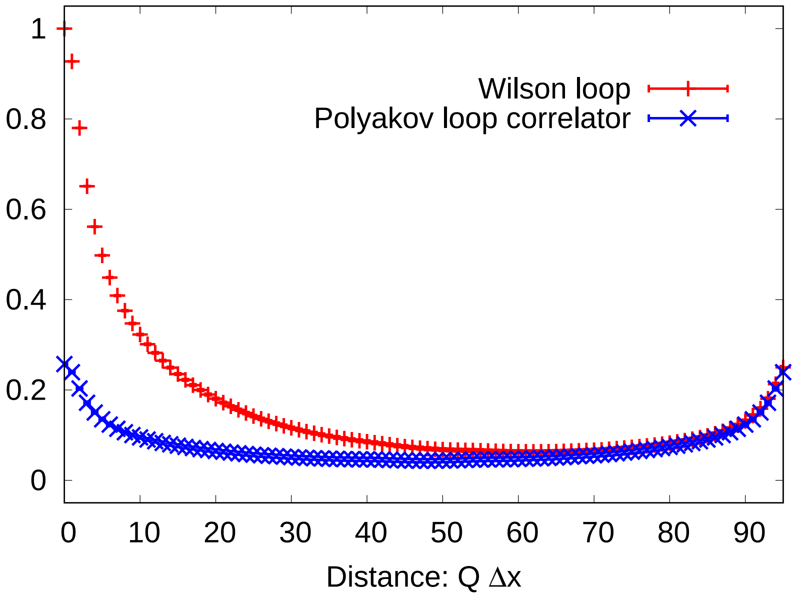

FIGURE 4.2: Comparison of the Wilson loop expectation value $\langle W \rangle$ and the Polyakov loop correlator $\langle PP^\dagger \rangle$ on a lattice with size $N_s = 96$ at time $Qt = 1000$. The Polyakov loop correlator $\langle PP^\dagger \rangle$ exhibits consistent dynamics with the Wilson loop at larger spatial separations, indicating a strong correlation between the two quantities.

4.1.2 Local order parameters

We seek for degrees of freedom that do not hide essential parts of the dynamics by absorbing them, as the Wilson loop (4.3) does, and are as local as possible. The latter is important for the construction of a local kinetic theory for QCD, specifically to rewrite the action in Eq. (4.1) in terms of these degrees of freedom.

This becomes clear when we view the Wilson loop as a correlation function instead of a dynamical field. Let us consider the Wilson loop in (4.3), shown in the left panel of Figure 4.1, that winds around the full extent of the x_2 direction. This observable gives us access to the infrared dynamics that we are interested in. From the simulation point of view, it also smooths out ultraviolet effects and hence lattice artifacts [1]. In this picture, the Wilson loop can be understood as the correlation function of an operator at x_1 and one at x_1'. However, further non-localities are introduced by the connecting lines, which are indicated by the blue lines in the middle panel of Figure 4.1.

---

[1] We note that in classical-statistical simulations of highly occupied systems far from equilibrium the dependence on the ultraviolet modes can be further reduced if the characteristic dynamical scale $\sim Q_s$ is much lower.

In order to construct a more local version of the Wilson loop that carries the correlation function structure, we introduce a spatial Wilson loop,

$$P_i(t,\boldsymbol{x}) = \frac{1}{N_c}\,\mathrm{Tr}\;\tilde{P}_i(t,\boldsymbol{x}) \tag{4.4}$$

$$\tilde{P}_i(t,\boldsymbol{x}) = \mathcal{P}e^{-i\,g\int_0^L A_i(t,\boldsymbol{x})\,dx_i}\,, \tag{4.5}$$

which corresponds to a closed path over the full x_i direction, as depicted in the right panel of Figure 4.1. It can be viewed as the spatial version of the Polyakov loop that usually corresponds to a temporal Wilson loop that is used in thermal QCD as an order parameter for the confinement-deconfinement phase transition. We therefore refer to it as the spatial Polyakov loop, or in short, the Polyakov loop, in a slight abuse of notation. Its two-point function with $\boldsymbol{x}, \boldsymbol{x}'$ differing by $\Delta x = x_1 - x_1'$

$$\langle P_2(t,\boldsymbol{x}) P_2^\dagger(t,\boldsymbol{x}')\rangle \tag{4.6}$$

is related to the expectation value of the Wilson loop (4.3), as suggested in Figure 4.1 but lacks the non-local connection lines between x_1 and x_1'. Therefore, in contrast to the Wilson loop in Eq. (4.3), the correlation function in Eq. (4.6) is symmetric under $\Delta x \to L - \Delta x$ due to spatial periodicity. This can be seen quantitatively in Figure 4.2, where both the Wilson loop and the spatial Polyakov loop correlator are plotted as functions of the distance Δx. While for small distances the non-local connection lines seem to be important, their impact decreases at larger distances where both quantities agree.

Since Eq. (4.4) wraps around the x_i-direction one may ask whether the apparent non-locality can be removed. Although we are interested in the infrared dynamics of QCD, a local operator also inevitably carries ultraviolet fluctuations that must be regularized. Moreover, the non-local gauge symmetry prohibits the construction of fully local operators that do not carry part of the dynamics. It follows that the traced Polyakov loop in Eq. (4.4) is a gauge-invariant quantity that is sensitive to the infrared but sufficiently local in space.

Let us now introduce a scalar field via the traced spatial Polyakov loop (4.4) and discuss how it emerges naturally as a variable in the action (4.1). To that end, the operator in the trace in Eq. (4.5) can be written as

$$\tilde{P}_i(x) = \mathcal{P}e^{-i\,g\int_0^L \mathcal{A}_i(x)\,dx_i} = e^{\mathrm{i}\phi_i(x)}\,, \tag{4.7}$$

where we use the same notation $x = (t, \boldsymbol{x})$ as before. Here we have introduced the algebra-valued field,

$$\phi_i(x) = \phi_i^a(x)\, t^a \,, \qquad t^a = \sigma^a/2 \,, \tag{4.8}$$

with the Pauli matrices σ^a, $a = 1, 2, 3$, for $\tilde{P}_i \in SU(2)$. This invites us to define the gauge-invariant scalar field $\varphi_i(x)$ as

$$\frac{1}{N_c} \operatorname{Tr} \tilde{P}_i \equiv P_i = \cos\varphi_i . \tag{4.9}$$

Similar to P_i, the scalar field $\varphi_i(x)$ lacks any dependence on the spatial direction x_i that has been integrated out. On the other hand, the spatial Polyakov lines transform covariantly under gauge transformations $U \in SU(2)$, with $\tilde{P}_i \to U\tilde{P}_i U^\dagger$. It follows that the algebra element transforms in the same way,

$$\phi_i(x) \to U(x)\phi_i(x)U^\dagger(x) \,. \tag{4.10}$$

The gauge transformation can be used to diagonalize $\tilde{P}_i$ and hence ϕ_i. This fixes the gauge freedom to a spatial Polyakov or diagonalization gauge, where the eigenvalue field φ_i becomes proportional to the algebra field,

$$\phi_i(x) = \varphi_i(x) t^3 \,. \tag{4.11}$$

We emphasize that the scalar field φ_i is gauge invariant since it is defined as an eigenvalue of the operator ϕ_i. Moreover, φ_i is a suitable infrared degree of freedom that we have searched for and is directly linked to the gauge fields $A_i(x)$. To see this, we consistently use the Polyakov gauge for $\tilde{P}_i$, ϕ_i, and for $A_i(x)$ at all x_i, which corresponds to rotating them into the Cartan subalgebra. Then the path ordering in Eq. (4.7) can be dropped and we have the relation

$$\phi_i(x) = -g \int_0^L \mathrm{d}x_i A_i(x) = -gLA_i(x) \,, \tag{4.12}$$

where the last step can be done if the gauge transformation is also used to remove the x_i dependence in the gauge field $A_i(x)$. In the temporal direction such a gauge transformation enforces the Polyakov gauge. Note that in the evaluation above this is not introduced as a gauge but for elucidating the relation between the phase fields ϕ_i and the gauge field. However, this also entails that we can use a respective gauge in Eq. (4.1) to make the dependence of the action on the gauge covariant phase field ϕ_i and hence on the gauge invariant field φ_i apparent. Since we only want to illuminate this connection, we use this gauge in Eq. (4.1) in the following; the respective gauge fixing has been discussed in detail in [35] and literature therein.

Let us now single out the spatial direction x_3, choose the spatial Polyakov gauge as before, and reformulate the classical action in Eq. (4.1) in terms of $\phi_3(x)$. To that end we invert the relation in Eq. (4.12) and substitute into Eq. (4.1)

$$A_3(x) = -\frac{1}{gL}\phi_3(x) = -\frac{1}{gL}\varphi_3(x)t^3\,. \tag{4.13}$$

This leads us to the formulation of the classical action,

$$S_{\mathrm{YM}} = \frac{1}{2}\int_x \mathrm{Tr}\ F^2_{\bar{\mu}\bar{\nu}} + \int_x \mathrm{Tr}\ F^2_{3\bar{\mu}}\,, \tag{4.14a}$$

where $\bar{\mu} = 0, 1, 2$ and $\bar{x} = (x_0, x_1, x_2)$, and

$$\int_x \mathrm{Tr}\, F^2_{3\bar{\mu}} = \frac{1}{2}\int_x \mathrm{Tr}\,(\partial_3 A_{\bar{\mu}})^2 + \frac{g}{L}\int_{\bar{x}} \mathrm{Tr}\ \phi_3(\bar{x})\int_{x_3}[A_{\bar{\mu}}, \partial_3 A_{\bar{\mu}}] + \frac{1}{g^2L^2}\int_x \mathrm{Tr}(D_{\bar{\mu}}\phi_3)^2\,, \tag{4.14b}$$

with the covariant derivative $D_\mu = \partial_\mu - \mathrm{i}gA_\mu$. Here the gauge-invariant degree of freedom φ_3 enters directly.

Since we aim at establishing a kinetic theory formulation for the scalar field eventually, we make an additional approximate simplification. For the moment, we neglect $\partial_3 A_{\bar{\mu}}$ since it is expected to have little impact on the dynamics of ϕ_3. Then the first line of Eq. (4.14b) vanishes, and the second line, together with the pure gauge field part in Eq. (4.14a), comprises the action of a non-Abelian Higgs model in 2+1 dimensions, with

$$S_{\mathrm{YM}} \to L\left[\frac{1}{2}\int_{\bar{x}} \mathrm{Tr}\ F^2_{\bar{\mu}\bar{\nu}} + \frac{1}{g^2L^2}\int_x \mathrm{Tr}(D_{\bar{\mu}}\phi_3)^2\right]\,. \tag{4.15}$$

However, with or without this last step, Eq. (4.14) illuminates the dependence of the Yang-Mills action on the algebra field ϕ_3. The latter, in a conveniently chosen gauge, carries the dynamics of the respective gauge field component A_3. It is also suggestive that this allows for the construction of effective actions in terms of the algebra fields, well- or naturally suited to describe the low-energy equilibrium and infrared far-from-equilibrium dynamics of gauge theories.

In this work, we study the dynamics of the gauge condensate in terms of the two-point correlations of both the gauge-invariant Polyakov loop P and the gauge-invariant field φ defined in Eqs. (4.4) and (4.11). Here and in the following we will simplify the notation by setting $P \equiv P_2$ and $\varphi \equiv \varphi_2$.

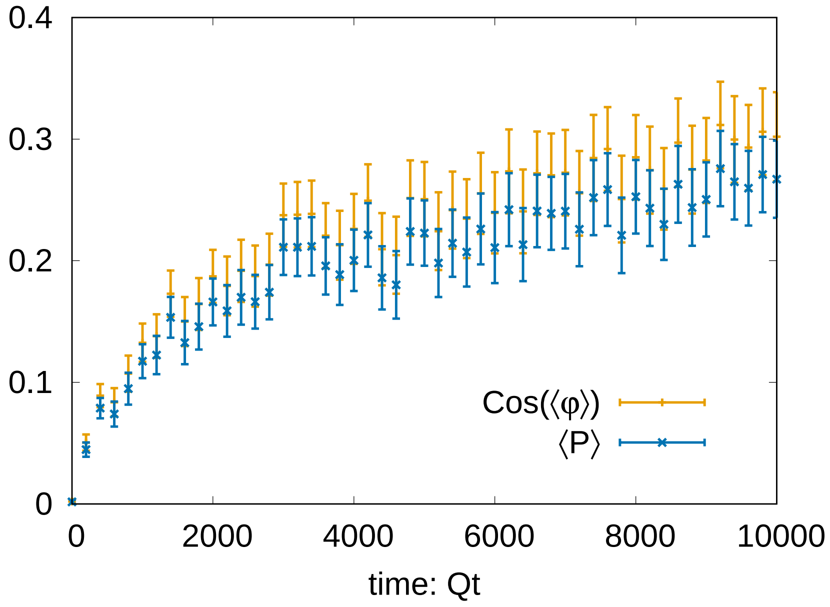

FIGURE 4.3: Comparison of the expectation value of the Polyakov loop to the Polyakov loop re-expressed in terms of the algebra-valued holonomous eigenvalue field for $N_s = 96$ lattice, $Q_s t = 1000$. This shows the approximate agreement of the one-point functions $\langle P\rangle \equiv \langle\cos(\varphi)\rangle \approx \cos(\langle\varphi\rangle)$.

4.2 Gauge-invariant condensation

With φ and P given by Eqs. (4.4) and (4.11), respectively, we have introduced two local order parameters that can be employed to study the dynamics of the gauge condensate as an alternative to the non-local Wilson loop. We now turn our attention to studying the condensate itself.

First, we will discuss the lattice simulations employed to evaluate the non-perturbative real-time evolution. Then, we will define our observables and discuss the signals for condensation. Finally, we will discuss the condensate fraction and the time evolution of the condensate.

4.2.1 Classical-statistical lattice simulations

The initial gluons produced in high energy heavy ion collisions carry momenta on the order of the saturation scale Q, at time $t \sim 1/Q$ in natural units [79, 118]. The system is considered strongly correlated despite the small running gauge coupling $\alpha_s(Q)$ due to the high initial gluon occupancies $f \sim 1/\alpha_s(Q)$. It follows that such a non-perturbative problem can be studied via classical-statistical lattice simulations [119, 120]. The characteristic initial over-occupation of gluons is translated into energy density $\sim Q^4/\alpha_s$

and fluctuations, which initializes the lattice gauge theory evolution. Throughout this study, quantities are given in terms of Q.

We discretize the $SU(N_c)$ gauge theory with $N_c = 2$ colors on a lattice with three spatial dimensions of size N_s and spacing a_s. The lattice gauge theory evolution is initialized as a superposition of transversely polarized gluon fields,

$$\mathcal{A}_j^a(t=0,\mathbf{p}) = \sqrt{\frac{f(0,p)}{2p}} \sum_\lambda c_\mathbf{p}^a \xi_j^{(\lambda)}(\mathbf{p}) + \text{c.c.}, \tag{4.16}$$

and their time derivatives,

$$E_j^a(t=0,\mathbf{p}) = \sqrt{\frac{f(0,p)p}{2}} \sum_\lambda c_\mathbf{p}^a \xi_j^{(\lambda)}(\mathbf{p}) + \text{c.c.} \tag{4.17}$$

Here, $\mathbf{p}$ denotes spatial momenta with $p = |\mathbf{p}|$, $\xi_j^{(\lambda)}$ the transverse polarization vectors, and $c_\mathbf{p}^a$ complex Gaussian random numbers with vanishing mean and unit variance. Index $a = 1, ..., N_c^2 - 1$ is the color index and $j = 1, 2, 3$ is the spatial index. The initial gluon over-occupation is parameterized by (with $A = 1.14$)

$$f(0,p) = \frac{QA}{4\pi\alpha_s p}\,\theta(Q-p). \tag{4.18}$$

The real-time evolution is realized by solving the classical Hamilton equations of motion in the temporal axial gauge $\mathcal{A}_0 = 0$. The equations of motion are formulated in a gauge covariant way, using $E_a^j(t,\mathbf{x})$ and link fields $U_j(t,\mathbf{x}) = \exp(ig\alpha_a\mathcal{A}_j(t,\mathbf{x}))$. For a detailed description of this standard technique we refer, e.g., to [3, 121, 122].

Our simulations are conducted on cubic lattices with $N_s = 48, 64, 96, 128$ lattice sites and the lattice spacing $Qa_s = 0.5$ (with $L = N_s a_s$). To obtain sufficient statistics, we average our observables over 200 configurations.

4.2.2 Evolution of one-point functions

Before defining and discussing condensates, we first consider the evolution of the one-point functions $\langle P\rangle$ and $\langle\varphi\rangle$. Often considering the expectation values of order parameters is sufficient to describe condensation phenomena. However, in our case this would be misleading because $\langle P\rangle$ grows while $\langle\varphi\rangle$ decreases with time.

Their relation is depicted in Figure 4.3, where $\langle P\rangle$ and $\cos(\langle\varphi\rangle)$ are shown as functions of time. One observes their approximate agreement,

$$\langle P\rangle \equiv \langle\cos(\varphi)\rangle \approx \cos(\langle\varphi\rangle). \tag{4.19}$$

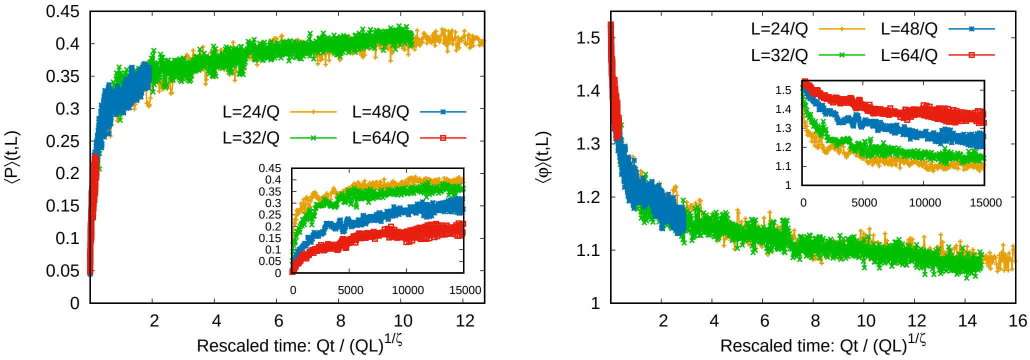

FIGURE 4.4: Expectation values of the spatial Polyakov loop and the scalar algebra field as functions of rescaled time for different volumes. The Polyakov loop is rescaled with $\zeta = 0.24$ and the algebra field is rescaled with $\zeta = 0.25$, both exhibiting scaling behavior in time. We also observe that $\langle \phi \rangle$ starts from $\approx \pi/2$ and decreases with time, which is in line with Figure 4.3. In the context of condensation, the connected correlator becomes increasingly independent of $\langle \phi \rangle$, indicating Bose-Einstein condensation behavior.

Since they start close to zero due to the large initial occupancies, the scalar field is initially $\langle \varphi \rangle \approx \pi/2$ and then decreases with time. This would naïvely contradict the emergence of a condensate.

However, one finds volume scaling in the time evolution of both $\langle P \rangle$ and $\langle \varphi \rangle$. This is shown in Figure 4.4 where these one-point functions are shown for different volumes as functions of rescaled time in the main plots and original time Qt in the insets. The rescaling proceeds by dividing time according to $Qt/(QL)^{1/\zeta}$ with the scaling exponents $\zeta = 0.24$ and $\zeta = 0.25$ for the Polyakov loop and the algebra field expectation values, respectively. [2] In this case, curves for different volumes fall on top of each other, indicating universal dynamics on a size-dependent time scale. We will argue in the following section using two-point correlators that this time scale is associated to a condensate formation time.

Although the macroscopic field $\langle \varphi \rangle$ decreases with time, a condensate can still emerge in the zero mode of the connected two-point function $\langle \varphi \varphi^\dagger \rangle_c$ that will be introduced in the following subsection. Such a phenomenon is not uncommon. For instance, scalar quartic models of inflation [123] can have a decaying inflaton $\langle \varphi \rangle$ while the zero mode of the connected correlator $\langle \varphi \varphi^\dagger \rangle_c(p{=}0)$ grows with time indicating the onset of condensation [4, 124]. This motivates us to define condensate fractions as connected correlators of the order parameters.

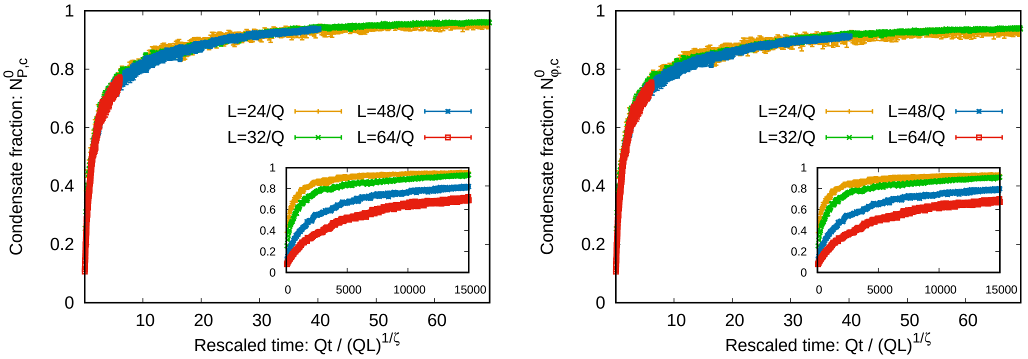

FIGURE 4.5: Condensate fractions (4.21) of the connected correlators $\langle PP^\dagger\rangle_c$ and $\langle\varphi\varphi^\dagger\rangle_c$ as functions of rescaled time for different lattice volumes. All curves fall on top of each other and therefore show the emergence of a volume-independent condensate fraction. The rescaled quantities have scaling exponents $\zeta = 0.31$ and $\zeta = 0.34$, respectively, using the procedure in Appendix D (cf., Table 4.1). (*Insets:*) Condensate fraction as a function of time, not rescaled, for the respective correlators.

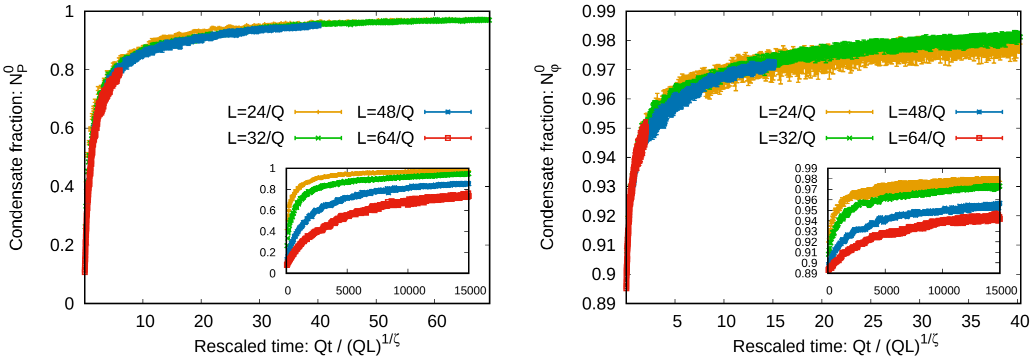

FIGURE 4.6: Condensate fraction (Eq. (4.23)) of the full Polyakov loop correlator (left) and the full algebra field correlator (right) as a function of finite-size rescaled time for different volumes. All curves fall on top of each other and therefore show the emergence of a volume-independent condensate fraction. The scaling exponents ζ are identical to those in Figure 4.5. Insets: Condensate fraction as a function of time, not rescaled, for the respective correlators.

4.2.3 Condensate fractions

In order to study condensation for the suggested local order parameters, we first consider a general quantity $\mathcal{O}$, for which we can define a condensate fraction. We propose to study the connected two-point correlators,

$$\langle\mathcal{O}\mathcal{O}^\dagger\rangle_c(t,\Delta x,L) = \langle\mathcal{O}\mathcal{O}^\dagger\rangle - \langle\mathcal{O}\rangle\langle\mathcal{O}\rangle^*, \tag{4.20}$$

where $\mathcal{O}$ is either P or φ, in order to explicitly distinguish their dynamics from the one-point functions $\langle\mathcal{O}\rangle$ discussed in the previous subsection.

---

[2] More precisely, we obtain $\zeta = 0.24 \pm 0.03$ and $\zeta = 0.25 \pm 0.03$ by employing the method presented in Appendix D.

Observable	Δx	Exponent
$\langle PP^\dagger\rangle_c(t,\Delta x,L)$	$L/2$	$\zeta = 0.36 \pm 0.04$
$\langle PP^\dagger\rangle_c(t,\Delta x,L)$	$L/4$	$\zeta = 0.31 \pm 0.09$
$\langle \varphi\varphi^\dagger\rangle_c(t,\Delta x,L)$	$L/2$	$\zeta = 0.37 \pm 0.03$
$\langle \varphi\varphi^\dagger\rangle_c(t,\Delta x,L)$	$L/4$	$\zeta = 0.34 \pm 0.03$
$\langle PP^\dagger\rangle(t,\Delta x,L)$	$L/2$	$\zeta = 0.31 \pm 0.04$
$\langle PP^\dagger\rangle(t,\Delta x,L)$	$L/4$	$\zeta = 0.27 \pm 0.06$
$W(t,\Delta x,L)$	$L/2$	$\zeta = 0.27 \pm 0.04$
$W(t,\Delta x,L)$	$L/4$	$\zeta = 0.24 \pm 0.06$

TABLE 4.1: Summary of scaling exponents for different condensate observables. These values and their uncertainties have been estimated using a similar χ^2-procedure as in [3–5], which we outline in Appendix D. The scaling exponent ζ is compared for the two sufficiently local observables studied in this work, the connected Polyakov loop correlator and the algebra field, to the Polyakov loop correlator in (4.23), and to the Wilson loop expectation value studied in [5].

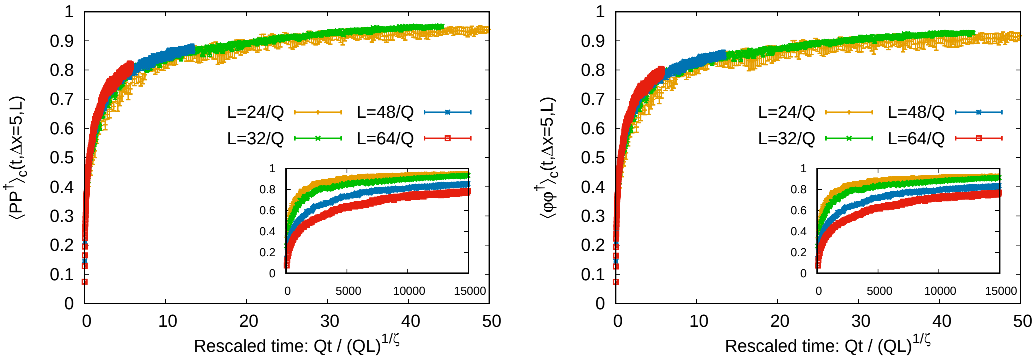

FIGURE 4.7: Rescaled connected correlators $\langle PP^\dagger\rangle_c$ and $\langle\varphi\varphi^\dagger\rangle_c$ normalized by their values at $\Delta x = 0$ for fixed $Q\Delta x = 5$, with a reduced time extent ($Qt \leq 15000$). The scaling exponents ζ are identical to those in Figure 4.5.

In one dimension, we define the condensate fraction for a given length L by integrating with respect to the spatial extent Δx and dividing out the length γL, [3]

$$N^0_{\mathcal{O},c}(t,L) = \frac{1}{\gamma L}\int_0^{\gamma L} d\Delta x\, \frac{\langle \mathcal{O}\mathcal{O}^\dagger\rangle_c(t,\Delta x,L)}{\langle \mathcal{O}\mathcal{O}^\dagger\rangle_c(t,\Delta x{=}0,L)}, \tag{4.21}$$

where $\gamma < 1$ is a real parameter. The length L in the x_2-direction spans the length of the lattice. Since the lattice is periodic, the correlators are symmetric around $\Delta y = L/2$, which constitutes the longest physical distance. In our numerics, we, therefore, use $\gamma = 1/4$ and show that our results are consistent with $\gamma = 1/2$.

---

[3] We have checked that other powers like $\frac{1}{(\gamma L)^2}\int_0^{\gamma L} d\Delta x\, \Delta x$ lead to similar scaling exponents.

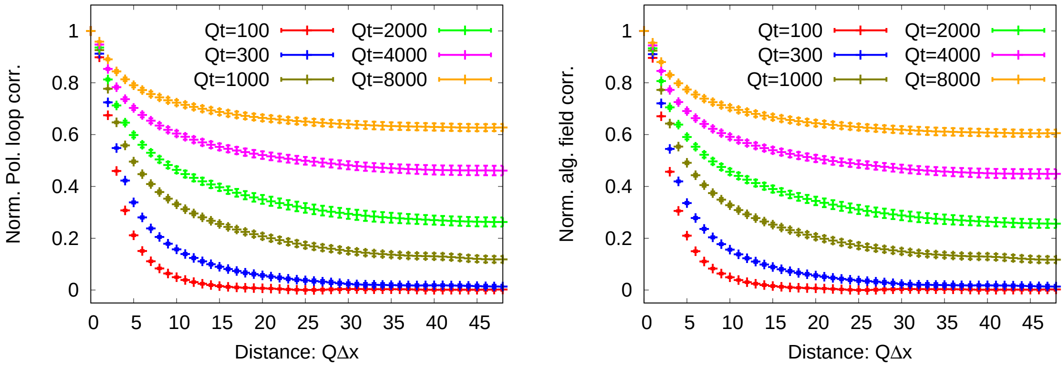

FIGURE 4.8: Time evolution of the normalized connected Polyakov loop correlator $\langle PP^\dagger\rangle_c(\Delta x)/\langle PP^\dagger\rangle_c(\Delta x{=}0)$ (left) and normalized connected algebra field correlator $\langle\varphi\varphi^\dagger\rangle_c(\Delta x)/\langle\varphi\varphi^\dagger\rangle_c(\Delta x{=}0)$ (right) shown for six times $Qt = 100, 300, 1000, 2000, 4000, 8000$ on a $N_s = 96$ lattice. Clear growth of condensate is demonstrated for both order parameters.

Following our previous discussion about the generalized notion of condensation, we make several observations about the condensate fraction in Eq. (4.21). Firstly, the integral $\int d\Delta x \langle\mathcal{O}\mathcal{O}^\dagger\rangle_c(t,\Delta x,L)$ resembles a Fourier transformation, or rather a Wigner transform for a vanishing momentum $p = 0$. Since $\langle\mathcal{O}\mathcal{O}^\dagger\rangle_c(t,\Delta x{=}0,L)$ can be interpreted as an integral over all momentum modes $\int dp\langle\mathcal{O}\mathcal{O}^\dagger\rangle_c(t,p,L)$ by Fourier transforming $\langle\mathcal{O}\mathcal{O}^\dagger\rangle_c(t,\Delta x,L)$, dividing the zero mode by this quantity corresponds to its fraction. Finally, dividing by a suitable volume or length element bounds it to unity and allows one to interpret this zero-mode fraction as a condensate if it becomes large and independent of the lattice size. However, such lattice size independence is difficult to show since the condensate fraction keeps growing due to the far-from-equilibrium dynamics. Therefore we define a volume-dependent condensate formation time in a similar way as for Wilson loops in [5] and relativistic and nonrelativistic scalar field theories in [4], as

$$t_{\text{cond}} = (QL)^{1/\zeta}. \tag{4.22}$$

Rescaling time by t/t_{cond} gets rid of the remaining volume dependence in the evolution of the condensate fractions $N^0_{\mathcal{O},c}$, as we will demonstrate numerically below, finally signaling the emergence of a condensate. On the other hand, an interpretation in terms of a condensate is not possible if this quantity remains volume-dependent. This is the case in thermal equilibrium. We note that this particular form of condensate formation is a genuinely far-from-equilibrium phenomenon, usually requires large occupation numbers, and is often associated with an inverse particle cascade that occupies the zero mode, as observed for scalar theories [4, 125].

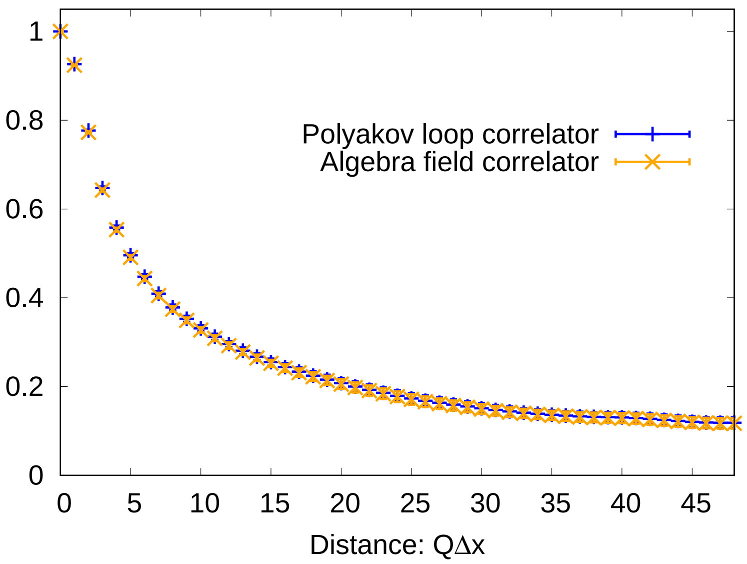

FIGURE 4.9: Comparative analysis of the normalized connected Polyakov loop correlator $\langle PP^\dagger\rangle(\Delta x)/\langle PP^\dagger\rangle(\Delta x{=}0)$ and the normalized connected algebra field correlator $\langle\varphi\varphi^\dagger\rangle(\Delta x)/\langle\varphi\varphi^\dagger\rangle(\Delta x{=}0)$ on a lattice with size $N_s = 96$ at time $Qt = 1000$, as in Figure 4.2 and Figure 4.8.

In Figure 4.5, we demonstrate the emergence of a volume-independent condensate fraction for both the connected Polyakov loop (left) and the connected algebra field correlators (right) computed using Eq. (4.21). In particular, we show $N^0_{P,c}$ and $N^0_{\varphi,c}$ for four different volumes as functions of time Qt in the insets, which yields a volume-dependent evolution. In contrast rescaling time by t_{cond} leads to volume-independent curves, as visible in the main panels. The initial growth of the zero mode necessarily ceases as the volume becomes correlated; this is demonstrated in the figure as the zero mode grows with time for each lattice size and then levels off at the time scale $\sim t_{\text{cond}}$.

The time scaling is characterized by the scaling exponent ζ entering t_{cond} in (4.22). We find for the condensate fraction of the connected Polyakov loop correlator, $\zeta = 0.31$, and for the connected algebra field correlator, $\zeta = 0.34$. The collapse of the curves onto one another in Figure 4.5 illustrates the volume-independent nature of the condensation phenomenon.

Although the dynamics is captured mainly by the connected correlators, we also check the condensate fraction scaling in terms of the full two-point functions of the spatial Polyakov loop and the algebra field in Figure 4.6. For a generic order parameter $\mathcal{O}$, this condensate fraction is given as:

$$N^0_{\mathcal{O}}(t,L) = \frac{1}{\gamma L}\int_0^{\gamma L} d\Delta x\, \frac{\langle\mathcal{O}\mathcal{O}^\dagger\rangle(t,\Delta x,L)}{\langle\mathcal{O}\mathcal{O}^\dagger\rangle(t,\Delta x{=}0,L)}. \tag{4.23}$$

The condensate fractions for the full correlators scale with similar exponents ζ as their respective connected parts.

In Table 4.1, we summarize the scaling exponents for the connected correlators and compare them to the scaling results of $N_P^0(t, L)$ and to those found in the previous publication [5] for the Wilson loop expectation value using our conventions. We note that the latter two quantities are intrinsically connected to each other but are not the same, as shown in Figure 4.1 and Figure 4.2. We observe that all of the extracted scaling exponents agree within statistical error, while showing a slight systematic dependence on the maximal distance Δx in the integrals. For $L/4$ the value for ζ tends to be around $10 - 15\%$ smaller than for $L/2$.

We then check the scaling of the connected correlators $\langle PP^\dagger \rangle$ and $\langle \varphi\varphi^\dagger \rangle$ in Eq. (4.20) at a fixed Δx, as shown in Figure 4.7. Interestingly, both the Polyakov loop and the algebra field correlators show the same scaling as their integrated counterparts in Figure 4.5. We find the values $\zeta = 0.31$ for the connected Polyakov loop correlator and $\zeta = 0.34$ for the connected algebra field correlator. This implies that not only correlations at large distances grow in this self-similar way, but also at finite distances in a similar fashion.

To further visualize this condensation phenomenon, we show the time evolution for the connected Polyakov loop and algebra field correlators for a lattice of size $N_s = 96$ in Figure 4.8. The connected correlators are plotted as functions of the distance Δx for six different times. One observes that for early times $Qt = 100$ and 300, both correlations are zero are large distances, signaling no condensate. However, at $Qt \gtrsim 1000$ a plateau has started to form at all distances, which further grows over time. This demonstrates a phase transition between a phase without and one with a condensate, where the condensate formation time scales with volume according to t_{cond} in Eq. (4.22).

Interestingly, these connected correlators agree even quantitatively, as shown in Figure 4.9. A similar agreement is known from (non-relativistic) scalar models [126]. There field correlations associated to the particle number can be dominated by excitations of the fluctuating phase-angle fields at sufficiently low momenta during Bose-Einstein condensation far from equilibrium. This observation provides another interesting analogy to scalar systems.

4.3 Conclusion

In this chapter we have demonstrated the existence of gauge condensation in overoccupied QCD plasmas. Two order parameters related to the Wilson loop demonstrate the build up of a macroscopic zero mode characteristic of condensation phenomena. These order parameters are the spatial Polyakov loop and algebra-valued scalar holonomous eigenvalue field, which form connected two-point correlation functions of which the condensate is obtained from their zero modes.

Through classical-statistical lattice simulations of the Yang-Mills plasma with large gluon densities and weak coupling, we have observed the emergence of condensate fractions on time scales $t_{\text{cond}} \sim L^{1/\zeta}$. The extracted values for the universal scaling exponent ζ are consistent with the different correlators employed and also agree with previous studies for the spatial Wilson loop within error. We have shown that the growth of the corresponding zero modes can also be seen in the correlations at large distances and is independent of the dynamics of the one-point functions of the order parameters.

The algebra-valued local scalar field can be related to scalar Bose condensation. Furthermore, the use of a local scalar field allows us to construct effective actions in terms of the algebra field, which is naturally suited to describe infrared dynamics far from equilibrium. We have constructed a suitable effective action and leave the connection to kinetic or other approaches to future studies.

The findings presented in this study contribute to the ongoing quest for a deeper understanding of the non-equilibrium dynamics of QCD matter. Moreover, they provide valuable insights into the challenges associated with defining gauge condensation and offer new perspectives on the early-time evolution of heavy-ion collisions. This work further paves the way for investigations into the rich physics of non-equilibrium QCD and its connections to other areas of theoretical and experimental physics.

Chapter 5

Conclusion

In this chapter we summarize our results and provide an outlook for future research directions in the study of non-Abelian gauge theories. We refer to the conclusions presented in Section 3.5 and Section 4.3 for detailed discussions.

In the first half of this thesis, we presented non-trivial effects on charge transport in high-temperature QCD plasmas due to sphaleron transitions. We modified the anomalous hydrodynamic equations of motion to explicitly include dissipative effects sourced by sphaleron transitions. Within this framework, dissipation due to sphaleron transitions is incorporated as a damping term proportional to the sphaleron transition rate, which depletes the net axial charge imbalance of all fermion flavors and contributes positively to entropy production in the system. Then, by linearizing the hydrodynamic equations around a space-time independent background, we investigated the coupled dynamics of vector and axial charge perturbations in a charge neutral background and contrasted our results including sphaleron damping to the traditional behavior of a Chiral Magnetic Wave. When sphaleron damping is taken into consideration, a characteristic wavenumber scale k_{CMW} emerges. This scale characterizes the hydrodynamic behavior of the charge modes and depends on the magnetic field strength and sphaleron transition rate. Finally, we studied the time evolution of linearized vector/axial charge perturbations and demonstrated the strong dependence of diffusion and charge separation on both the magnetic field strength and the sphaleron transition rate. We further quantified the amount of charge separation in terms of the electric dipole moment, and determined its dependence on the sphaleron rate. For realistic values of the sphaleron transition rate, the charge separation can easily be suppressed by a factor of two compared to the situation where dissipative effects due to sphaleron transitions are not taken into account.

Our central result directly impacts the experimental search for chiral transport phenomena in heavy ion collisions. We find that charge separation is highly sensitive to the sphaleron transition rate. The search for chiral phenomena in heavy ion collisions is ongoing and requires further clarification and investigations on the theory side. Our results show that, based on the magnetic field and the sphaleron transition rate, the signal for the CME in heavy ion collisions is lower than had been originally expected. Our results should be taken into account when looking for a signal in heavy ion collision experiments.

The sensitivity to the sphaleron transition rate also conceivably opens up an avenue to experimentally constrain this quantity. Such constraints can confront the current lattice calculations and also provide a unique way to probe the topological properties of QCD at high temperatures. This motivates a more careful and comprehensive treatment of axial charge dynamics. In the future, it is important to incorporate fluctuations of axial charge sourced by sphaleron transitions in the current framework.

In the second half of this thesis, we presented evidence of gauge condensation in the far-from equilibrium matter created in heavy ion collisions. Two order parameters related to the Wilson loop demonstrate the build up of a macroscopic zero mode characteristic of condensation phenomena. These order parameters are the spatial Polyakov loop and algebra-valued scalar holonomous eigenvalue field, which form connected two-point correlation functions of which the condensate is obtained from their zero modes. Using classical-statistical lattice simulations, we observe the emergence of a condensate fraction on a characteristic time scale $t_{\text{cond}} \sim L^{1/\zeta}$. The extracted values for the universal scaling exponent ζ are consistent for both the spatial Polyakov loop and the algebra field correlators. Additionally, these agree with previous studies for the spatial Wilson loop within error. We have shown that the growth of the corresponding zero modes can also be seen in the correlations at large distances and is independent of the dynamics of the one-point functions of the order parameters.

Our results highlight that the formation of a condensate in the early stages of a heavy ion collision is nontrivial. For instance, it is consequential when formulating an effective kinetic theory to describe the infrared dynamics. Extracting a local order parameter such as the algebra field correlator allows for the construction of an effective action that describes these dynamics. Furthermore, the algebra field correlator can be directly compared to scalar order parameter fields that describe condensation in other over-occupied systems. Such a comparison gives us further insight into far-from-equilibrium universality classes and motivates further investigation.

Acknowledgements

A very special thanks is in order to my co-advisors, Jan Pawlowski and Jürgen Berges. Thank you both for believing in me and for everything you've done to help and guide me during my time in Heidelberg.

Another very special thanks to Sören Schlichting, who is like the sun because you absorb the energy and enthusiasm he radiates and it pushes you to be a better researcher. I am immensely grateful for our collaboration and for his advice and mentoring over the past few years.

I am grateful for the advice I have received and discussions I've had with my mentors in Stony Brook, Dima Kharzeev and Luis Alvarez-Gaume. I've also benefited greatly from discussions I've had with Rob Pisarski, Zohar Komargodski, Nikita Nekrasov, Matthias Kaminski, Alan Calder, and everyone in the Nuclear Theory Group at Stony Brook.

I've had the great pleasure of collaborating with Kirill Boguslavski, who has graciously shared his knowledge of simulations and physics with me. A groisen dank, Kirill! I've also had the great pleasure of working with Tara Butler as she finished her Master's thesis with us, and for our discussions on everything, from physics to the miscellaneous. I've also greatly appreciated discussions with Master's student Parham Radpay, who worked adjacent to Tara and me.

A special thank you to my friends who graciously read this manuscript and provided vital feedback: Yanky Landau, Julio Virrueta, Dennis Bollweg, Viktoria Noel, and Adam Takacs. You're the greatest, and thanks for being great friends as well.

I am indebted to my other colleagues who have become my friends: Roli, Janhavi, Vilija, Cedric, Louis, Stefan, Alvaro, Catherine, Dallas, Felipe, Aleksas, Julian, and Freddy. And to my friends outside the field, for keeping me sane. I want to especially acknowledge Gina, Brendan, Kathryn, Sarah, Shannon, Ammo, Alex, Molly, Haley, Gordon, Jason, Meghan, Ilana, Janell, and Mars. Your support and friendship means the world to me.

Finally, I could not have done any of this without the love and support from my family, especially my parents, Daniel and Deirdre, my siblings Jackie, Kara, and Danny, and my grandmothers Phyllis and Claire.

Appendix A

Divergence identities derivation

In Chapter 3, we present three divergences used in our calculations: $\partial_\mu S^\mu$, the divergence of entropy current, and $\partial_\mu B^\mu$, $\partial_\mu \omega^\mu$, expressions for the divergence of magnetic field and vorticity from the ideal (non-dissipative) hydrodynamic equations. We provide details about the derivation of these expressions here.

A.1 Divergence of the entropy current

Let us first derive the divergence of the entropy current. The viscous correction to the entropy current in first order hydrodynamics is

$$S^\mu = \frac{(e+p)}{T} u^\mu - \frac{\mu_i}{T} j_i^\mu \tag{A.1}$$

where indexed terms i are summed over for $i = V, A$. Immediately, the divergence takes the form

$$\partial_\mu S^\mu = \partial_\mu \left(\frac{(e+p)}{T} u^\mu \right) - \partial_\mu \left(\frac{\mu_i}{T} n_i u^\mu + \frac{\mu_i}{T} \nu_i^\mu \right) \tag{A.2}$$

We focus on the first term on the right hand side of Eq. (A.2). From the longitudinal projection on the divergence of the energy-momentum tensor, we have

$$\partial_\mu (e+p) u^\mu = u^\mu \partial_\mu p - \tau^{\mu\nu} \left(\partial_\mu u_\nu \right) - u_\nu \left(\partial_\mu T^{\mu\nu} \right). \tag{A.3}$$

Now, using the thermodynamic relations $Ts = (e+p) - \mu_i n_i$ and $dP = sdT + n_i d\mu_i$, we can express

$$\frac{1}{T} u^\mu \partial_\mu p \quad = \quad -(e+p) u^\mu \left(\partial_\mu \frac{1}{T} \right) + n_i u^\mu \left(\partial_\mu \frac{\mu_i}{T} \right) \tag{A.4}$$

Dividing Eq. (A.3) by T, and then combining with Eq. (A.4), we obtain

$$\partial_\mu \left(\frac{e+p}{T}u^\mu\right) = -\frac{1}{T}\tau^{\mu\nu}\left(\partial_\mu u_\nu\right) - \frac{1}{T}u_\nu\left(\partial_\mu T^{\mu\nu}\right) + n_i u^\mu \left(\partial_\mu \frac{\mu_i}{T}\right). \tag{A.5}$$

We substitute this result into Eq. (A.2), and obtain

$$\partial_\mu S^\mu = -\frac{1}{T}\tau^{\mu\nu}\left(\partial_\mu u_\nu\right) - \left(j_i^\mu - n_i u^\mu\right)\left(\partial_\mu \frac{\mu_i}{T}\right) - \frac{1}{T}u_\nu\left(\partial_\mu T^{\mu\nu}\right) - \frac{\mu_i}{T}\left(\partial_\mu J_i^\mu\right). \tag{A.6}$$

Identifying $j_i^\mu - n_i u^\mu = \nu_i^\mu$, we evaluate

$$u_\nu\left(\partial_\mu T^{\mu\nu}\right) = -eq_f E_\lambda \left(j_V^\lambda - n_V u^\lambda\right), \tag{A.7}$$

where in the last step we used the fact that E^μ is a spacelike vector (i.e $u_\mu E^\mu = 0$). After making the appropriate substitutions into Eq. (A.6), it is straightforward to find

$$\partial_\mu S^\mu = -\frac{1}{T}\tau^{\mu\nu}\left(\partial_\mu u_\nu\right) - \nu_V^\mu\left(\left(\partial_\mu \frac{\mu_i}{T}\right) - \frac{eq_f}{T}E_\mu\right) - \nu_A^\mu\left(\partial_\mu \frac{\mu_A}{T}\right) - \frac{\mu_A}{T}\left(\partial_\mu J_A^\mu\right). \tag{A.8}$$

A.2 Divergence of vorticity and magnetic field

To find the identities for the divergences of vorticity ω^μ and magnetic field B^μ, we first note that both of these quantities can be expressed in an analogous way in terms of the components of the tensors $F_{\alpha\beta} = \partial_\alpha A_\beta - \partial_\beta A_\alpha$ and $\Omega_{\alpha\beta} = \frac{1}{2}\epsilon^{\mu\nu\alpha\beta}\partial_\alpha u_\beta$ according to

$$F_{\alpha\beta} = u_\alpha E_\beta - u_\beta E_\alpha - \epsilon_{\alpha\beta\gamma\delta}u^\gamma B^\delta , \tag{A.9}$$

$$\Omega_{\alpha\beta} = u_\lambda \omega_\beta - u_\beta \omega_\alpha - \epsilon_{\alpha\beta\gamma\delta}u^\gamma a^\delta , \tag{A.10}$$

where

$$a^\mu = \frac{1}{2}\epsilon^{\mu\nu\alpha\beta}u_\nu \Omega_{\alpha\beta} = \frac{1}{2}u_\nu \partial^\nu u^\mu \tag{A.11}$$

is the acceleration of the fluid. Since for sufficiently smooth fields $\partial_\mu \Omega^{\mu\nu} = 0$, we can then express the derivatives as

$$\partial_\mu B^\mu = \frac{1}{2}\epsilon^{\mu\nu\alpha\beta}(\partial_\mu u_\nu)F_{\alpha\beta} = -2\omega_\mu E^\mu + 2a_\mu B^\mu, \tag{A.12}$$

$$\partial_\mu \omega^\mu = \partial_\mu\left(\Omega^{\mu\nu}u_\nu\right) = (\partial_\mu u_\nu)\Omega^{\mu\nu} = 4a_\mu \omega^\mu . \tag{A.13}$$

By projecting the energy-momentum conservation equation $\Delta^\alpha{}_\nu \partial_\mu T^{\mu\nu}$, we obtain

$$(e+p)u^\mu \partial_\mu u^\alpha = -\Delta^\alpha{}_\nu \partial^\nu p + qe_f \Delta^\alpha{}_\nu F^{\nu\lambda} j_\lambda^V + \Delta^\alpha{}_\nu \partial_\mu \tau^{\mu\nu} \tag{A.14}$$

which, upon keeping only terms linear in gradients, becomes

$$(e+p)u^\mu\partial_\mu u^\alpha = -\Delta^\alpha{}_\nu\partial^\nu p + qe_f n^V E^\alpha + \mathcal{O}(\partial^2). \tag{A.15}$$

Collecting everything, we immediately obtain the identities

$$\begin{aligned}
\partial_\mu B^\mu &= -2\omega_\mu E^\mu - \frac{B^\mu}{e+p}\left((\partial_\mu p) - qe_f n_V E_\mu\right), &\text{(A.16)}\\
\partial_\mu \omega^\mu &= -\frac{2\omega^\mu}{e+p}\left((\partial_\mu p) - qe_f n_V E_\mu\right)\ . &\text{(A.17)}
\end{aligned}$$

Appendix B

Linearized hydrodynamic equations

In this appendix, we detail the linearization of the hydrodynamic equations used in Chapter 3.

B.1 Linearizing energy-momentum transport equations

Let us begin by linearizing the energy-momentum tensor. We write $\delta T^{\mu\nu}$

$$\delta T^{\mu\nu} \;=\; (\epsilon+P)\left(\delta u^{\mu}u^{\nu}+u^{\mu}\delta u^{\nu}\right)+\delta\epsilon u^{\mu}u^{\nu}+\delta P\left(g^{\mu\nu}+u^{\mu}u^{\nu}\right)-\eta\delta\sigma^{\mu\nu} \tag{B.1}$$

$\sigma^{\mu\nu}$ is defined in three spatial dimensions,

$$\sigma^{\mu\nu} \;=\; \Delta^{\mu\alpha}\Delta^{\mu\alpha}\left(\partial_{\alpha}u_{\beta}+\partial_{\beta}u_{\alpha}-\frac{2}{3}g_{\alpha\beta}\partial_{\gamma}u^{\gamma}\right), \tag{B.2}$$

such that $\delta\sigma^{\mu\nu}$ is

$$\delta\sigma^{\mu\nu} \;=\; \nabla^{\mu}\delta u^{\nu}+\nabla^{\nu}\delta u^{\mu}-\frac{2}{3}\Delta^{\mu\nu}\nabla_{\gamma}\delta u^{\gamma} \tag{B.3}$$

where we have defined $\nabla^{\mu}=\Delta^{\mu\alpha}\partial_{\alpha}$ and recognize

$$\Delta^{\mu\alpha}\Delta^{\nu\beta}g_{\alpha\beta}=\left(g^{\mu\alpha}+u^{\mu}u^{\alpha}\right)\left(g^{\nu\beta}+u^{\nu}u^{\beta}\right)g_{\alpha\beta}. \tag{B.4}$$

Decomposing $T^{\mu\nu}$ into tensor components:

$$\delta T^{00} = \delta\epsilon, \qquad \delta T^{0i} = (\epsilon + P)\delta u^i, \qquad \delta T^{i0} = (\epsilon + P)\delta u^i, \tag{B.5}$$

$$\delta T^{ij} = \left(\delta P + \frac{2}{3}\eta\partial_k\delta u^k\right)\delta^{ij} - \eta\left(\partial^i\delta u^j + \partial^j\delta u^i\right). \tag{B.6}$$

We take the divergence of the components, obtaining

$$\partial_\mu\delta T^{\mu0} = \partial_t\delta\epsilon + \partial_i\delta u^i(\epsilon + P) \tag{B.7}$$

$$\partial_\mu\delta T^{\mu i} = (\epsilon + P)\partial_t\delta u^i + \partial_i\delta P - \frac{1}{3}\eta\partial_i\partial_k\delta u^k - \eta\partial_k\partial^k\delta u_i. \tag{B.8}$$

Now, we spatially Fourier transform these equations to momentum space, via

$$\delta u^i(\mathbf{x}) = \int\frac{d^3k}{(2\pi)^3}e^{i\mathrm{k}\cdot\mathrm{x}}\delta u^i(\mathbf{k}), \tag{B.9}$$

and define the components of the velocity field,

$$u_L(\mathbf{k}) = \frac{k_i}{|\mathbf{k}|}\delta u^i(\mathbf{k}), \qquad u^i_\perp(\mathbf{k}) = u^i(\mathbf{k}) - \frac{k^i}{|\mathbf{k}|}u_L(\mathbf{k}). \tag{B.10}$$

From Eq. (B.7), we obtain

$$\partial_\mu T^{\mu0} = u_\nu\partial_\mu T^\mu = \partial_t\delta\epsilon + ik\delta u_L(\epsilon + P). \tag{B.11}$$

From the longitudinal projection of Eq. (B.8),

$$\begin{aligned}\frac{k_i}{|\mathbf{k}|}\partial_\mu T^{\mu i} &= k^\lambda\Delta_{\lambda\nu}\partial_\mu T^{\mu\nu} \\ &= (\epsilon + P)\partial_t\delta u_L + ik\delta P + \frac{4}{3}\eta\mathbf{k}^2\delta u_L.\end{aligned} \tag{B.12}$$

Then, from the transverse projection of Eq. (B.8), we find

$$\begin{aligned}\left(\delta_{ij} - \frac{k_ik_j}{|\mathbf{k}^2|}\right)\partial_\mu T^{\mu j} &= \left(\Delta_{i\lambda} - \frac{k_ik_\lambda}{|\mathbf{k}^2|}\right)\Delta_{\lambda\nu}\partial_\mu T^{\mu\nu} \\ &= (\epsilon + P)\partial_t\delta u^i_\perp + \eta\mathbf{k}^2\delta u^i_\perp.\end{aligned} \tag{B.13}$$

Since energy-momentum transport is not conserved due to the Lorentz force, we must also linearize the right-hand side of Eq. (3.3). It is important to note that we are considering only contributions from background vector charge fluctuations in this computation. First, we find the longitudinal component,

$$F_L \equiv \frac{k_\nu}{|\mathbf{k}|}F^{\nu\lambda}\delta j^V_\lambda = -n_V\mathbf{B}\cdot(\mathbf{k}\times\delta\mathbf{u}_\perp). \tag{B.14}$$

The transverse component of the right-hand side of Eq. (3.3) can be written

$$F_\perp^i \equiv \left(\delta_{ij} - \frac{k_i k_j}{|\mathbf{k}^2|}\right)\epsilon^{ijk} B_k \left(n_v \delta u_j - i k_j \sigma_{VV} T \delta \frac{\mu_V}{T} - i k_j \sigma_{VA} T \delta \frac{\mu_A}{T}\right). \tag{B.15}$$

We specialize these equations for a charge-neutral background such that the background vector charge $n_V = 0$. Then, we obtain the following identities:

$$\delta\left(\frac{\mu_{V/A}}{T}\right) = \frac{\delta\mu_{V/A}}{T}, \qquad Ts = \epsilon + P, \qquad \delta n_{A/V} = \chi_{A/V}\delta\mu_{A/V}. \tag{B.16}$$

We can evaluate Eqs. (B.14) and (B.15) at $n_v = 0$,

$$F_L \propto n_V \Rightarrow F_L = 0, \quad F_\perp^i = -\epsilon^{ijk} k_j B_k \left(\sigma_{VA}\delta\mu_A + \sigma_{VV}\delta\mu_V\right). \tag{B.17}$$

We collect the hydrodynamic equations for energy-momentum transport:

$$\begin{aligned}
\partial_t \delta\epsilon + ik(\epsilon+P)\delta u_L &= 0, && \text{(B.18)}\\
(\epsilon+P)\partial_t \delta u_L + ik\delta P + \frac{4}{3}\eta\mathbf{k}^2\delta u_L &= 0, && \text{(B.19)}\\
(\epsilon+P)\partial_t \delta u_\perp^i + \eta\mathbf{k}^2\delta u_\perp^i &= -\epsilon^{ijk} k_j B_k \left(\frac{\sigma_{VA}}{\chi_A}\delta n_A + \frac{\sigma_{VV}}{\chi_V}\delta n_V\right). && \text{(B.20)}
\end{aligned}$$

In this form, the hydrodynamic equations are ready to be modified as described in Chap. 3.

B.2 Linearizing charge transport equations

Let first linearize the vector charge transport equation. We start by writing δj_V^μ:

$$\begin{aligned}
\delta j_V^\mu = {} & \delta n_V u^\mu + n_V \delta u^\mu - \sigma_{VA} T \Delta^{\mu\nu}\partial_\nu \delta\frac{\mu_A}{T} - \sigma_{VV} T \Delta^{\mu\nu}\partial_\nu \delta\frac{\mu_V}{T}\\
& + \delta\sigma_{VB} B^\mu + \xi_V \delta\omega^\mu.
\end{aligned} \tag{B.21}$$

From the calculation of transport coefficients,

$$\delta\sigma_{VB} = C\left(1 - \frac{n_V \mu_V}{\epsilon+P}\right)\delta\mu_A = C\frac{Ts}{\epsilon+P}. \tag{B.22}$$

We take the divergence of Eq. (B.21) following the conventions in Sec. B.1,

$$\partial_\mu j_V^\mu = \partial_t \delta n_V + ikn_v u_L + \sigma_{VA} T\mathbf{k}^2\delta\frac{\mu_A}{T} + \sigma_{VV} T\mathbf{k}^2\delta\frac{\mu_V}{T} + C\frac{Ts}{\epsilon+P}(i\mathbf{k}\cdot\mathbf{B})\delta\mu_A. \tag{B.23}$$

Now, for the axial charge transport equation, we start again with δj^μ_A:

$$\delta j^\mu_A \quad = \quad \delta n_A u^\mu - \sigma_{AA} T \Delta^{\mu\nu} \partial_\nu \delta \frac{\mu_A}{T} - \sigma_{AV} T \Delta^{\mu\nu} \partial_\nu \delta \frac{\mu_V}{T} + \delta\sigma_{AB} B^\mu + \xi_A \delta\omega^\mu . \tag{B.24}$$

From the derived transport coefficients, $\delta\sigma_{AB}$ takes the form

$$\delta\sigma_{AB} = C\delta\mu_V + C\mu_V \frac{\delta(n_A \mu_A)}{\epsilon + P} . \tag{B.25}$$

Taking the divergence of Eq. (B.24), as done for vector charge transport, we find

$$\partial_\mu \delta j^\mu_A \quad = \quad \partial_t \delta n_A + \sigma_{AA} T \mathbf{k}^2 \delta \frac{\mu_A}{T} + \sigma_{VA} T \mathbf{k}^2 \delta \frac{\mu_V}{T} + C(i\mathbf{k}\cdot\mathbf{B}) \left(\delta\mu_V + \frac{\delta(n_A \mu_A)\mu_V}{\epsilon + P} \right) . \tag{B.26}$$

As with energy-momentum transport, $\partial_\mu \delta j^\mu_A$ is not conserved. Although we considered the Abelian part of Eq. (3.5) when we derived the transport coefficients in Sec. **??**, we did not consider the non-Abelian contribution that we added to incorporate sphaleron damping since it is purely dissipative and therefore contributes to positive entropy production. Since it still contributes to the non-conservation of axial charge, we include it in our axial charge transport equation in the form

$$\partial_\mu \delta j^\mu_{A,\mathrm{non-Abelian}} = -4\Gamma_{\mathrm{sph}} \delta \left(\frac{\mu_A}{T} \right) . \tag{B.27}$$

To get the charge transport equations in the form we want, we collect the equations and specialize for $n_V = 0$:

$$\partial_t \delta n_V + \frac{\sigma_{VV}}{\chi_V} \mathbf{k}^2 \delta n_V + \left(\frac{\sigma_{VA}}{\chi_A} \mathbf{k}^2 + iC \frac{\mathbf{k}\cdot\mathbf{B}}{\chi_A} \right) \delta n_A \quad = \quad 0 \tag{B.28}$$

$$\partial_t \delta n_A + \left(\frac{\sigma_{AA}}{\chi_A} \mathbf{k}^2 + \frac{4\Gamma_{\mathrm{sph}}}{\chi_A T} \right) \delta n_A + \left(\frac{\sigma_{AV}}{\chi_V} \mathbf{k}^2 + iC \frac{\mathbf{k}\cdot\mathbf{B}}{\chi_V} \right) \delta n_V \quad = \quad 0 \tag{B.29}$$

Appendix C

Multiflavor degenerate perturbation theory calculations

Below we explain the calculation of the eigenmodes in the two quark-flavor case. We focus for simplicity on the case $\chi_V = \chi_A = \chi$, where the matrix is symmetric and the calculations can be carried out in a familiar fashion. One finds that to leading order in the small k limit, the matrix $M_{ab}^{N_f=2}$ (Eq. 3.47) becomes

$$M_{k=0}^{N_f=2} = \begin{pmatrix} 0 & 0 & 0 & 0 \\ 0 & \gamma_{\mathrm{sph}} & 0 & \gamma_{\mathrm{sph}} \\ 0 & 0 & 0 & 0 \\ 0 & \gamma_{\mathrm{sph}} & 0 & \gamma_{\mathrm{sph}} \end{pmatrix}, \tag{C.1}$$

with eigenvalues

$$\lambda_1 = 2\gamma_{\mathrm{sph}}, \qquad \lambda_2 = \lambda_3 = \lambda_4 = 0. \tag{C.2}$$

We use degenerate perturbation theory to disentangle the three degenerate eigenvalues and determine the perturbations up to first order in k. By perturbing the matrix (C.1) with the first order contributions from (3.47), one obtains the first-order matrix,

$$M^{N_f=2}\Big|_{\mathcal{O}(k)} = \begin{pmatrix} 0 & ieq_u C\chi^{-1}\mathbf{k}\cdot\mathbf{B} & 0 & 0 \\ ieq_u C\chi^{-1}\mathbf{k}\cdot\mathbf{B} & \gamma_{\mathrm{sph}} & 0 & \gamma_{\mathrm{sph}} \\ 0 & 0 & 0 & ieq_d C\chi^{-1}\mathbf{k}\cdot\mathbf{B} \\ 0 & \gamma_{\mathrm{sph}} & ieq_d C\chi^{-1}\mathbf{k}\cdot\mathbf{B} & \gamma_{\mathrm{sph}} \end{pmatrix} . \tag{C.3}$$

We then can choose an orthonormal basis for the leading order eigenvectors that diagonalizes the degenerate subspace,

$$\mathbf{e}_1 = \frac{1}{\sqrt{2}}\left\{0,1,0,1\right\}, \tag{C.4}$$

$$\mathbf{e}_2 = \frac{1}{\sqrt{q_d^2+q_u^2}}\left\{q_d,0,q_u,0\right\}, \tag{C.5}$$

$$\mathbf{e}_3 = \frac{1}{\sqrt{2}}\left\{\frac{-q_u}{\sqrt{q_d^2+q_u^2}}, \frac{1}{\sqrt{2}}, \frac{q_d}{\sqrt{q_d^2+q_u^2}}, -\frac{1}{\sqrt{2}}\right\} \tag{C.6}$$

$$\mathbf{e}_4 = \frac{1}{\sqrt{2}}\left\{\frac{-q_u}{\sqrt{q_d^2+q_u^2}}, -\frac{1}{\sqrt{2}}, \frac{q_d}{\sqrt{q_d^2+q_u^2}}, \frac{1}{\sqrt{2}}\right\} . \tag{C.7}$$

By projecting the matrix (C.8) onto the leading order eigenvectors in Eq. (C.7), we obtain a matrix of the form

$$M^{N_f=2}\Big|_{\mathcal{O}(k)} = \begin{pmatrix} 2\gamma & k\vec{v}^T \\ k\vec{v} & kD \end{pmatrix} \tag{C.8}$$

where the matrix D describes the mixing between the degenerate leading order eigenvectors $(i,j=2,3,4)$,

$$kD_{ij} = \mathbf{e}_i^T\left(M^{N_f=2}\Big|_{\mathcal{O}(k)} - M^{N_f=2}_{k=0}\right)\mathbf{e}_j \ , \tag{C.9}$$

$$kD = \begin{pmatrix} 0 & 0 & 0 \\ 0 & -\frac{ieC\mathbf{k}\cdot\mathbf{B}}{\chi\sqrt{2}}\sqrt{q_d^2+q_u^2} & 0 \\ 0 & 0 & \frac{ieC\mathbf{k}\cdot\mathbf{B}}{\chi\sqrt{2}}\sqrt{q_d^2+q_u^2} \end{pmatrix}, \tag{C.10}$$

and the vector $\vec{v}$ describes the coupling between the degenerate eigenvectors $(i = 2, 3, 4)$ and the non-degenerate state $(j = 1)$

$$k\vec{v}_i = \vec{e}_i^T \left(M_{ab}^{N_f=2}\Big|_{\prime(k)} - M^{k0} \right) \vec{e}_1 \ , \qquad k\vec{v} = \begin{pmatrix} \frac{ieq_d q_u C\sqrt{2}\mathbf{k}\cdot\mathbf{B}}{\chi\sqrt{q_d^2+q_u^2}} \\ \frac{ie(q_d^2-q_u^2)C\mathbf{k}\cdot\mathbf{B}}{2\chi\sqrt{q_d^2+q_u^2}} \\ \frac{ie(q_d^2-q_u^2)C\mathbf{k}\cdot\mathbf{B}}{2\chi\sqrt{q_d^2+q_u^2}} \end{pmatrix} . \tag{C.11}$$

From the diagonal components of the matrix in (C.10), we immediately obtain the first-order corrections to the eigenvalues,

$$\begin{aligned} \lambda_2' &= 0, \\ \lambda_3' &= -\frac{ieC\mathbf{k}\cdot\mathbf{B}}{\chi\sqrt{2}}\sqrt{q_d^2+q_u^2}, \\ \lambda_4' &= \frac{ieC\mathbf{k}\cdot\mathbf{B}}{\chi\sqrt{2}}\sqrt{q_d^2+q_u^2}. \end{aligned} \tag{C.12}$$

Our shifted eigenvalues are $\lambda_{i,\mathrm{tot}} = \lambda_i + \lambda_i'$, and from the relation $\omega = i\lambda$ we obtain the shifted frequencies,

$$\omega_{2,\mathrm{new}} = 0, \tag{C.13}$$

$$\omega_{3,\mathrm{new}} = -\frac{eC}{\chi\sqrt{2}}\sqrt{q_d^2+q_u^2}|\mathbf{k}\cdot\mathbf{B}|, \tag{C.14}$$

$$\omega_{4,\mathrm{new}} = \frac{eC}{\chi\sqrt{2}}\sqrt{q_d^2+q_u^2}|\mathbf{k}\cdot\mathbf{B}|. \tag{C.15}$$

The first-order corrections to the eigenvectors take the form

$$\mathbf{e}_{1,\mathrm{new}} = \mathbf{e}_1 + \frac{k}{2\gamma}\vec{v}_i\mathbf{e}_i \ , \tag{C.16}$$

$$\mathbf{e}_{i,\mathrm{new}} = \mathbf{e}_i - \frac{k}{2\gamma}\vec{v}_i\mathbf{e}_1, \tag{C.17}$$

for $i = 2, 3, 4$. Using this prescription, we compute the shifted eigenvectors,

$$\mathbf{e}_{1,\text{new}} = \left\{ \frac{ieCq_u\mathbf{k}\cdot\mathbf{B}}{\gamma_{\text{sph}}\chi 2\sqrt{2}}, \frac{1}{\sqrt{2}}, \frac{ieCq_d\mathbf{k}\cdot\mathbf{B}}{\gamma_{\text{sph}}\chi 2\sqrt{2}}, \frac{1}{\sqrt{2}} \right\}, \tag{C.18}$$

$$\mathbf{e}_{2,\text{new}} = \left\{ \frac{q_d}{\sqrt{q_d^2+q_u^2}}, -\frac{ieCq_dq_u\mathbf{k}\cdot\mathbf{B}}{\chi\gamma_{\text{sph}}2\sqrt{q_d^2+q_u^2}}, \frac{q_u}{\sqrt{q_d^2+q_u^2}}, -\frac{ieCq_dq_u\mathbf{k}\cdot\mathbf{B}}{\chi\gamma_{\text{sph}}2\sqrt{q_d^2+q_u^2}} \right\}, \tag{C.19}$$

$$\begin{aligned}\mathbf{e}_{3,\text{new}} =& \Bigg\{ -\frac{q_u}{\sqrt{2(q_d^2+q_u^2)}}, \frac{1}{8}\left(4 - \frac{ieC\sqrt{2}\mathbf{k}\cdot\mathbf{B}(q_d^2-q_u^2)}{\chi\gamma_{\text{sph}}\sqrt{q_d^2+q_u^2}}\right), \frac{q_d}{\sqrt{2(q_d^2+q_u^2)}}, \\ & -\frac{1}{8}\left(4 + \frac{ieC\sqrt{2}\mathbf{k}\cdot\mathbf{B}(q_d^2-q_u^2)}{\chi\gamma_{\text{sph}}\sqrt{q_d^2+q_u^2}}\right) \Bigg\},\end{aligned} \tag{C.20}$$

$$\begin{aligned}\mathbf{e}_{4,\text{new}} =& \Bigg\{ -\frac{q_u}{\sqrt{2(q_d^2+q_u^2)}}, -\frac{1}{8}\left(4 + \frac{ieC\sqrt{2}\mathbf{k}\cdot\mathbf{B}(q_d^2-q_u^2)}{\chi\gamma_{\text{sph}}\sqrt{q_d^2+q_u^2}}\right), \frac{q_d}{\sqrt{2(q_d^2+q_u^2)}}, \\ & \frac{1}{8}\left(4 - \frac{ieC\sqrt{2}\mathbf{k}\cdot\mathbf{B}(q_d^2-q_u^2)}{\chi\gamma_{\text{sph}}\sqrt{q_d^2+q_u^2}}\right) \Bigg\}.\end{aligned} \tag{C.21}$$

Appendix D

Mean and error estimates for scaling exponents

In this appendix, we detail our mean and error esimates for the scaling exponents computed in Chapter 4.

Let us consider a time- and lattice size-dependent quantity $A(t, L)$ such as $\langle \mathcal{O} \rangle(t, L)$ or $N^0_{\mathcal{O},c}(t, L)$. We assume that its dependence can be reduced to a single argument that combines t and L using $t_{\text{cond}} = (QL)^{1/\zeta}$ as in (4.22). Our goal is to estimate the most likely value for the exponent ζ and its uncertainty such that the quantity A becomes a function of t/t_{cond} only. For this, we use an adapted version of the χ^2-procedure in [3–5].

In particular, we choose the lattice lengths $L_i \in \{24, 32, 48, 64\}$, with $L = N_s a_s$. We drop the transient early time evolution before scaling sets in considering only $t > \{100, 300, 300, 600\}$.Next, we vary ζ within $[0.2, 0.6]$ with 0.005 steps, rescale time using t_{cond}, which leads to $A_i(t, \zeta) \equiv A(t/t_{\text{cond}}(L_i, \zeta), L_i)$, and define

$$\chi^2(\zeta) = \frac{1}{5} \sum_{(i,j)} \frac{\int dt (A_i(t, \zeta) - A_j(t, \zeta))^2}{\int dt (A_i(t, \zeta))^2}. \tag{D.1}$$

Here, the tuple (i, j) runs over five pairs of lattice sizes which are explicitly chosen as $(i, j) \in \{(1, 2), (1, 3), (2, 3), (2, 4), (3, 4)\}$, and $\int dt$ integrates over a shared domain of the rescaled times of A_i.

We approximate the likelihood distribution of ζ as

$$P(\zeta) = \exp\left\{ -\frac{\chi^2(\zeta)}{2\chi^2_{min}} \right\}, \tag{D.2}$$

with χ^2_{min} being the minimum value of χ^2 in (D.1). Finally, the optimal value of the exponent $\bar{\zeta}$ and its uncertainty σ_ζ are estimated by fitting a Gaussian function of the form

$$f(\bar{\zeta}, \sigma_\zeta, \zeta) = \mathcal{N} \exp\left\{ -\frac{(\zeta_{opt} - \zeta)^2}{2\sigma_\zeta^2} \right\} \tag{D.3}$$

to the likelihood distribution $P(\zeta)$. Our results in Table 4.1 are given by $\zeta = \bar{\zeta} \pm \sigma_\zeta$.

Bibliography

[1] Ulrich W. Heinz. Towards the Little Bang Standard Model. *J. Phys. Conf. Ser.*, 455:012044, 2013. doi: 10.1088/1742-6596/455/1/012044.

[2] M. Mace, S. Schlichting, and R. Venugopalan. Off-equilibrium sphaleron transitions in the Glasma. *Phys. Rev. D*, 93(7):074036, 2016. doi: 10.1103/PhysRevD.93.074036.

[3] Juergen Berges, Kirill Boguslavski, Soeren Schlichting, and Raju Venugopalan. Universal attractor in a highly occupied non-Abelian plasma. *Phys. Rev. D*, 89 (11):114007, 2014. doi: 10.1103/PhysRevD.89.114007.

[4] A. Piñeiro Orioli, K. Boguslavski, and J. Berges. Universal self-similar dynamics of relativistic and nonrelativistic field theories near nonthermal fixed points. *Phys. Rev. D*, 92(2):025041, 2015. doi: 10.1103/PhysRevD.92.025041.

[5] Jürgen Berges, Kirill Boguslavski, Mark Mace, and Jan M. Pawlowski. Gauge-invariant condensation in the nonequilibrium quark-gluon plasma. *Phys. Rev. D*, 102(3):034014, 2020. doi: 10.1103/PhysRevD.102.034014.

[6] Julian S. Schwinger. A Theory of the Fundamental Interactions. *Annals Phys.*, 2: 407–434, 1957. doi: 10.1016/0003-4916(57)90015-5.

[7] Martin Schumacher. Nambu's Nobel Prize, the σ meson and the mass of visible matter. *Annalen Phys.*, 526(5-6):215–226, 2014. doi: 10.1002/andp.201400077.

[8] Martin Schumacher. Mass generation via the Higgs boson and the quark condensate of the QCD vacuum. *Pramana*, 87(3):44, 2016. doi: 10.1007/s12043-016-1256-0.

[9] Dominik J. Schwarz. The first second of the universe. *Annalen Phys.*, 12:220–270, 2003. doi: 10.1002/andp.200310010.

[10] Michael Buballa et al. EMMI rapid reaction task force meeting on quark matter in compact stars. *J. Phys. G*, 41(12):123001, 2014. doi: 10.1088/0954-3899/41/12/123001.

[11] Edward V. Shuryak. Quark-Gluon Plasma and Hadronic Production of Leptons, Photons and Psions. *Phys. Lett. B*, 78:150, 1978. doi: 10.1016/0370-2693(78)90370-2.

[12] Edward V. Shuryak. What RHIC experiments and theory tell us about properties of quark-gluon plasma? *Nucl. Phys. A*, 750:64–83, 2005. doi: 10.1016/j.nuclphysa.2004.10.022.

[13] Paul Romatschke and Ulrike Romatschke. Viscosity Information from Relativistic Nuclear Collisions: How Perfect is the Fluid Observed at RHIC? *Phys. Rev. Lett.*, 99:172301, 2007. doi: 10.1103/PhysRevLett.99.172301.

[14] A. A. Belavin, Alexander M. Polyakov, A. S. Schwartz, and Yu. S. Tyupkin. Pseudoparticle Solutions of the Yang-Mills Equations. *Phys. Lett. B*, 59:85–87, 1975. doi: 10.1016/0370-2693(75)90163-X.

[15] Larry D. McLerran, Emil Mottola, and Mikhail E. Shaposhnikov. Sphalerons and Axion Dynamics in High Temperature QCD. *Phys. Rev. D*, 43:2027–2035, 1991. doi: 10.1103/PhysRevD.43.2027.

[16] Guy D. Moore and Marcus Tassler. The Sphaleron Rate in SU(N) Gauge Theory. *JHEP*, 02:105, 2011. doi: 10.1007/JHEP02(2011)105.

[17] Lillian de Bruin and Sören Schlichting. Sphaleron damping and effects on vector and axial charge transport in high-temperature QCD plasmas. 9 2023.

[18] Stephen L. Adler. Axial vector vertex in spinor electrodynamics. *Phys. Rev.*, 177:2426–2438, 1969. doi: 10.1103/PhysRev.177.2426.

[19] J. S. Bell and R. Jackiw. A PCAC puzzle: $\pi^0 \to \gamma\gamma$ in the σ model. *Nuovo Cim. A*, 60:47–61, 1969. doi: 10.1007/BF02823296.

[20] M. F. Atiyah and I. M. Singer. The index of elliptic operators on compact manifolds. *Bull. Am. Math. Soc.*, 69:422–433, 1969. doi: 10.1090/S0002-9904-1963-10957-X.

[21] Kenji Fukushima, Dmitri E. Kharzeev, and Harmen J. Warringa. The Chiral Magnetic Effect. *Phys. Rev. D*, 78:074033, 2008. doi: 10.1103/PhysRevD.78.074033.

[22] Dam T. Son and Piotr Surowka. Hydrodynamics with Triangle Anomalies. *Phys. Rev. Lett.*, 103:191601, 2009. doi: 10.1103/PhysRevLett.103.191601.

[23] Dmitri E. Kharzeev and Ho-Ung Yee. Chiral Magnetic Wave. *Phys. Rev. D*, 83:085007, 2011. doi: 10.1103/PhysRevD.83.085007.

[24] D. T. Son and Ariel R. Zhitnitsky. Quantum anomalies in dense matter. *Phys. Rev. D*, 70:074018, 2004. doi: 10.1103/PhysRevD.70.074018.

[25] Max A. Metlitski and Ariel R. Zhitnitsky. Anomalous axion interactions and topological currents in dense matter. *Phys. Rev. D*, 72:045011, 2005. doi: 10.1103/PhysRevD.72.045011.

[26] D. E. Kharzeev, J. Liao, S. A. Voloshin, and G. Wang. Chiral magnetic and vortical effects in high-energy nuclear collisions—A status report. *Prog. Part. Nucl. Phys.*, 88:1–28, 2016. doi: 10.1016/j.ppnp.2016.01.001.

[27] Dmitri E. Kharzeev and Ho-Ung Yee. Anomalies and time reversal invariance in relativistic hydrodynamics: the second order and higher dimensional formulations. *Phys. Rev. D*, 84:045025, 2011. doi: 10.1103/PhysRevD.84.045025.

[28] Axel Brandenburg, Jennifer Schober, Igor Rogachevskii, Tina Kahniashvili, Alexey Boyarsky, Jurg Frohlich, Oleg Ruchayskiy, and Nathan Kleeorin. The turbulent chiral-magnetic cascade in the early universe. *Astrophys. J. Lett.*, 845(2):L21, 2017. doi: 10.3847/2041-8213/aa855d.

[29] Volker Koch, Soeren Schlichting, Vladimir Skokov, Paul Sorensen, Jim Thomas, Sergei Voloshin, Gang Wang, and Ho-Ung Yee. Status of the chiral magnetic effect and collisions of isobars. *Chin. Phys. C*, 41(7):072001, 2017. doi: 10.1088/1674-1137/41/7/072001.

[30] Qiang Li, Dmitri E. Kharzeev, Cheng Zhang, Yuan Huang, I. Pletikosic, A. V. Fedorov, R. D. Zhong, J. A. Schneeloch, G. D. Gu, and T. Valla. Observation of the chiral magnetic effect in ZrTe5. *Nature Phys.*, 12:550–554, 2016. doi: 10.1038/nphys3648.

[31] Miklos Horvath, Defu Hou, Jinfeng Liao, and Hai-cang Ren. Chiral magnetic response to arbitrary axial imbalance. *Phys. Rev. D*, 101(7):076026, 2020. doi: 10.1103/PhysRevD.101.076026.

[32] Mikhail Stephanov, Ho-Ung Yee, and Yi Yin. Collective modes of chiral kinetic theory in a magnetic field. *Phys. Rev. D*, 91(12):125014, 2015. doi: 10.1103/PhysRevD.91.125014.

[33] Amadeo Jimenez-Alba, Karl Landsteiner, and Luis Melgar. Anomalous magnetoresponse and the Stückelberg axion in holography. *Phys. Rev. D*, 90:126004, 2014. doi: 10.1103/PhysRevD.90.126004.

[34] Jean-Paul Blaizot, Francois Gelis, Jin-Feng Liao, Larry McLerran, and Raju Venugopalan. Bose–Einstein Condensation and Thermalization of the Quark Gluon Plasma. *Nucl. Phys. A*, 873:68–80, 2012. doi: 10.1016/j.nuclphysa.2011.10.005.

[35] Thomas Gasenzer, Larry McLerran, Jan M. Pawlowski, and Dénes Sexty. Gauge turbulence, topological defect dynamics, and condensation in Higgs models. *Nucl. Phys. A*, 930:163–186, 2014. doi: 10.1016/j.nuclphysa.2014.07.030.

[36] C. Ford, U. G. Mitreuter, T. Tok, A. Wipf, and J. M. Pawlowski. Monopoles, Polyakov loops and gauge fixing on the torus. *Annals Phys.*, 269:26–50, 1998. doi: 10.1006/aphy.1998.5841.

[37] U. G. Mitreuter, J. M. Pawlowski, and A. Wipf. Polyakov loops and fermionic zero modes QCD in two-dimensions on the torus. *Nucl. Phys. B*, 514:381–398, 1998. doi: 10.1016/S0550-3213(97)00733-5.

[38] J. Berges and D. Sexty. Bose condensation far from equilibrium. *Phys. Rev. Lett.*, 108:161601, 2012. doi: 10.1103/PhysRevLett.108.161601.

[39] Juergen Berges, Sebastian Scheffler, and Denes Sexty. Bottom-up isotropization in classical-statistical lattice gauge theory. *Phys. Rev. D*, 77:034504, 2008. doi: 10.1103/PhysRevD.77.034504.

[40] A. Dumitru, T. Lappi, and Y. Nara. Structure of longitudinal chromomagnetic fields in high energy collisions. *Phys. Lett. B*, 734:7–12, 2014. doi: 10.1016/j.physletb.2014.05.005.

[41] J. Berges, M. Mace, and S. Schlichting. Universal self-similar scaling of spatial Wilson loops out of equilibrium. *Phys. Rev. Lett.*, 118(19):192005, 2017. doi: 10.1103/PhysRevLett.118.192005.

[42] Dmitri E. Kharzeev. Topologically induced local P and CP violation in QCD x QED. *Annals Phys.*, 325:205–218, 2010. doi: 10.1016/j.aop.2009.11.002.

[43] Gerard 't Hooft. Symmetry Breaking Through Bell-Jackiw Anomalies. *Phys. Rev. Lett.*, 37:8–11, 1976. doi: 10.1103/PhysRevLett.37.8.

[44] Huey-Wen Lin et al. Parton distributions and lattice QCD calculations: a community white paper. *Prog. Part. Nucl. Phys.*, 100:107–160, 2018. doi: 10.1016/j.ppnp.2018.01.007.

[45] William Detmold, Robert G. Edwards, Jozef J. Dudek, Michael Engelhardt, Huey-Wen Lin, Stefan Meinel, Kostas Orginos, and Phiala Shanahan. Hadrons and Nuclei. *Eur. Phys. J. A*, 55(11):193, 2019. doi: 10.1140/epja/i2019-12902-4.

[46] Luis Alvarez-Gaume and Miguel A. Vazquez-Mozo. *An invitation to quantum field theory*, volume 839. 2012. doi: 10.1007/978-3-642-23728-7.

[47] Kazuo Fujikawa. On the Evaluation of Chiral Anomaly in Gauge Theories with Gamma(5) Couplings. *Phys. Rev. D*, 29:285, 1984. doi: 10.1103/PhysRevD.29.285.

[48] Luis Alvarez-Gaume and Paul H. Ginsparg. The Topological Meaning of Non-abelian Anomalies. *Nucl. Phys. B*, 243:449–474, 1984. doi: 10.1016/0550-3213(84)90487-5.

[49] Luis Alvarez-Gaume. Supersymmetry and the Atiyah-Singer Index Theorem. *Commun. Math. Phys.*, 90:161, 1983. doi: 10.1007/BF01205500.

[50] Sören Schlichting and Sayantan Sharma. Chiral Instabilities and the Fate of Chirality Imbalance in Non-Abelian Plasmas. *Phys. Rev. Lett.*, 131(10):102303, 2023. doi: 10.1103/PhysRevLett.131.102303.

[51] Peter Brockway Arnold and Larry D. McLerran. The Sphaleron Strikes Back. *Phys. Rev. D*, 37:1020, 1988. doi: 10.1103/PhysRevD.37.1020.

[52] Harvey B. Meyer. Transport properties of the quark-gluon plasma from lattice QCD. *Nucl. Phys. A*, 830:641C–648C, 2009. doi: 10.1016/j.nuclphysa.2009.09.053.

[53] Luis Altenkort, Alexander M. Eller, Olaf Kaczmarek, Lukas Mazur, Guy D. Moore, and Hai-Tao Shu. Sphaleron rate from Euclidean lattice correlators: An exploration. *Phys. Rev. D*, 103(11):114513, 2021. doi: 10.1103/PhysRevD.103.114513.

[54] Gokce Basar and Dmitri E. Kharzeev. The Chern-Simons diffusion rate in strongly coupled N=4 SYM plasma in an external magnetic field. *Phys. Rev. D*, 85:086012, 2012. doi: 10.1103/PhysRevD.85.086012.

[55] Dmitri E. Kharzeev. The Chiral Magnetic Effect and Anomaly-Induced Transport. *Prog. Part. Nucl. Phys.*, 75:133–151, 2014. doi: 10.1016/j.ppnp.2014.01.002.

[56] Yuji Hirono, Dmitri Kharzeev, and Yi Yin. Self-similar inverse cascade of magnetic helicity driven by the chiral anomaly. *Phys. Rev. D*, 92(12):125031, 2015. doi: 10.1103/PhysRevD.92.125031.

[57] E. V. Gorbar, I. A. Shovkovy, S. Vilchinskii, I. Rudenok, A. Boyarsky, and O. Ruchayskiy. Anomalous Maxwell equations for inhomogeneous chiral plasma. *Phys. Rev. D*, 93(10):105028, 2016. doi: 10.1103/PhysRevD.93.105028.

[58] Kirill Tuchin. Taming instability of magnetic field in chiral medium. *Nucl. Phys. A*, 969:1–13, 2018. doi: 10.1016/j.nuclphysa.2017.09.015.

[59] Mark Mace, Niklas Mueller, Sören Schlichting, and Sayantan Sharma. Chiral Instabilities and the Onset of Chiral Turbulence in QED Plasmas. *Phys. Rev. Lett.*, 124(19):191604, 2020. doi: 10.1103/PhysRevLett.124.191604.

[60] Igor Rogachevskii, Oleg Ruchayskiy, Alexey Boyarsky, Jürg Fröhlich, Nathan Kleeorin, Axel Brandenburg, and Jennifer Schober. Laminar and turbulent dynamos in chiral magnetohydrodynamics-I: Theory. *Astrophys. J.*, 846(2):153, 2017. doi: 10.3847/1538-4357/aa886b.

[61] Yukinao Akamatsu and Naoki Yamamoto. Chiral Plasma Instabilities. *Phys. Rev. Lett.*, 111:052002, 2013. doi: 10.1103/PhysRevLett.111.052002.

[62] Dam Thanh Son and Naoki Yamamoto. Berry Curvature, Triangle Anomalies, and the Chiral Magnetic Effect in Fermi Liquids. *Phys. Rev. Lett.*, 109:181602, 2012. doi: 10.1103/PhysRevLett.109.181602.

[63] Cristina Manuel and Juan M. Torres-Rincon. Dynamical evolution of the chiral magnetic effect: Applications to the quark-gluon plasma. *Phys. Rev. D*, 92(7): 074018, 2015. doi: 10.1103/PhysRevD.92.074018.

[64] Koichi Hattori, Yuji Hirono, Ho-Ung Yee, and Yi Yin. MagnetoHydrodynamics with chiral anomaly: phases of collective excitations and instabilities. *Phys. Rev. D*, 100(6):065023, 2019. doi: 10.1103/PhysRevD.100.065023.

[65] E. V. Gorbar, V. A. Miransky, I. A. Shovkovy, and P. O. Sukhachov. Consistent hydrodynamic theory of chiral electrons in Weyl semimetals. *Phys. Rev. B*, 97 (12):121105, 2018. doi: 10.1103/PhysRevB.97.121105.

[66] P. V. Buividovich and M. V. Ulybyshev. Numerical study of chiral plasma instability within the classical statistical field theory approach. *Phys. Rev. D*, 94(2): 025009, 2016. doi: 10.1103/PhysRevD.94.025009.

[67] Daniel G. Figueroa, Adrien Florio, and Mikhail Shaposhnikov. Chiral charge dynamics in Abelian gauge theories at finite temperature. *JHEP*, 10:142, 2019. doi: 10.1007/JHEP10(2019)142.

[68] James M. Cline, Kimmo Kainulainen, and Keith A. Olive. On the erasure and regeneration of the primordial baryon asymmetry by sphalerons. *Phys. Rev. Lett.*, 71:2372–2375, 1993. doi: 10.1103/PhysRevLett.71.2372.

[69] V. A. Kuzmin, V. A. Rubakov, and M. E. Shaposhnikov. On the Anomalous Electroweak Baryon Number Nonconservation in the Early Universe. *Phys. Lett. B*, 155:36, 1985. doi: 10.1016/0370-2693(85)91028-7.

[70] V. A. Rubakov and M. E. Shaposhnikov. Electroweak baryon number nonconservation in the early universe and in high-energy collisions. *Usp. Fiz. Nauk*, 166: 493–537, 1996. doi: 10.1070/PU1996v039n05ABEH000145.

[71] Dietrich Bodeker and Wilfried Buchmuller. Baryogenesis from the weak scale to the grand unification scale. *Rev. Mod. Phys.*, 93(3):035004, 2021. doi: 10.1103/RevModPhys.93.035004.

[72] Volker Koch, Soeren Schlichting, Vladimir Skokov, Paul Sorensen, Jim Thomas, Sergei Voloshin, Gang Wang, and Ho-Ung Yee. Status of the chiral magnetic effect and collisions of isobars. *Chin. Phys. C*, 41(7):072001, 2017. doi: 10.1088/1674-1137/41/7/072001.

[73] Sergei A. Voloshin. Testing the Chiral Magnetic Effect with Central U+U collisions. *Phys. Rev. Lett.*, 105:172301, 2010. doi: 10.1103/PhysRevLett.105.172301.

[74] Mohamed Abdallah et al. Search for the chiral magnetic effect with isobar collisions at $\sqrt{s_{NN}}$=200 GeV by the STAR Collaboration at the BNL Relativistic Heavy Ion Collider. *Phys. Rev. C*, 105(1):014901, 2022. doi: 10.1103/PhysRevC.105.014901.

[75] J. Adam et al. Methods for a blind analysis of isobar data collected by the STAR collaboration. *Nucl. Sci. Tech.*, 32(5):48, 2021. doi: 10.1007/s41365-021-00878-y.

[76] Dmitri E. Kharzeev, Jinfeng Liao, and Shuzhe Shi. Implications of the isobar-run results for the chiral magnetic effect in heavy-ion collisions. *Phys. Rev. C*, 106(5):L051903, 2022. doi: 10.1103/PhysRevC.106.L051903.

[77] D. T. Son and B. Z. Spivak. Chiral Anomaly and Classical Negative Magnetoresistance of Weyl Metals. *Phys. Rev. B*, 88:104412, 2013. doi: 10.1103/PhysRevB.88.104412.

[78] Edmond Iancu and Raju Venugopalan. *The Color glass condensate and high-energy scattering in QCD*, pages 249–3363. 3 2003. doi: 10.1142/9789812795533_0005.

[79] Francois Gelis, Edmond Iancu, Jamal Jalilian-Marian, and Raju Venugopalan. The Color Glass Condensate. *Ann. Rev. Nucl. Part. Sci.*, 60:463–489, 2010. doi: 10.1146/annurev.nucl.010909.083629.

[80] Larry McLerran. The CGC and the Glasma: Two Lectures at the Yukawa Insitute. *Prog. Theor. Phys. Suppl.*, 187:17–30, 2011. doi: 10.1143/PTPS.187.17.

[81] Larry D. McLerran and Raju Venugopalan. Computing quark and gluon distribution functions for very large nuclei. *Phys. Rev. D*, 49:2233–2241, 1994. doi: 10.1103/PhysRevD.49.2233.

[82] Gert Aarts and Jan Smit. Classical approximation for time dependent quantum field theory: Diagrammatic analysis for hot scalar fields. *Nucl. Phys. B*, 511:451–478, 1998. doi: 10.1016/S0550-3213(97)00723-2.

[83] Dietrich Bodeker. Classical real time correlation functions and quantum corrections at finite temperature. *Nucl. Phys. B*, 486:500–514, 1997. doi: 10.1016/S0550-3213(96)00688-8.

[84] Mikko Laine, Guy D. Moore, Owe Philipsen, and Marcus Tassler. Heavy Quark Thermalization in Classical Lattice Gauge Theory: Lessons for Strongly-Coupled QCD. *JHEP*, 05:014, 2009. doi: 10.1088/1126-6708/2009/05/014.

[85] John B. Kogut and Leonard Susskind. Hamiltonian Formulation of Wilson's Lattice Gauge Theories. *Phys. Rev. D*, 11:395–408, 1975. doi: 10.1103/PhysRevD.11.395.

[86] J. Berges, S. Scheffler, and D. Sexty. Turbulence in nonabelian gauge theory. *Phys. Lett. B*, 681:362–366, 2009. doi: 10.1016/j.physletb.2009.10.032.

[87] Aleksi Kurkela and Guy D. Moore. UV Cascade in Classical Yang-Mills Theory. *Phys. Rev. D*, 86:056008, 2012. doi: 10.1103/PhysRevD.86.056008.

[88] Mark C. Abraao York, Aleksi Kurkela, Egang Lu, and Guy D. Moore. UV cascade in classical Yang-Mills theory via kinetic theory. *Phys. Rev. D*, 89(7):074036, 2014. doi: 10.1103/PhysRevD.89.074036.

[89] Soeren Schlichting. Turbulent thermalization of weakly coupled non-abelian plasmas. *Phys. Rev. D*, 86:065008, 2012. doi: 10.1103/PhysRevD.86.065008.

[90] J. Berges, K. Boguslavski, S. Schlichting, and R. Venugopalan. Turbulent thermalization process in heavy-ion collisions at ultrarelativistic energies. *Phys. Rev. D*, 89(7):074011, 2014. doi: 10.1103/PhysRevD.89.074011.

[91] Aleksi Kurkela and Guy D. Moore. Thermalization in Weakly Coupled Nonabelian Plasmas. *JHEP*, 12:044, 2011. doi: 10.1007/JHEP12(2011)044.

[92] K. Boguslavski, A. Kurkela, T. Lappi, and J. Peuron. Highly occupied gauge theories in 2+1 dimensions: A self-similar attractor. *Phys. Rev. D*, 100(9):094022, 2019. doi: 10.1103/PhysRevD.100.094022.

[93] Guy D. Moore and Neil Turok. Lattice Chern-Simons number without ultraviolet problems. *Phys. Rev. D*, 56:6533–6546, 1997. doi: 10.1103/PhysRevD.56.6533.

[94] Juergen Berges and Julien Serreau. Parametric resonance in quantum field theory. *Phys. Rev. Lett.*, 91:111601, 2003. doi: 10.1103/PhysRevLett.91.111601.

[95] Jennie H. Traschen and Robert H. Brandenberger. Particle Production During Out-of-equilibrium Phase Transitions. *Phys. Rev. D*, 42:2491–2504, 1990. doi: 10.1103/PhysRevD.42.2491.

[96] Lev Kofman, Andrei D. Linde, and Alexei A. Starobinsky. Reheating after inflation. *Phys. Rev. Lett.*, 73:3195–3198, 1994. doi: 10.1103/PhysRevLett.73.3195.

[97] Juergen Berges, Alexander. Rothkopf, and Jonas Schmidt. Non-thermal fixed points: Effective weak-coupling for strongly correlated systems far from equilibrium. *Phys. Rev. Lett.*, 101:041603, 2008. doi: 10.1103/PhysRevLett.101.041603.

[98] Alejandro Arrizabalaga, Jan Smit, and Anders Tranberg. Tachyonic preheating using 2PI-1/N dynamics and the classical approximation. *JHEP*, 10:017, 2004. doi: 10.1088/1126-6708/2004/10/017.

[99] A. Piñeiro Orioli, K. Boguslavski, and J. Berges. Universal self-similar dynamics of relativistic and nonrelativistic field theories near nonthermal fixed points. *Phys. Rev. D*, 92(2):025041, 2015. doi: 10.1103/PhysRevD.92.025041.

[100] Maximilian Prüfer, Philipp Kunkel, Helmut Strobel, Stefan Lannig, Daniel Linnemann, Christian-Marcel Schmied, Jürgen Berges, Thomas Gasenzer, and Markus K. Oberthaler. Observation of universal dynamics in a spinor Bose gas far from equilibrium. *Nature*, 563(7730):217–220, 2018. doi: 10.1038/s41586-018-0659-0.

[101] Maximilian Prüfer, Torsten V. Zache, Philipp Kunkel, Stefan Lannig, Alexis Bonnin, Helmut Strobel, Jürgen Berges, and Markus K. Oberthaler. Experimental extraction of the quantum effective action for a non-equilibrium many-body system. *Nature Phys.*, 16(10):1012–1016, 2020. doi: 10.1038/s41567-020-0933-6.

[102] Sebastian Erne, Robert Bücker, Thomas Gasenzer, Jürgen Berges, and Jörg Schmiedmayer. Universal dynamics in an isolated one-dimensional Bose gas far from equilibrium. *Nature*, 563(7730):225–229, 2018. doi: 10.1038/s41586-018-0667-0.

[103] E. V. Gorbar, V. A. Miransky, I. A. Shovkovy, and P. O. Sukhachov. Quantum oscillations as a probe of interaction effects in Weyl semimetals in a magnetic field. *Phys. Rev. B*, 90(11):115131, 2014. doi: 10.1103/PhysRevB.90.115131.

[104] Peter Brockway Arnold, Guy D. Moore, and Laurence G. Yaffe. Transport coefficients in high temperature gauge theories. 1. Leading log results. *JHEP*, 11:001, 2000. doi: 10.1088/1126-6708/2000/11/001.

[105] Jonah E. Bernhard, J. Scott Moreland, and Steffen A. Bass. Bayesian estimation of the specific shear and bulk viscosity of quark–gluon plasma. *Nature Phys.*, 15 (11):1113–1117, 2019. doi: 10.1038/s41567-019-0611-8.

[106] A. V. Sadofyev and M. V. Isachenkov. The Chiral magnetic effect in hydrodynamical approach. *Phys. Lett. B*, 697:404–406, 2011. doi: 10.1016/j.physletb.2011.02.041.

[107] Xu-Guang Huang and Jinfeng Liao. Axial Current Generation from Electric Field: Chiral Electric Separation Effect. *Phys. Rev. Lett.*, 110(23):232302, 2013. doi: 10.1103/PhysRevLett.110.232302.

[108] Lars Onsager. Reciprocal Relations in Irreversible Processes. I. *Phys. Rev.*, 37(4): 405–426, 1931. doi: 10.1103/physrev.37.405.

[109] V. Skokov, A. Yu. Illarionov, and V. Toneev. Estimate of the magnetic field strength in heavy-ion collisions. *Int. J. Mod. Phys. A*, 24:5925–5932, 2009. doi: 10.1142/S0217751X09047570.

[110] Jean-Paul Blaizot, Jinfeng Liao, and Yacine Mehtar-Tani. The thermalization of soft modes in non-expanding isotropic quark gluon plasmas. *Nucl. Phys. A*, 961: 37–67, 2017. doi: 10.1016/j.nuclphysa.2017.02.003.

[111] J. Berges, K. Boguslavski, S. Schlichting, and R. Venugopalan. Universality far from equilibrium: From superfluid Bose gases to heavy-ion collisions. *Phys. Rev. Lett.*, 114(6):061601, 2015. doi: 10.1103/PhysRevLett.114.061601.

[112] J. Berges, K. Boguslavski, S. Schlichting, and R. Venugopalan. Nonequilibrium fixed points in longitudinally expanding scalar theories: infrared cascade, Bose condensation and a challenge for kinetic theory. *Phys. Rev. D*, 92(9):096006, 2015. doi: 10.1103/PhysRevD.92.096006.

[113] A. Schachner, A. Piñeiro Orioli, and J. Berges. Universal scaling of unequal-time correlation functions in ultracold Bose gases far from equilibrium. *Phys. Rev. A*, 95(5):053605, 2017. doi: 10.1103/PhysRevA.95.053605.

[114] R. Walz, K. Boguslavski, and J. Berges. Large-N kinetic theory for highly occupied systems. *Phys. Rev. D*, 97(11):116011, 2018. doi: 10.1103/PhysRevD.97.116011.

[115] Isara Chantesana, Asier Piñeiro Orioli, and Thomas Gasenzer. Kinetic theory of nonthermal fixed points in a Bose gas. *Phys. Rev. A*, 99(4):043620, 2019. doi: 10.1103/PhysRevA.99.043620.

[116] Kirill Boguslavski and Asier Piñeiro Orioli. Unraveling the nature of universal dynamics in $O(N)$ theories. *Phys. Rev. D*, 101(9):091902, 2020. doi: 10.1103/PhysRevD.101.091902.

[117] Jürgen Berges, Kirill Boguslavski, Lillian de Bruin, Tara Butler, and Jan M. Pawlowski. Order parameters for gauge invariant condensation far from equilibrium. 7 2023.

[118] T. Lappi and L. McLerran. Some features of the glasma. *Nucl. Phys. A*, 772: 200–212, 2006. doi: 10.1016/j.nuclphysa.2006.04.001.

[119] Gert Aarts and Juergen Berges. Classical aspects of quantum fields far from equilibrium. *Phys. Rev. Lett.*, 88:041603, 2002. doi: 10.1103/PhysRevLett.88.041603.

[120] Jan Smit and Anders Tranberg. Chern-Simons number asymmetry from CP violation at electroweak tachyonic preheating. *JHEP*, 12:020, 2002. doi: 10.1088/1126-6708/2002/12/020.

[121] Jan Ambjorn, T. Askgaard, H. Porter, and M. E. Shaposhnikov. Sphaleron transitions and baryon asymmetry: A Numerical real time analysis. *Nucl. Phys. B*, 353:346–378, 1991. doi: 10.1016/0550-3213(91)90341-T.

[122] K. Boguslavski, A. Kurkela, T. Lappi, and J. Peuron. Spectral function for overoccupied gluodynamics from real-time lattice simulations. *Phys. Rev. D*, 98(1): 014006, 2018. doi: 10.1103/PhysRevD.98.014006.

[123] Raphael Micha and Igor I. Tkachev. Relativistic turbulence: A Long way from preheating to equilibrium. *Phys. Rev. Lett.*, 90:121301, 2003. doi: 10.1103/PhysRevLett.90.121301.

[124] J. Berges, K. Boguslavski, S. Schlichting, and R. Venugopalan. Basin of attraction for turbulent thermalization and the range of validity of classical-statistical simulations. *JHEP*, 05:054, 2014. doi: 10.1007/JHEP05(2014)054.

[125] Christian-Marcel Schmied, Aleksandr N. Mikheev, and Thomas Gasenzer. Nonthermal fixed points: Universal dynamics far from equilibrium. *Int. J. Mod. Phys. A*, 34(29):1941006, 2019. doi: 10.1142/S0217751X19410069.

[126] Aleksandr N. Mikheev, Christian-Marcel Schmied, and Thomas Gasenzer. Low-energy effective theory of nonthermal fixed points in a multicomponent Bose gas. *Phys. Rev. A*, 99(6):063622, 2019. doi: 10.1103/PhysRevA.99.063622.